Photoelectron diffraction in magnetic dichroism in core-level photoemission

elektronisches dokument
ULB Sachsen-Anhalt

Dissertation

zur Erlangung des akademischen Grades
doctor rerum naturalium (Dr. rer. nat.)

vorgelegt der

Mathematisch-Naturwissenschaftlich-Technischen Fakultät
(mathematisch-naturwissenschaftlicher Bereich)
der Martin-Luther-Universität Halle-Wittenberg

von Herrn Xingyu Gao

geb. am 08.10.1969 in Minshan, Provinz Sichuan, V. R. China

Gutachter:
1. Prof. Dr. J. Kirschner
2. Prof. Dr. H. Neddermeyer
3. Prof. Dr. K. Baberschke

Halle (Saale),14.7.1999

Contents

1 Introduction **1**

2 Theoretical aspects of core-level photoemission **3**
2.1 Basic concepts of core-level photoemission 3
2.2 One-electron theory of core-level photoemission from ferromagnets . . . 6
2.3 Magnetic dichroism in core-level photoemission 10

3 Experimental aspects **13**
3.1 Apparatus 13
3.2 Light sources for XPS 15
3.2.1 x-ray tube 16
3.2.2 Circularly polarized light at ESRF 18

4 MDAD in core-level photoemission **20**
4.1 Basic review and introduction of forward scattering 20
4.2 Co/Cu(001) 23
4.2.1 General aspects 23
4.2.2 MDAD of 5 ML Co/Cu(001) at different temperatures 25
4.2.3 MDAD of Co/Cu(001) at different thicknesses 33
4.2.4 MDAD in an extended angular range including several low index axes 38
4.2.5 MDAD of 5 ML Co/Cu(001) using circular light with lower photon energy 48
4.3 Fe/Co/Cu(001) 54
4.3.1 Review of Fe/Co/Cu(001) 54
4.3.2 Different angular dependencies of 3 ML and 8 ML Fe/Co/Cu(001) in MDAD using unpolarized light 56
4.3.3 MCDAD of Fe/Co/Cu(001) at different thicknesses 59

5 Discussion **68**
5.1 Co/Cu(001) 68
5.1.1 The principle of the diffraction effects in MLDAD 68
5.1.2 Temperature effect and thickness dependence 73
5.1.3 Other low index axes 77
5.1.4 Lower kinetic energies 78
5.2 Fe/Co/Cu(001) 79

Zusammenfassung **85**

References **89**

1 Introduction

Thin films of ferromagnetic materials, epitaxially grown on non-magnetic substrates, have since long been of interest. Often, the films will grow in a metastable structure which follows that of the substrate rather than that of the natural bulk equilibrium phase of the film. Since the magnetic properties of a material are sensitive to the structure, epitaxial films offer a possibility to study the relationship between magnetism and structure. Also ultrathin magnetic films as magnetic 2-dimensional systems may reveal unique magnetic properties due to the reduced symmetry and dimension. For example, the critical temperature (the Curie temperature in the case of bulk materials), describing the transition from the magnetic phase to the non-magnetic phase, will strongly depend on the thickness of the film. Magnetic films therefore represent a complicated system in which the magnetic properties are strongly related to the structure, morphology and thickness of the film. In particular, it is known that both structure and magnetism of film interfaces and surfaces may very well deviate from those of the interior of the film [1]. For the study of such systems a method is thus needed which permits one to obtain information about the depth distribution of magnetic properties within a single film of the same element.

A possibility to achieve this is on the one hand to make use of the structural information intrinsic to the angular distribution of photoelectrons, which is governed by scattering events of the photo-emitted electrons at the surrounding atom cores. This effect is employed for structural investigations in surface physics (photoelectron diffraction) [2]. The change of the spectral intensity distribution of photoelectrons upon magnetization reversal, on the other hand, yields information about the magnetic properties; in the case when core levels are probed, even with elemental resolution. This effect is termed magnetic dichroism in angular-resolved photoemission (MDAD), and is a widely used technique for magnetic characterization [3-16]. It seems obvious that the combination of both photoelectron diffraction and magnetic dichroism, which implies recording the angular *and* spectral distribution of photoelectrons [17, 19], should allow one to study structural and magnetic properties of thin films and surfaces at the same time, i.e., give structural information on a magnetic basis, or magnetic information on a structural basis.

The idea is thus to study the angular dependence of magnetic dichroism in photoemission using unpolarized light in a geometry with a fixed angle between the incident photons ($\mathbf{q}$) and the outgoing photoelectrons ($\mathbf{k}$). The dichroism is coming from the photoemission intensity difference by reversing the magnetization $\mathbf{M}$, which is vertical to the plane consisting of $\mathbf{q}$ and $\mathbf{k}$ (cf. Fig. 4.3 on page 24). Using just the single atom model the dichroism should be proportional to $\mid \mathbf{M} \bullet (\mathbf{k} \times \mathbf{E})(\mathbf{k} \bullet \mathbf{E}) \mid \propto \sin(2\theta)$,

where **E** is the electric field vector of the light, and θ the angle between **k** and **E** [21]. By rotating the sample to vary the emission angle in this geometry, any change of the dichroism is then related to the crystal lattice (diffraction effects). Recent MDAD experiments have shown that a strong modulation on the angular distribution of the atomic-like dichroism appears, which is mainly due to forward scattering of photoelectrons [17-20] In those experiments it was observed that diffraction effects were present for emission direction off the sample normal, giving origin to a characteristic *chessboard* pattern in the angular distribution of the dichroic asymmetry. Along low index directions the dichroism was found to exhibit mainly atomic character [17, 19].

Due to their well known epitaxial layer-by-layer growth, structure and magnetic properties [22-29], Co/Cu(001) films were chosen for such a investigation to obtain knowledge about the role of diffraction effects in magnetic dichroism. Angular distributions of MDAD were measured for different thicknesses and temperatures to establish the connection with photoelectron diffraction (PED).

To exploit the combination of PED and MDAD as a method to study structure and magnetism at the same time, ultrathin fcc Fe films on Co/Cu(001) were chosen. Fcc-Fe, which can be stabilized in ultrathin films by the choice of appropriate substrates, is a system in which striking differences between magnetic properties of film surface and interior have been observed. Fe films of a certain thickness, deposited at room temperature directly on Cu(001), exhibit a non-ferromagnetic behavior of the inner film layers, but ferromagnetism at the film surface [30-33]. Bringing this film into contact with a ferromagnetic underlayer, in the present case Co, raises the question of the magnetic phases which will then be present in the fcc Fe overlayer. It is particularly interesting to see, whether or not a magnetic material, Fe, possibly remains non-ferromagnetic in contact with another magnetic material. If this should be the case, it has to be checked whether there is also a ferromagnetic layer at the surface. This question can be answered from the angular distribution of MDAD in Fe/Co/Cu(001) films, which will demonstrate the ability of this method to obtain information about the distribution of magnetic properties within a single film of the same element.

2 Theoretical aspects of core-level photoemission

2.1 Basic concepts of core-level photoemission

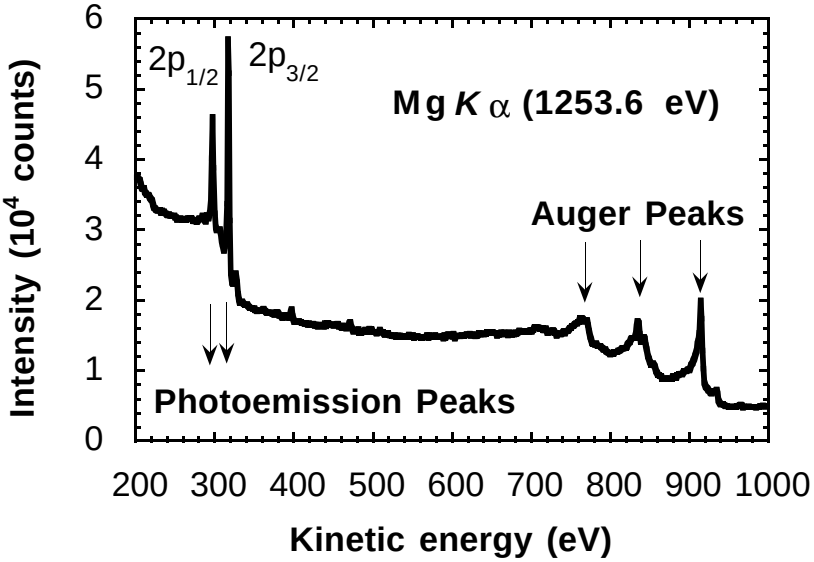

Figure 2.1: 'Typical' XPS spectrum using 1253.6 eV photon (Mg K_α) on a clean Cu(001) sample at normal emission.

When photons with the wavelength in the x-ray region are incident on the crystal surface, the energy distribution of the emitted electrons can be measured. This is called x-ray photoelectron spectroscopy (XPS). Fig. 2.1 shows a spectrum taken from a clean Cu(001) sample, using unpolarized light with a photon energy of 1253.6 eV. There are two processes leading to intensity peaks: direct photoemission and electrons from Auger decay. The latter are also easily excited by incident electrons, which has led to the development of Auger electron spectroscopy (AES) into a standard surface science tool. Therefore in XPS one concentrates on the photoemission peaks. In the spectrum there is a step-like structure at each photoemission peak. This is due to inelastically scattered secondary electrons. Each discrete emission opens up a new channel of primary electrons to be inelastically scattered into lower kinetic energy states, resulting in the higher intensity step at lower kinetic energies of each emission peak.

As discussed in the introduction, the photoemission from core-levels is known as a technique to determine the atomic species on the surface. This is because the core levels are electronic states localized on a single atom and less affected by the neighboring atoms than the electrons in the valence band. Since the local chemical and electronic environments can contribute to so-called 'chemical shifts', further information about the chemical state of an atomic species on the surface can be obtained. That is the

reason that XPS is also called ESCA – Electron Spectroscopy for Chemical Analysis. Generally from the photoemission spectrum the binding energy E_b can be determined by the formula

$$E_{kin} = hv - E_b. \tag{2.1}$$

Actually there will be a so-called relaxation shift in the spectrum from many-body effects which will be discussed later, after the theory to describe the photoemission process has been introduced.

In a photoemission process, light of a given photon energy and a given polarization interacts with the atoms in the sample. Electrons will be excited from an initial bound energy level into free electronic states above the Fermi level. There are many parameters in the description of such a process, which depend on the geometry. The electromagnetic field can be described in a perturbation Hamiltonian,

$$H' = \frac{e}{mc}\vec{A}\cdot\vec{p}, \tag{2.2}$$

where $\vec{A}(\vec{r},t)$ is the vector potential of the light and $\vec{p} = -i\hbar\vec{\bigtriangledown}$ is the electron movement momentum operator. The vector potential can be written in the following form:

$$\vec{A}(\vec{r},t) = \hat{\epsilon}A_0\exp[i(\vec{q}\cdot\vec{r} - \omega t)], \tag{2.3}$$

where $\hat{\epsilon}$, $\vec{q}$ and ω are the unit polarization vector, the wavevector and the angular velocity of the light, respectively.

The transition rate $R_{i\to f}$ between an initial core-level state $|\Psi_i\rangle$ to a final free electron state $|\Psi_f(\vec{k})\rangle$ with wavevector $\vec{k}$ can be deduced from time-dependent perturbation theory as:

$$R_{i\to f} = \frac{2\pi}{\hbar}|M_{if}|^2\rho(E). \tag{2.4}$$

This is called Fermi's Golden Rule. $\rho(E)$ is the electron density of states at energy E. From (2.2) and (2.3) there follows

$$|M_{if}|^2 = |\langle\Psi_f(\vec{k})|\vec{A}\cdot\vec{p}|\Psi_i\rangle|^2 = \hbar^2A_0^2|\langle\Psi_f(\vec{k})|\exp(i\vec{q}\cdot\vec{r})\hat{\epsilon}\cdot\vec{\bigtriangledown}|\Psi_i\rangle|^2. \tag{2.5}$$

The wavelength of the soft x-ray light in the present case is of the order of 10 Å and the spatial extension of a highly localized core electron is ≈ 0.5 Å. Therefore for the highly localized core-level electron the electric dipole approximation (i.e., $\exp(i\vec{q}\cdot\vec{r}) \approx 1$) is good enough to describe the emission process. Then the matrix elements can be obtained as [34]

$$M_{if} = C\langle\Psi_f(\vec{k})|\hat{\epsilon}\cdot\vec{r}|\Psi_i\rangle. \tag{2.6}$$

Here C is the product of fundamental constants and A_0. From the symmetry character of the involved wave functions and the dipole operator the following selection rules

can be deduced from group theory:

$$\begin{aligned} l^f - l &= \pm 1 \\ m_l^f - m_l &= 0, \pm 1 \\ m_s^f - m_s &= 0, \end{aligned} \tag{2.7}$$

where for the initial state the l, m_l are the orbital quantum numbers and m_s is the spin quantum number. For the final state these numbers are l^f, m_l^f and m_s^f. For the two different l^f values, there will be in general two photoemission channels: $l^f = l+1$ and $l^f = l-1$.

The initial state is actually an atomic ground state of the N-electron system, even without considering the influence of the solid environment. There will generally be somw many-body character in these ground states. However for a weakly correlated system the initial state may often be approximated by a single-particle wavefunction corresponding to the core-level. The final state is also a N-electron state containing a core hole and an outgoing electron. Normally the coupling between the photoelectron and the $(N-1)$-electron system is negligible, so that the final state can be decomposed in two parts:

$$|\Psi_f(\vec{k})\rangle = |\Psi_f^+(N-1); \phi_f(\vec{k})\rangle, \tag{2.8}$$

where $|\Psi_f^+(N-1)\rangle$ is the many-body eigenstate of the system and $|\phi_f(\vec{k})\rangle$ is the wavefunction of the outgoing photoelectron. Therefore two kinds of so-called "final-state effects" can be defined, which are related to $|\Psi_f^+(N-1)\rangle$ and $|\phi_f(\vec{k})\rangle$, respectively.

The first type of final-state effect is a many-body effect: it is the result of the many-electron response to the sudden creation of a core-hole. When the core hole is created by photoemission, the other electrons, especially the valence-band electrons, will relax in energy to higher binding energies to screen the core hole partially. This changes the kinetic energy of the outgoing electron by a relaxation shift. This shift can be decomposed into two parts: the intra-atomic relaxation shift E_a, which is present in the case of a free atom, and an extra relaxation shift E_r associated with the solid state environment. Also a consequence of the interaction between the core-hole and the valence electrons is that the spectral density in photoemission is not a single sharp peak, but a broadened feature with multiplet splittings and satellite structures.

The second type of final-state effect is due to photoelectron scattering in the lattice on the way out of the crystal. The scattered waves can interfere constructively or destructively with the direct photoelectron wave, thus causing the modulations in the spectra of photoemission. This kind of effects will be the topic of the following chapters. Before turning to the scattering, however, it is necessary to discuss core-level photoemission from ferromagnetic systems.

2.2 One-electron theory of core-level photoemission from ferromagnets

The extension of conventional XPS to magnetic materials leads to magnetic dichroism. The theoretical models of magnetic dichroism in core-level photoemission can be divided into four categories. On one hand, a distinction can be made between one-particle (ground-state) and many-body (excited-state) theories, on the other hand one can classify between atomic theories and those which take into account the solid, in particular photo-electron diffraction. Therefore, there are atomic one-particle theories (for examples Refs. [35-37]), atomic many-particle theories (for example Refs. [38-42]), solid many-particle theories (for example Ref.[43]), and solid one-electron theories (for example Refs. [44-47]). In order to discuss the results of the core-level photoemission in a clear physical picture, the one-electron model of core-level photoemission after J. G. Menchero [35] will be introduced here. This theory describes the core-level spectra of Fe and Co well, which have no pronounced satellites due to many-body effects. Although it does not include the crystallinity of the sample, and is very complicated to calculate for a general geometry, it is well suited to understand the fundamental origin of the dichroism in photoemission.

The electric operator is defined as

$$T_\varepsilon = \vec{r} \cdot \vec{\varepsilon} = x\varepsilon_x + y\varepsilon_y + z\varepsilon_z, \tag{2.9}$$

where $\vec{r}$ is the electron coordinate vector and ε is the electric field polarization.

$$\vec{r} = r\hat{r} = r[(\frac{x}{r})\hat{e_x} + (\frac{y}{r})\hat{e_y} + (\frac{z}{r})\hat{e_z}]$$

$$\vec{\varepsilon} = \varepsilon_x\hat{e_x} + \varepsilon_y\hat{e_y} + \varepsilon_z\hat{e_z}. \tag{2.10}$$

Expressing $\frac{x}{r}$, $\frac{y}{r}$ and $\frac{z}{r}$ by spherical harmonics, the dipole operator can be written as [35]

$$T_\varepsilon = \vec{r} \cdot \vec{\varepsilon} = r\frac{4\pi}{3}(-Y_1^1\varepsilon_+ + Y_1^{-1}\varepsilon_- + Y_1^0\varepsilon_z), \tag{2.11}$$

where

$$\varepsilon_+ = \frac{\varepsilon_x - i\varepsilon_y}{\sqrt{2}}, \quad \varepsilon_- = \frac{\varepsilon_x + i\varepsilon_y}{\sqrt{2}}. \tag{2.12}$$

For a better understanding of the relationship between the dipole operator and the geometry of the experiment, Fig. 2.2 shows the situation of an oriented atom. k is the photoelectron wavevector and the q is the photon wavevector. A normalized polarization vector $\hat{\varepsilon}$ then can be written in spherical coordinates in terms of two angles α and δ:

$$\hat{\varepsilon} = \cos\alpha\hat{\varepsilon}_\theta + \sin\alpha e^{i\delta}\hat{\varepsilon}_\phi. \tag{2.13}$$

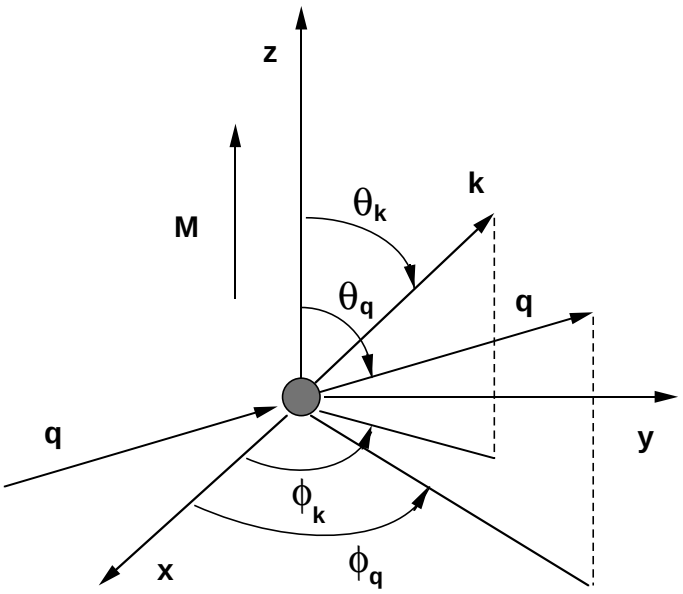

Figure 2.2: A geometry for an orientated atom.

θ_q and ϕ_q are the spherical coordinates for the photon wavevector in Fig. 2.2. α determines the relative magnitude between the two orthogonal components of the light electric field and δ determines the phase difference. $\hat{\varepsilon}_\theta$, and $\hat{\varepsilon}_\phi$ are normalized polarization vectors in spherical coordinates.

Then the three components ε_+, ε_-, and ε_z can be expressed as [35]

$$\begin{aligned} \varepsilon_+ &= \frac{e^{-i\phi_q}}{\sqrt{2}}(\cos\alpha\cos\theta_q - i\sin\alpha e^{i\delta}) \\ \varepsilon_- &= \frac{e^{i\phi_q}}{\sqrt{2}}(\cos\alpha\cos\theta_q + i\sin\alpha e^{i\delta}) \\ \varepsilon_z &= -\cos\alpha\sin\theta_q. \end{aligned} \tag{2.14}$$

Now it is easy to write out the dipole operator for different light polarizations in this description. For example, right circularly polarized (RCP) light (positive helicity) propagating along the +z direction means $\theta_q = 0°$, $\alpha = 45°$, and $\delta = 90°$, therefore $|\varepsilon_+| = 1$ and $T_\varepsilon \sim Y_1^1$. As discussed before, the intensity of the excited electrons is not only governed by the dipole operator, but also by the initial core-level wavefunction $|\Psi_{core}\rangle$, and the final wavefunction $|\Psi_{k\sigma}\rangle$ with wavevector k and spin σ. It can be written as

$$I_{k\sigma}^{\varepsilon} = |\langle|\Psi_{k\sigma}|T_\varepsilon|\Psi_{core}\rangle|^2\delta(E_B + E_k - \hbar\omega) \tag{2.15}$$

where E_B is the binding energy of the core-level, E_k is the kinetic energy of the outgoing electron, and $\hbar\omega$ is the photon energy as before.

The final state as a free electron with wavevector k can be written as a superposition of spherical waves,

$$\Psi_{k\sigma}(r,\theta,\phi) = 4\pi \sum_{lm} i^l e^{-i\delta_l} Y^*_{lm},(\theta_k,\phi_k) Y_{lm}(\theta,\phi) f_{kl}(r)\sigma, \tag{2.16}$$

where δ_l are the partial wave phase shifts, and $f_{kl}(r)$ are the radial wavefunctions at kinetic energy $E_k = \hbar^2 k^2/2m$. For a plane wave $\delta_l = 0$ and $f_{kl}(r) = j_{kl}(r)$, where $j_{kl}(r)$ is the spherical Bessel function of order l.

The initial state Ψ_{core} is given by

$$|\Psi_{core}\rangle = |f_{nl}(r); \Phi_\sigma(\theta,\phi)\rangle, \tag{2.17}$$

where $f_{nl}(r)$ is the radial wavefunction and $\Phi_\sigma(\theta,\phi)$ is the part depending on solid angle and spin.

For a spin-orbit split $2p$ state using Clebsch-Gordan coefficients the following representation can be obtained:

$$\begin{aligned}
|3/2,\quad 3/2\rangle &= |Y_1^1\uparrow\rangle \\
|3/2,\quad 1/2\rangle &= \sqrt{\frac{2}{3}}|Y_1^0\uparrow\rangle + \sqrt{\frac{1}{3}}|Y_1^1\downarrow\rangle \\
|3/2,\ -1/2\rangle &= \sqrt{\frac{1}{3}}|Y_1^{-1}\uparrow\rangle + \sqrt{\frac{2}{3}}|Y_1^0\downarrow\rangle \\
|3/2,\ -3/2\rangle &= |Y_1^{-1}\downarrow\rangle \\
|1/2,\quad 1/2\rangle &= \sqrt{\frac{1}{3}}|Y_1^0\uparrow\rangle - \sqrt{\frac{2}{3}}|Y_1^1\downarrow\rangle \\
|1/2,\ -1/2\rangle &= \sqrt{\frac{2}{3}}|Y_1^{-1}\uparrow\rangle - \sqrt{\frac{1}{3}}|Y_1^0\downarrow\rangle.
\end{aligned} \tag{2.18}$$

Now the binding energy for different $|j,m\rangle$ spin-orbit states can be considered. The terms related to spin-orbit interaction and exchange interaction in the Hamiltonian are given by

$$H = \lambda \vec{l}\cdot\vec{s} + \xi s_z, \tag{2.19}$$

where λ determines the strength of the spin-orbit interaction, s_z is the component of the spin along the direction of the magnetic field, and ξ determines the strength of the exchange interaction. Using (2.18) H can be calculated in this basis,

$$H = \frac{1}{6}\begin{pmatrix}
3\lambda+3\xi & 0 & 0 & 0 & 0 & 0 \\
0 & 3\lambda+\xi & 0 & 0 & \sqrt{8}\xi & 0 \\
0 & 0 & 3\lambda-\xi & 0 & 0 & \sqrt{8}\xi \\
0 & 0 & 0 & 3\lambda-3\xi & 0 & 0 \\
0 & \sqrt{8}\xi & 0 & 0 & -6\lambda-\xi & 0 \\
0 & 0 & \sqrt{8}\xi & 0 & 0 & -6\lambda+\xi
\end{pmatrix}. \tag{2.20}$$

As the introduction of a magnetic field breaks the spherical symmetry, the $j = 3/2$ and $j = 1/2$ levels are allowed to mix, as can be seen from the off-diagonal terms in (2.20). Therefore j is not a good quantum number, but m_j is. In the limit $\lambda \gg \xi$ (spin-orbit interaction is much stronger than exchange interaction), which is a good approximation for a $2p$ core-level of the 3d elements, the $p_{3/2}$ and $p_{1/2}$ levels are shifted energetically by $+\lambda/2$ and $-\lambda$, respectively, and an exchange splitting of $\xi/3$ appears between adjacent m_j sublevels. The level scheme for this limit can be seen from Fig. 2.3.

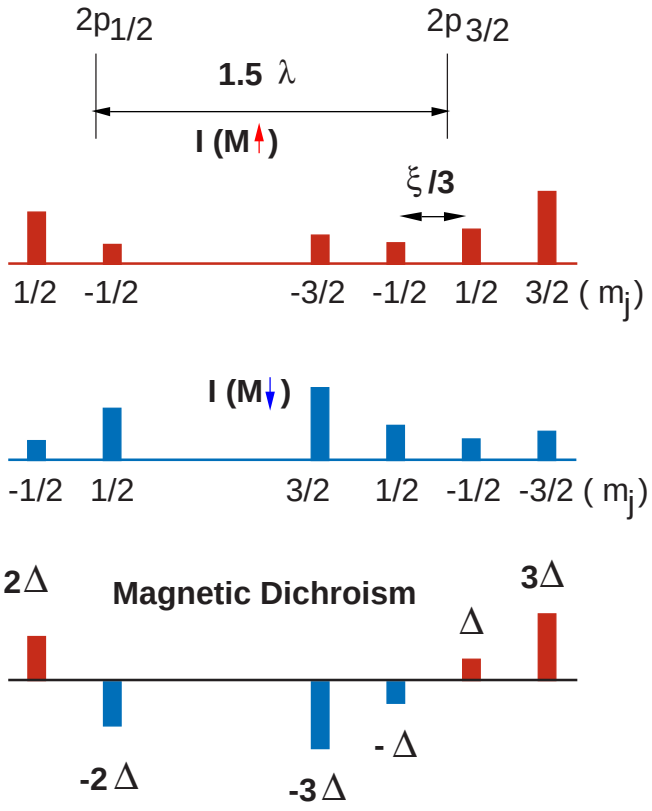

Figure 2.3: Schematic diagram showing the energetic positions of the $|j, m_j\rangle$ core states, photoemission intensity for both magnetic directions, and the magnetic dichroism. The energy scale is with higher binding energy at the left side.

In order to calculate the intensity of the outgoing electron, the three basic photon polarizations rY_1^1, rY_1^{-1}, and rY_1^0 can be considered with the $|j, m_j\rangle$ basis states as initial states and a free electron wavefunction as the final state. For the three basic photon polarizations with $2p$ levels as initial states, the dipole operator matrix elements can be obtained in the three tables in [35]. Any $2p$ core-level state is composed of the $|j, m_j\rangle$ basis states, and any polarized light in any geometry is composed of the three basic photon polarizations, so that it is possible to calculate the matrix

elements for different core-level states from these tables. However, for a general geometry, these calculations include many terms, and can be very complex. Comparing with the one-electron theory introduced by Cherepkov [21, 36, 37], which is more general and powerful, the model by J. G. Menchero is physically more transparent and easier to interpret in an intuitive way.

2.3 Magnetic dichroism in core-level photoemission

In the previous subsection a one-electron theory for core-level photoemission was described. In a next step this model will be used to understand the fundamental origin of magnetic dichroism in the core-level photoemission process. First, the dichroism using both circularly polarized and unpolarized light by reversing the magnetization will be discussed. At the end, magnetic dichroism from helicity reversal will also shortly be mentioned.

In a magnetic dichroism experiment, the dichroism is obtained either by reversing the magnetization or by reversing the helicity of the circularly polarized light. The MDAD effect with circularly polarized radiation is termed MCDAD. When the light source is linearly polarized (the dichroism is termed MLDAD) or unpolarized and the experimental geometry is fixed, it is only possible to get a dichroism by changing the magnetization. Now, first the magnetic dichroism by reversing the magnetization will be discussed. When light with a definite polarization impinges upon a magnetic sample, the dichroic signal is the difference spectrum between the photoemission spectra with a certain magnetization ($M\uparrow$) and opposite magnetization ($M\downarrow$). Here it is better to consider the case with strong spin-orbit coupling ($\lambda \gg \xi$) to offer a simple physical view of the magnetic dichroism. For this limit, to first order, the core eigenstates are just the $|j, m_j\rangle$ spin-orbit eigenstates, and the energy separation between adjacent m_j sublevels is $\xi/3$ (cf. Fig. 2.3). By reversing the magnetization, the transition probabilities from these states remain the same, but the energetic positions of $|j, m_j\rangle$ and $|j, -m_j\rangle$ will be interchanged. This can be seen schematically from Fig. 2.3. Then the dichroic signal $I_{M\uparrow} - I_{M\downarrow}$ can be calculated from $I_{|j,m_j\rangle} - I_{|j,-m_j\rangle}$ at any given energetic position of the sublevels.

For right circularly polarized (RCP) excitation, when the photon wavevector $\vec{q}$ is parallel to the magnetization $\vec{M}$, the intensity difference will be

$$\begin{array}{lrcl} 2P_{3/2}: & I_{|3/2,3/2\rangle} - I_{|3/2,-3/2\rangle} & = & 3\Delta_{MCDAD} \\ & I_{|3/2,1/2\rangle} - I_{|3/2,-1/2\rangle} & = & \Delta_{MCDAD} \\ 2P_{1/2}: & I_{|1/2,1/2\rangle} - I_{|3/2,-1/2\rangle} & = & 2\Delta_{MCDAD}, \end{array} \tag{2.21}$$

where Δ_{MCDAD} gives the angular distribution of the dichroism in MCDAD and can be calculated from the three tables mentioned before.

For linearly polarized excitation, when the photon wavevector $\vec{q} \sim \hat{e}_x$ and $\alpha = 90°$, the dipole operator will be $T_\varepsilon \sim y$, and the magnetic dichroism can be calculated as follows,

$$\begin{array}{lrcl} 2P_{3/2}: & I_{|3/2,3/2\rangle} - I_{|3/2,-3/2\rangle} & = & 3\Delta_{MLDAD} \\ & I_{|3/2,1/2\rangle} - I_{|3/2,-1/2\rangle} & = & \Delta_{MLDAD} \\ 2P_{1/2}: & I_{|1/2,1/2\rangle} - I_{|3/2,-1/2\rangle} & = & 2\Delta_{MLDAD}, \end{array} \tag{2.22}$$

where Δ_{MLDAD} gives the angular distribution of the dichroism in MLDAD. Therefore, except for an angle-dependent scaling factor, the MLDAD signal is equal to the MCDAD spectrum.

In Fig. 2.3 both types of dichroism are identical, as shown schematically. Although this result was derived for the one-electron model in the limit $\lambda \gg \xi$, it holds generally even for the many-body cases [48]. Both types of magnetic dichroism can be explained as a result of the spin polarization induced by the excitation. At a certain takeoff angle, there may be strong preferential emission of a given spin component—say spin up—at one of the energy levels. When the magnetization is reversed, the spin polarization does not change, but the peak will be shifted due to the interchange of majority and minority spin directions in space. Therefore different intensity spectra will result from magnetization reversal. From Fig. 2.3, it is obvious that from lower binding energy to higher binding energy, $2p_{3/2}$ levels have a "plus/minus" shape and $2p_{1/2}$ levels have a "minus/plus" shape in the dichroic spectrum.

As discussed before, unpolarized light can be thought of as being composed incoherently of s and p polarized light. Whereas the s component gives no dichroic signal, the p component will generate dichroism as discussed before, so that there will be a magnetic dichroism using unpolarized light. Of course, due to the intensity contribution from the s component, the dichroic signal will be smaller than the MLDAD observed with pure p-polarized light. Note that the scaling factor is not necessarily exact one half, because the excitation matrix elements may have different values for s and p components.

Because this work is mainly concerned about MDAD from $2p$ levels using unpolarized light, it is reasonable to give the form for Δ_{MLDAD} here as:

$$\Delta_{MLDAD} = R_0 R_2 \sin^2\theta_k \sin 2\phi_k \sin(\delta_0 - \delta_2) \tag{2.23}$$

where R_0 and R_2 are the radial matrix elements for the s and d channels which are allowed for $2p$ photoemission, and δ_0 and δ_2 are the phase shifts for the two channels, respectively. The formula here is actually a special case of the formula (1) in Ref. [21]. In the geometry for p-polarized light with $q \sim \hat{e}_x$ and M along z, one can deduce from this formula that the dichroism $I_{MLDAD} \propto C^j_{221}(\vec{k}\cdot\vec{q})(\vec{q}\cdot\vec{k}\times\vec{M})$, where $C^j_{221} \propto \sin(\delta_0 - \delta_2)$. This formula is exactly the same as the eq.(2.23), and has been

widely used to describe the angular dependence of MLDAD, which is discussed in the introduction. From this formula it is clear that either interference or different phase shifts result in MLDAD. As discussed in the introduction, it is also clear that this result holds only for an oriented atom, and that there is no term related to the orientation of the crystal lattice in this formula.

Now it is necessary to shortly discuss magnetic dichroism with reversing the photon helicity for a fixed direction of magnetization (MCDAD). When the magnetization $\vec{M}$, photon wave vector $\vec{q}$, and photoelectron wave vector $\vec{k}$ all lie in the same plane, it is seen easily upon symmetry considerations that both the dichroism upon magnetization reversal and the dichroism from helicity reversal are identical, as far as only oriented atoms and no crystal lattice are considered.

3 Experimental aspects

3.1 Apparatus

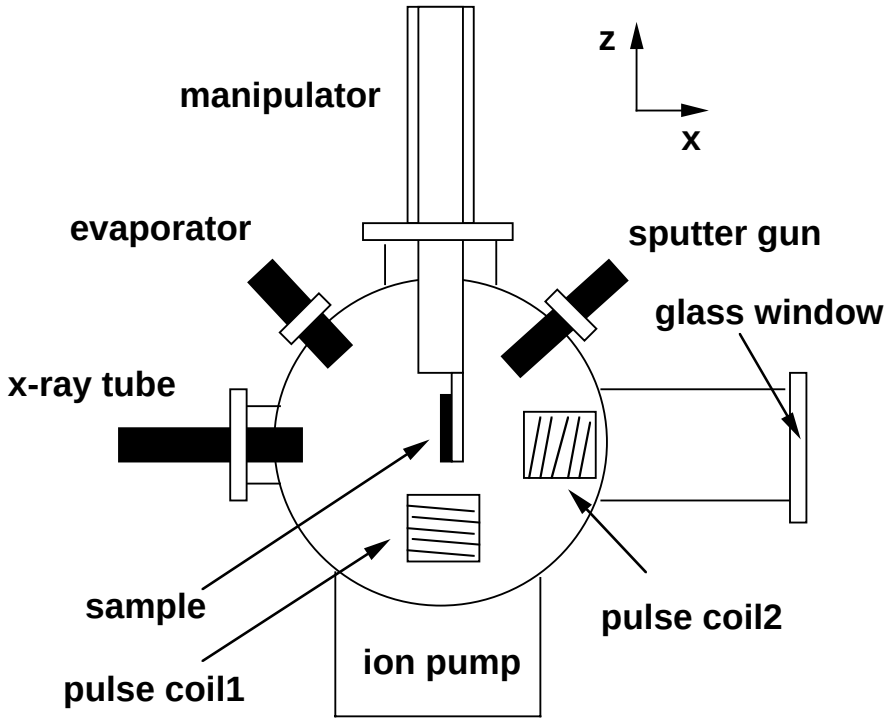

Figure 3.1: The schematic sideview of the experimental setup

The experiments in this thesis were performed in an ultrahigh vacuum (UHV) chamber, the schematic sideview and topview of which are shown in Fig. 3.1 and Fig. 3.2, respectively. With the ion getter pump, this chamber can reach a base pressure of 1×10^{-10} mbar. There is a cooling trap available for this chamber which can be cooled by liquid N_2, so that the base pressure then can be lowered to several 10^{-11} mbar.

The samples studied in this thesis were all prepared in this chamber. The substrate in the present experiments was an fcc Cu(001) crystal with a size of about 1 cm^2. Before the film growth, the substrate is cleaned by 1.5 kV Ar^+ bombardment using the ion sputter gun. With the e-gun set at 3 kV, AES spectrum can be recorded by a commercial hemispherical electron analyzer to check the cleanliness of the substrate. In order to improve the smoothness of the substrate surface, the sample was heated by electron beam bombardment to about 800 K for 2 minutes and then to 600 K for 5 minutes. After the annealing, the substrate was cooled down to room temperature naturally or by liquid N_2. The temperature of the sample was controlled by an N-type thermocouple attached to the sample holder. The Fe and Co sublimaters mounted

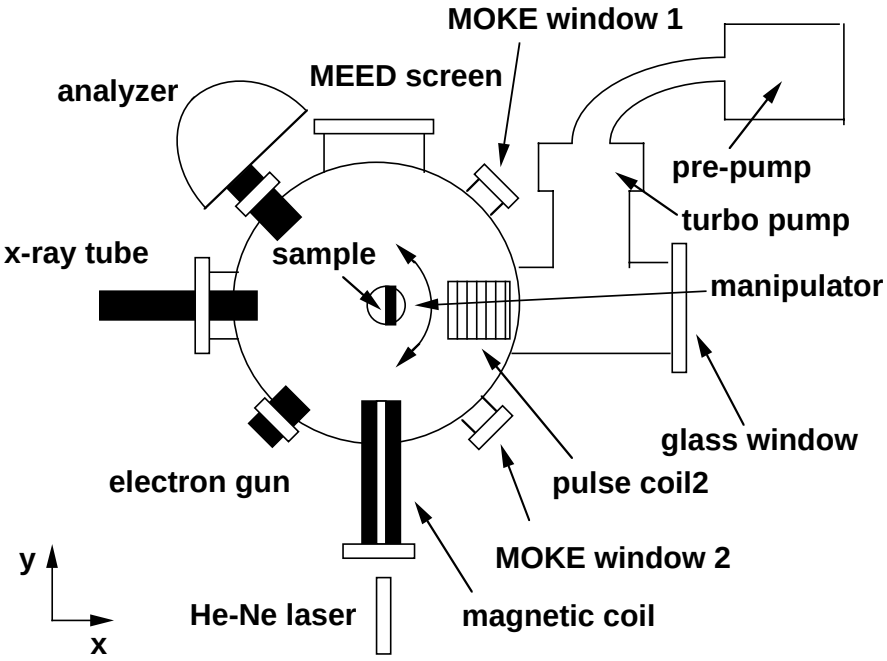

Figure 3.2: The schematic topview of the experimental setup

in this chamber are water-cooled evaporation sources without crucibles, where an electron beam is focused onto the tip of a high purity wire. By controlling the electron beam current and the ionized outgoing particle flux of the evaporators, very stable growth rates can be reached. During growth, using the Auger electron gun and the fluorescent screen MEED (medium energy electron diffraction) is performed to monitor the growth mode and to control the film thickness. To perform MEED, the image of the whole screen was taken by a CCD camera, which was connected to a computer. The intensity of the diffracted spots on the screen can be recorded by the computer during evaporation as a function of deposition time. After the growth, the film was checked again by AES to make sure that the film is clean, and to re-check the thickness of the film.

The MOKE (magneto-optical Kerr effect) setup in this chamber allows one to perform both polar and longitudinal Kerr effect measurements. The magnetic coil, shown in Fig. 3.2, with an iron core can reach a magnetic field of about 1500 Oe. It is driven by a bipolar power supply current-controlled by a computer. A He-Ne laser delivers a laser beam at wavelength 633 nm through the bore of the iron core onto the sample. By rotating the sample, the reflected laser beam from the sample can exit through MOKE window 1 or 2 for the polar and longitudinal mode, respectively. In this setup, the angles between the light incidence and the sample normal are $\sim$ 22.5° for the polar mode and $\sim$ 67.5° for the longitudinal mode, respectively. In the

MOKE experiment, the laser beam passes first through a polarizer filter, and is then modulated by an photo-elastical modulator to introduce a periodic modulation at 50 kHz of the light polarization, which oscillates from left circularly polarized to right circularly polarized light. The modulated laser beam is then incident on the sample, and the reflected light will pass through MOKE window 1 or 2. The outcoming light passes through another polarizer filter (the polarization of which is orthogonal to the first one), and is recorded by the photodiode. The modulation of the light allows here to use a lock-in system to measure the Kerr signal. This technique ensures a good sensitivity even with a film of just one monolayer coverage.

In the laboratory the light source for photoemission is a x-ray tube with a Mg anode ($\hbar\omega = 1253.6$ eV). It can be dismounted, and the chamber can be connected to a synchrotron beamline at the same port. The XPS spectrum is recorded by the same electron spectrometer as is used for AES.

The chamber contains also two coreless magnetic coils, which are called pulse coil 1 and 2 in Fig. 3.1 and Fig. 3.2. With a current pulse through these coils, a pulse magnetic field can be generated to magnetize the sample in x or z direction (cf. Fig. 3.1). The current pulse supplier is controlled by a computer and allows one to perform programmed magnetic dichroism measurements. With the x-ray tube, coil 1 underneath the sample was used to magnetize the sample in-plane for LMDAD measurements. With circularly polarized light from synchrotron radiation, both pulse coils were used to measure magnetic dichroism in different geometries. With circularly polarized light and pulse coil 2, it is also possible to carry out magnetic dichroism experiments in x-ray absorption.

Unfortunately there is no standard equipment to study the structure of the film. To study the structure by LEED (low energy electron diffraction), in some cases a preparation chamber was mounted on the top of this chamber with a longer manipulator. However, most of the work presented here was done with just the main chamber. Therefore the samples studied in this thesis (for example, Co/Cu(001)) are chosen because their structure is well-known, and the preparation conditions are controlled as described in the literature.

3.2 Light sources for XPS

This thesis is focused on the magnetic dichroism in core-level photoemission. Because the characteristics of the light source are very important in the photoemission process, this section will give a short introduction to the x-ray tube in the laboratory and the synchrotron facility ESRF.

3.2.1 x-ray tube

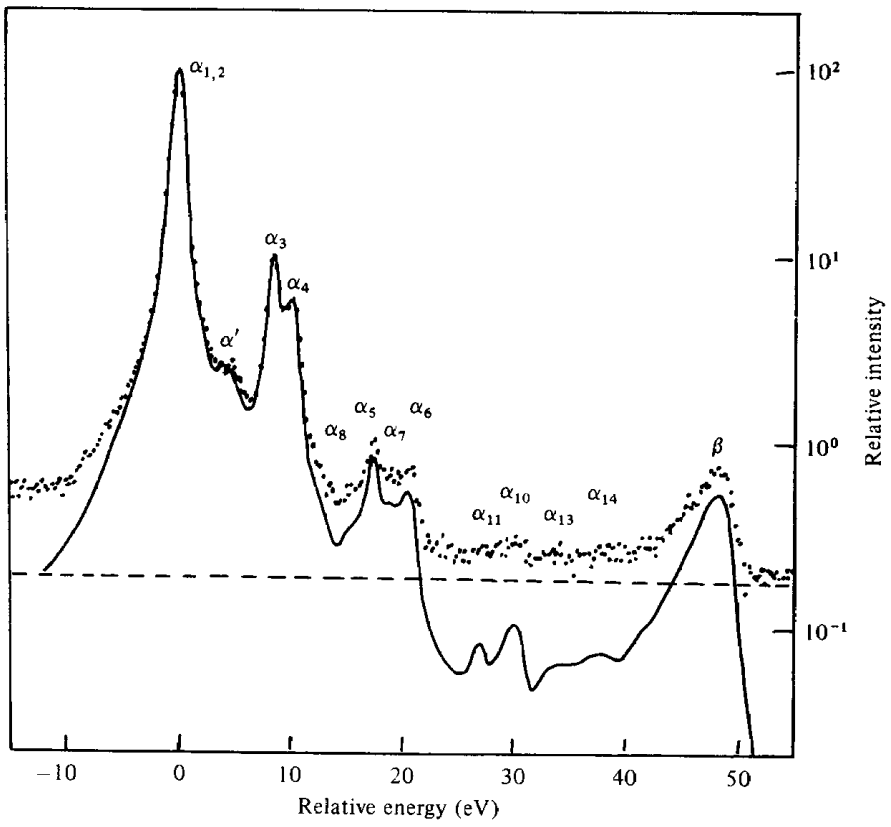

Figure 3.3: Mg K-shell X-ray emission spectrum. The full line shows the characteristic line emissions after subtraction of a constant background as shown by the dashed line. Note the logarithmic intensity scale. [49]

The x-ray tube in this thesis is a conventional tube with a Mg anode, as mentioned in the section before. The anode will be bombarded by the electrons with 15 keV energy to generate x-ray emission. These emission from the anode consists of characteristic line emissions associated with the filling of core holes created by the incident electron beam, superimposed on a continuum background up to the incident electron energy due to bremsstrahlung. In Fig. 3.3 shows a Mg K-shell x-ray emission spectrum with intensities on a logarithmic scale [49]. The electron energy of 15 keV is higher than the K-shell binding energy, and the unresolved doublet of $K_{\alpha 1,2}$ lines associated with the filling of the K-shell holes dominates the spectrum ($2p_{\frac{1}{2}} \rightarrow 1s$ for $K_{\alpha 1}$ and $2p_{\frac{3}{2}} \rightarrow 1s$ for $K_{\alpha 2}$). Mg is chosen as a good anode material due to its low bremsstrahlung background, its dominating $K_{\alpha 1,2}$ line emission, and also due to its good heat conductivity. There are still some other emission lines in the spectrum. However, except for the doubly ionized $K_{\alpha 3,4}$ emission, which gives rise to a photoelectron satellite of about 8% of the main intensities at a 10 eV higher kinetic energy,

others lines are generally small ($\leq$ 1%). Another important characteristics of the x-ray source is the width of the emission line. The full width at half maximum of the dominant $K_{\alpha 1,2}$ line is about 0.7–0.8 eV, which limits the energy resolution of the present XPS spectra.

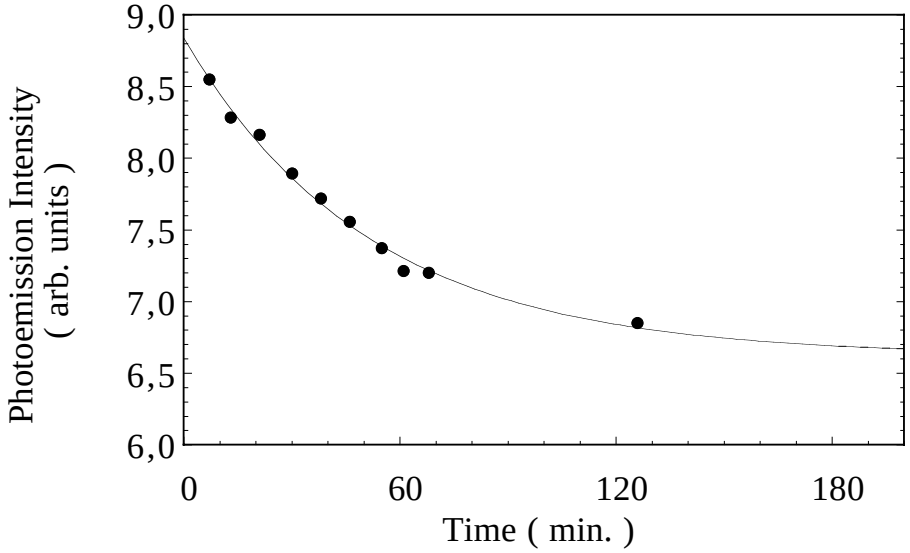

Figure 3.4: The maximum photoemission intensity of Co $2p_{\frac{3}{2}}$ at normal emission from 6 ML Co/Cu(001) film (filled circles) as a function of the time after the x-ray tube is switched on. The solid line is an exponential function fit for the data points. The film is grown at room temperature and the photoemission is measured at room temperature. The experimental setup of photoemission is shown later. A typical Co photoemission intensity spectrum of Co $2p$ core levels is reported later.

Because the dichroic spectra are the difference of photoemission intensity between reversing magnetizations in the present experiments and the photoemission intensity depends on the light intensity, it is necessary to discuss the origin and consequences of intensity changes of the x-ray tube. In the x-ray tube most of the electron energy is converted into heat, which raises the temperature of anode and thus raise the pressure due to outgassing, especially the pressure in the tube. Even with the help of the cooling system for the anode, some temperature and pressure raise still cannot be avoided. These raises are time-dependent: when the x-ray tube is switched on, the temperature and pressure raise quickly in the beginning, then this increase will be slowing down. After more than one hour, the temperature will reach a stable value due to the cooling system. Also the pressure will be stable. This temperature and pressure raises cause the variation of x-ray intensity. It has been found that the x-ray intensity will drop down after the x-ray tube is switched on. The reason can be some small changes of x-ray tube parts due to temperature effects or the drop of efficiency of the electron beam due to the worse pressure in the x-ray tube. In order to check the

magnitude of this effect, the intensity maximum of Co $2p_{\frac{3}{2}}$ from 6 ML Co/Cu(001) is measured at normal emission angle as a a function of time after switching on the x-ray tube with an emission current of 45 mA. The result is shown in Fig 3.4. It is seen clearly how the photoemission intensity drops down quickly in the beginning, and then this drop slows down. This time-dependent drop of photoemission is attributed to the intensity drop of the x-ray, because a similar time-dependent effect has not been found using circularly polarized light from the synchrotron radiation in ESRF. This slow change of the x-ray intensity is not so important in a dichroism measurement, as the analysis process used will minimize such an effect by a rescaling procedure. (In this procedure the spectra are rescaled relative to the two magnetizations, in order to have the two spectra coincide, both in the higher and lower binding side of the 2p levels, where no dichroism is expected.) However, in some cases the time-dependent change of the light intensity causes the baseline of the dichroism spectra to be tilted, which cannot be compensated for using simple rescaling. In the next chapter, a new method called template fit will be discussed, which can correct the tilted baseline in most cases when the time-dependent intensity change is linear with respect to time. In this thesis, valuable information is also drawn from the photoemission intensity (forward scattering), so that it is surely very important to correct the photoemission intensity to the x-ray flux to avoid artifacts.

3.2.2 Circularly polarized light at ESRF

The interaction of circularly polarized light with material has been a fascinating field. Spectroscopies studies such as spin resolved photo- and Auger-emission, circular dichroism, or magnetic microscopy need the synchrotron radiation source due to its high degree of polarization, a high flux, and a tunable photon energy. Especially circularly polarized light in the soft x-ray energy range is only available at synchrotron radiation sources. In this thesis, core-level photoemission measurements using circularly polarized light were performed at the European Synchrotron Radiation Facility (ESRF) at beamline ID12b. The planar helical undulator HELIOS I is used to produce intense radiation polarized circularly as well as linearly at this beamline. It consists of an upper and a lower planar magnetic array creating horizontal and vertical magnetic fields, respectively, along the path of the 6 GeV electron beam of the storage ring. By shifting the upper array longitudinally with respect to the lower one changes the horizontal and the vertical component of the radiation field vector. In this way the helicity can be changed. In the present experiments only left handed circularly polarized light was used. The degree of polarization at 900 eV is about 90% [50]. The radiation of the undulator's first harmonic, covering the range from 540 eV to 8 keV, is monochromatized using a "Dragon"-type monochromator [51] with a spherical

grating at grazing incidence operating from 500 eV to 1.6 keV. The energy resolution of the light in the experiments presented here was set to $\sim 3 \times 10^{-4}$. The beam size at the sample is smaller than 1×1 mm^2. At 100 mA ring current, the photon flux on the sample is $\sim 10^{10} - 10^{12}$ photons/second. Under these conditions the photoemission intensity using circular light from this beamline is about 10 times higher than using the Mg anode x-ray tube in the laboratory. The high intensity of the beamline and its monochromatized character allows one to perform photoemission on ultrathin films very quickly with lower background (compared with x-ray tube, which has spurious photons contributes the background), especially in the sub-monolayer range.

4 MDAD in core-level photoemission

4.1 Basic review and introduction of forward scattering

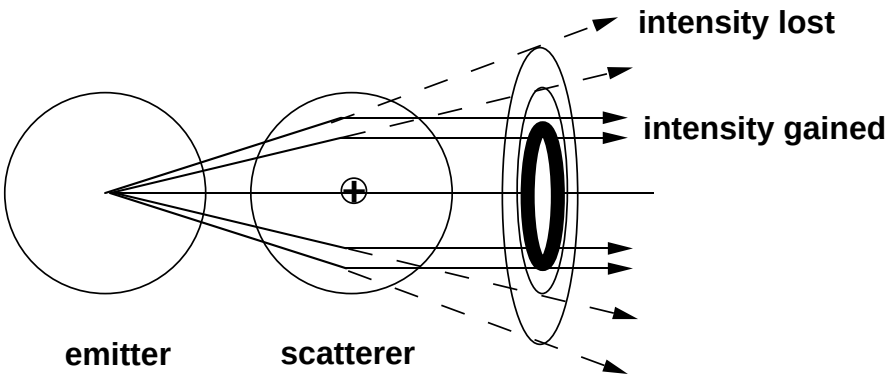

Figure 4.1: A classical diagram explaining forward scattering. The attractive potential of a scattering atom deflects a ring of solid angle into the forward direction. Since this part of the scattered wave is in-phase around the cylindrically symmetric axis, a constructive interference occurs and produces an enhanced intensity along the interatomic axis. [52]

As already mentioned in the introduction, diffraction effects in MDAD of $2p$ photoemission using unpolarized light from a Mg K_α anode (1254 eV) are mainly due to forward scattering of photoelectrons. The reason is that the photoemission from Fe or Co $2p$ levels (binding energies $\sim$ 700-800 eV) has kinetic energies of $450 - 550$ eV, where forward scattering dominates the photoelectron scattering [53, 54]. When photoelectrons with these kinetic energies are emitted from a crystal surface, enhanced intensities are observed along the interatomic axes connecting the emitting atom with its nearest and next-nearest neighbors. This is so-called forward-scattering or forward focusing [52-54]. A semiclassical description of such an effect is plotted in Fig. 4.1 [52]. The outgoing photoelectron wave is deflected into the forward direction from its initial trajectory by the attractive potential of an atom next to the emitter. Because this part of the scattered wave is in-phase with the direct wave, a constructive interference occurs and produces an enhanced intensity along the forward direction. This effect will let the intensity of the outgoing photoelectrons have a strong angular dependence around the low-index crystallographic directions. Since electrons emitted by the atoms in the top atomic layer at the surface do not exhibit such forward-scattering enhancements, this effect is an excellent diagnostic of whether or not a particular kind of atoms is located in lower layers. For such atoms, forward scattering will offer valuable information about the local structure around the emitting atom. Therefore it can be used as a probe of short-range order in thin films. As discussed

in the introduction, it will be shown later in this thesis that by combining this technique with magnetic dichroism structure and magnetism of magnetic thin films can be studied simultaneously.

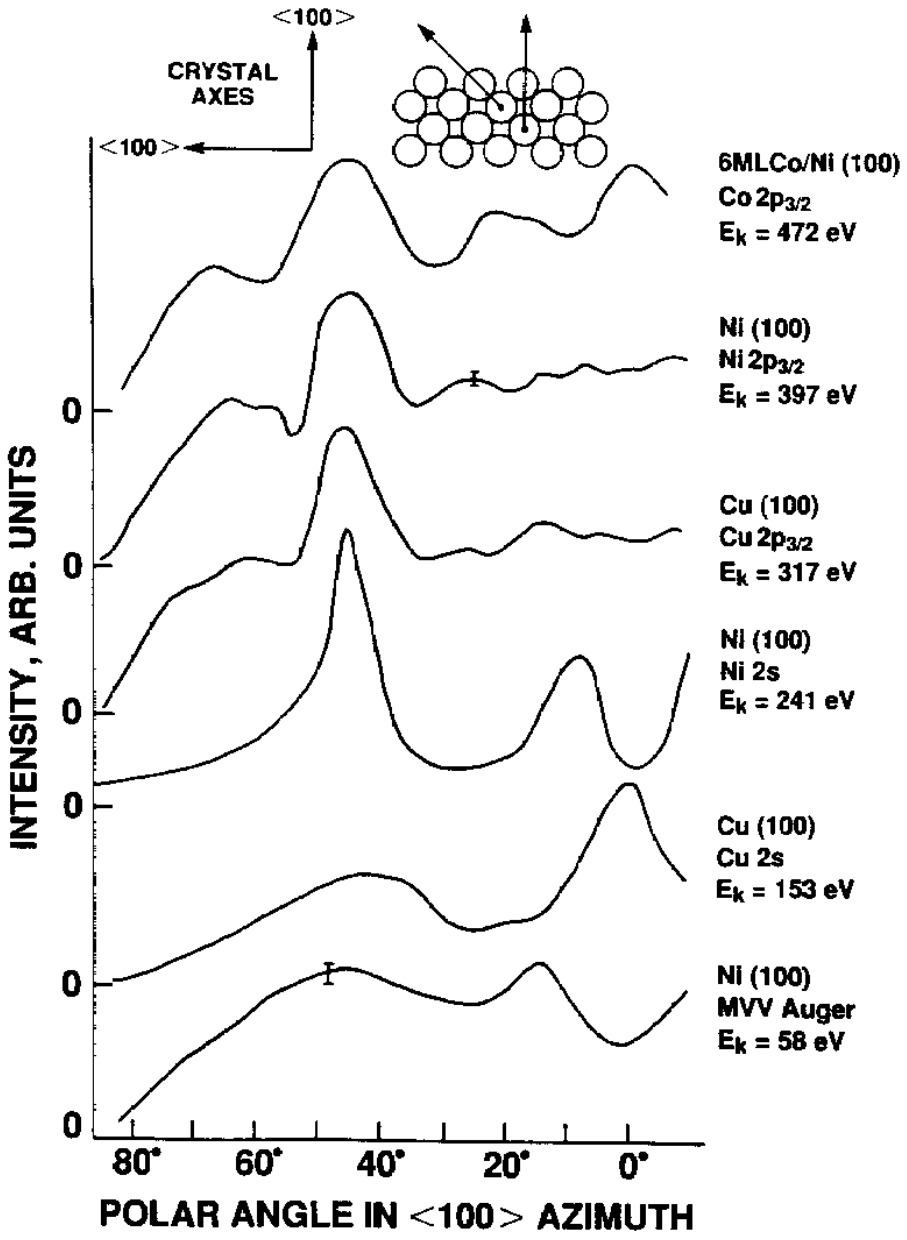

Figure 4.2: The kinetic-energy dependence of the forward-scattering peaks is illustrated using the indicated core levels and Auger line from isomorphic fcc (100) crystal surfaces (using Cu(100), Ni(100), and a 6 ML epitaxial film of Co deposited on Ni(100)). The inset at the upper right is a profile of the surface in the azimuth in which the data is recorded, <001>, indicating the origin of the 0° and 45° peaks. (from Ref. [57])

The scattering of photoelectrons depends strongly on the electron kinetic energy.

With increasing energy, the electron must come closer to the core to be significantly scattered, which means less photoelectrons will be scattered. Therefore, on the one hand, forward scattering itself inherently depends on the electron kinetic energy. On the other hand, other scattering processes which could affect the forward-scattering peaks also have a strong dependence on the electron kinetic energy. For example, at energies lower than 50 eV, there is a large amount of electrons even scattered backwards [55]. In contrast, very few electrons are backscattered at higher energies [55]. Although forward scattering accounts for the most prominent peaks in the angular distribution of the photoemission from crystalline samples at kinetic energies of several hundred eV, it should be noticed that some other–generally weaker–peaks can appear which are not related to forward-scattering. Among the most common of these intensity maxima are the ones arising from first-order constructive interferences [56]. This happens when the scattered wave has a phase shift of exact by 2π with respect to the direct wave along a certain direction. It complicates the angular distribution of the XPS emission, especially when two first-order constructive interferences overlap, for example, in an fcc lattice in a direction midway between the nearest and next-nearest neighbor axes [56]. Fig. 4.2 shows the kinetic-energy dependence of the forward-scattering peaks for samples having a common crystal structure (fcc <100>). Above 241 eV the forward-scattering peak at 45° (along the nearest-neighbor axis) dominates. At the same time, the forward-scattering peak at 0°, corresponding to the next-nearest-neighbor axis, only appears at 472 eV. At even higher energies the forward-scattering peaks gradually become narrower and less prominent (as can be understood from the fact that fewer electrons will be scattered). At low kinetic energies, the emitted wave going along 45° can be scattered into 0° and interferes with the forwardly scattered wave along <100>. The phase of this contribution differs in most cases from the forward scattered wave. This is the main reason why at a kinetic energy of 241 eV at 0° there is no forward-scattering. For higher kinetic energies, this interference becomes less important, because the probability for such 45° diffraction falls down quickly with increasing energy. At higher kinetic energies, forward scattering is generally the dominant contribution to the emission intensity along rows of atoms. This gives the possibility to use it as a probe for ultrathin films. For a thick film the XPS contribution from deeper layers is more isotropic due to multiple scattering, and the forward-scattering signal comes mostly from several layers at the surface [53]. As the number of scattering atoms above the emitter increases, the initial conditions for forward scattering become increasingly restrictive. Due to multiple scattering the trajectories of the electrons are no longer focused into the forward direction but also pass through adjacent rows of atoms and get scattered away. This defocusing effect diminishes the intensity of the forward-scattering peak and narrows the width of the

intensity peak that remains [58]. However, due to the limited mean free path length, the intensity of the photoemission signal will drop down quickly with depth, and the forward scattering from the first several layers will dominate in a single-element film. In this case, the defocusing effect is only of minor importance.

4.2 Co/Cu(001)

4.2.1 General aspects

Bulk cobalt assumes a stable hcp structure below 690 K. Only above 750 K bulk Co changes to the fcc phase. The fcc phase of Co can be stabilized around room temperature on fcc Cu(001), which has a lattice mismatch of 1.9%, at least up to 10 ML. As discussed in section 3.1, the Co films in this work were grown on Cu(001) at room temperature. With MEED, intensity oscillations can be observed during the Co evaporation, which indicates a nearly layer-by-layer growth mode, in agreement with the literature [22]. Like in the literature [23], it is also observed that the first oscillation is smaller than the second one. This is attributed to the presence of some second ML islands before completion of the first ML [22]. After 2 ML the growth mode is a good layer-by-layer mode. The structure of Co has been studied by many groups (for example: Refs. [24-26]). It has been found that Co adopts the lateral Cu(001) spacing ($a = 2.55$ Å) with a vertical interlayer contraction. This is the so-called face centered tetragonal (fct) structure. A LEED study indicated that the interlayer spacing of the topmost layer of the Co films is 6% contracted compared with Cu, while the contraction of the layers underneath is about 3% [26]. There are also a lot of studies on the magnetic properties of Co/Cu(001) films (for example: Refs. [27, 28]). The Curie temperature is found to be strongly dependent on the film thickness in the monolayer regime. The Co films were found to have a remanent magnetization always lying within the film plane at even very low thickness ($\sim$ 1.5 ML with $T_c \sim 130$ K) [27]. It was also found that there is a pronounced in-plane four-fold anisotropy which was suggested to be due to the strain-induced magnetoelastic anisotropy [22, 29]. In the present experiments, it was found that it needs higher magnetic fields to fully magnetize the Co films along the hard axis <100> than along the easy axis <110>. The remanent magnetization along all in-plane directions, however, was found to be equal to the saturation magnetization. This in-plane remanent magnetization of Co/Cu(001) films allows a study of these films with MDAD using unpolarized light.

Fig. 4.3 shows the setup of the MDAD experiment using unpolarized light. The magnetization direction **M** is oriented along the <100> direction of the fcc Cu substrate. The angle between the direction of the incident photons **q**, and the outgoing photoelectrons **k** is kept fixed to 45°. By supplying a pulse current through pulse

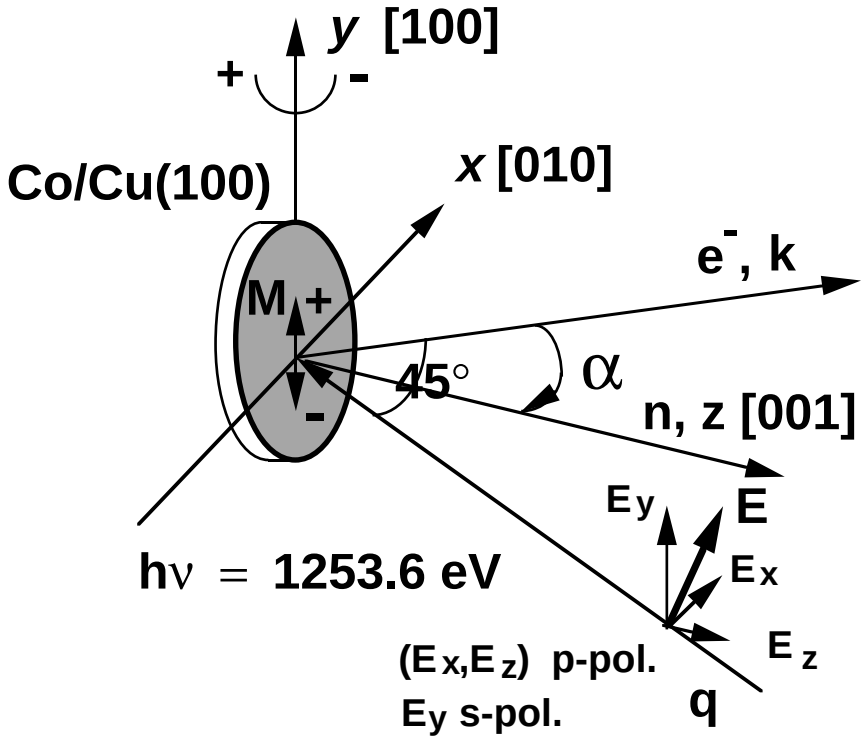

Figure 4.3: The experimental setup

coil 2 underneath the sample, the sample was magnetized along <100> direction (see Fig. 3.1 in the section 3.1). By reversing the current direction, the magnetization of the sample can be reversed. The fully remanent magnetization of sample was checked by MOKE before, during and after the MDAD measurement by the following procedure. After the sample is magnetized by a vertical pulse current along <100>, the sample azimuth is rotated by 90° to have the <100> axis in the horizontal plane (because the MOKE coil is also in the horizontal plane). A MOKE experiment is then performed. Because the value of the Kerr signal corresponds to the film magnetization, the value of the latter after applying the pulsed magnetic field along the <100> direction can be determined from the starting point in the MOKE loop.

The MDAD spectra were taken as two interleaved sets of scans with opposite magnetization directions. The magnetization was reversed before each scan by supplying reversed current pulse through pulse coil 2. The dichroism is quantified in terms of the intensity asymmetry, defined as $(I^+ - I^-)/(I^+ + I^-)$, where I^+ and I^- are the photoemission intensities for opposite sample magnetization. The MDAD spectra were collected for different emission angles α with respect to the surface normal $\mathbf{n}$ by simply rotating the sample around the axis parallel to the direction of magnetization. Normally each intensity scan at one angle was performed from lower to higher kinetic energies with a step width of 0.32 eV and a counting time for each point of 1 second.

To cover the energy range for Co $2p$ photoemission (440-485 eV), each intensity scan for one magnetization direction normally takes 3 minutes. The number of scans for one measurement depends on the intensity and the signal-to-noise ratio in the asymmetry spectrum. For 5 ML Co/Cu(001), the Co $2p$ photoemission intensity permits one to reach a good signal-to-noise ratio in an asymmetry spectrum in about 20 min with a total of $\sim 10^6$ counts for the Co-$2p_{3/2}$ intensity peak. When the film is thinner so that the count rate is lower, the time for each spectrum was extended. In the experimental geometry of Fig. 4.3 MDAD using unpolarized radiation is equivalent to MDAD using linearly polarized light. The use of a synchrotron radiation facility is thus not required.

4.2.2 MDAD of 5 ML Co/Cu(001) at different temperatures

In Fig. 4.4a Co-$2p$ intensity spectra for the two opposite directions of magnetization I^+ and I^- for a 5 ML Co/Cu(001) film are reported at normal emission angle ($\alpha = 0°$). The spectra have been collected at a sample temperature of $T = 100$ K. The film was grown at room temperature. The intensity contribution seen at the low binding energy side of the Co-$2p_{3/2}$ line has been subtracted as a constant background. Then the two spectra were rescaled by a constant factor in order to have identical intensity at the higher binding side of the $2p$ levels, where no dichroism is expected. In this way any artifacts in the dichroic spectra caused by the change of the experimental conditions during the measurement, such as the change of the x-ray intensity, can be minimized. The binding energy from literature is 793 eV for $2p_{1/2}$ and for 778 eV $2p_{3/2}$ [59]. While the Mg K_α x-ray source used in this work delivers unpolarized light at 1253.6 eV, the spectra of the Co $2p$ level are measured at kinetic energies between 440–485 eV. The spectra presented here refer to a binding energy scale relative to the energy position of the Co-$2p_{3/2}$ peak in the intensity spectra, fixed as zero of the energy scale. They show the two spin-orbit split $2p$ levels, $j = \frac{3}{2}$ and $j = \frac{1}{2}$, separated by ~ 15 eV, which is consistent with literature [59]. A broad structure centered at ~ 4 eV (marked in Fig. 4.4a with an arrow) is also clearly seen. It presents higher intensity for magnetization "down" (I^-). The spectra reported here agree qualitatively well in terms of lineshape and energetic position with others obtained in earlier reports at the same Co thickness [15]. The $2p$ lineshapes appear slightly asymmetric, with the higher binding energy side of the lines enlarged, in good agreement with the Doniach-Šunjić-type lineshape [60]. As discussed in the section 2.1 this is due to relaxation processes in photoemission.

In Fig. 4.4b the asymmetry function of the two intensity spectra is reported. As mentioned before, the asymmetry is defined as $A = (I^+ - I^-)/(I^+ + I^-)$. I^+ and I^- are the intensities after the rescaling procedure. The shape of the calculated dichroic

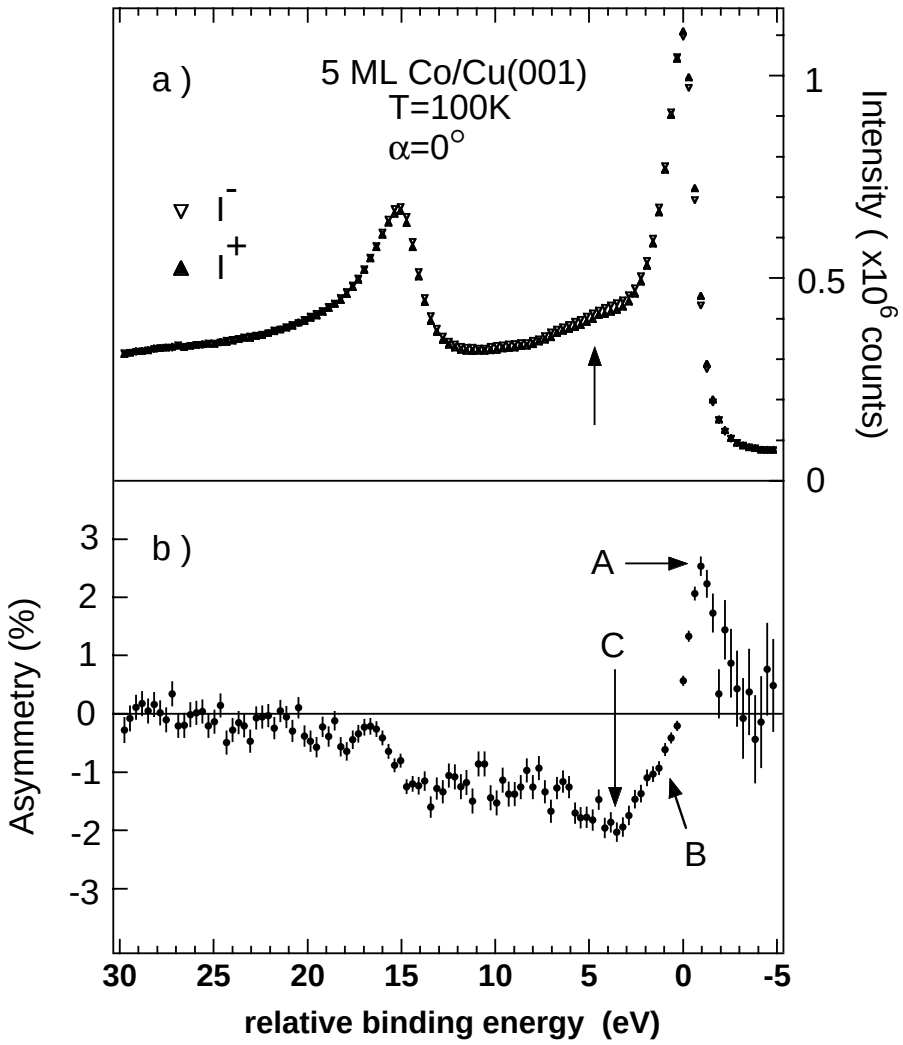

Figure 4.4: a): Co-2p intensity spectra for both magnetizations (I^+ and I^-), measured on a 5 ML Co/Cu(001) at the sample normal emission and 100 K. The arrow marks the position of a correlation induced satellite. b): Dichroic asymmetry spectrum calculated from the photoemission intensity spectra of a). Features A and B indicate the "plus" and "minus" features of the Co-2$p_{3/2}$ dichroism, respectively. Feature C marks the position of a superimposed negative peak.

asymmetry presents the typical "plus/minus " feature of the 2p lines. In the case of the $j = \frac{3}{2}$ level, the "plus" feature at about -1.1 eV is very clear (feature A in fig. 4.4b), whereas the "minus" feature appears as a shoulder at about 1.5 eV (feature B in Fig. 4.4b) on a wide negative structure. For the $j = \frac{1}{2}$ level the order of "plus/minus" is reversed, which is consistent with the one electron theory. However, the asymmetry presents clearly only the "minus" feature centered at ~ 14 eV.

In analogy with previous magnetic dichroism investigations using linearly polarized [12, 18] and unpolarized light [15], the dichroic feature centered at -1.1 eV can be attributed to the intensity difference in emission mainly from the $m_j = \pm 3/2$

projections of the Co-$2p_{3/2}$ core level. The negative shoulder at about 1.5 eV has then to be attributed to the same difference, and the "minus" peak centered at ~ 14 eV to the intensity difference in emission from the $m_j = \pm 1/2$ projections of the Co-$2p_{1/2}$ core level. The size of the "minus" at $2p_{1/2}$ is much smaller compared with the "plus" feature at $2p_{3/2}$. The reason is that there are a lot of secondary electrons at the higher binding energy side of $2p_{3/2}$ due to inelastic scattering. This intensity contribution from secondary electrons reduces the measured dichroic asymmetry at $2p_{1/2}$. Although at $2p_{1/2}$ the accompanying "plus" feature should be smaller than the "minus" feature because of more secondary electrons at higher binding energies, it should be still present. The small upward bump at ~ 17 eV can be identified as this "plus" feature. That it falls below zero is a hint towards an artificially tilted baseline, which is not corrected by the simple rescaling procedure. A method to overcome this problem will be introduced in this subsection.

The dichroism between the two levels is negative with a superimposed negative peak at $\sim$ 3 eV (feature C in Fig. 4.4b), that reflects the difference in emission intensity for the two magnetizations in this energy region. From one electron theory, there should be no dichroism in this region. The observed dichroism must thus be explained by many-body effects.

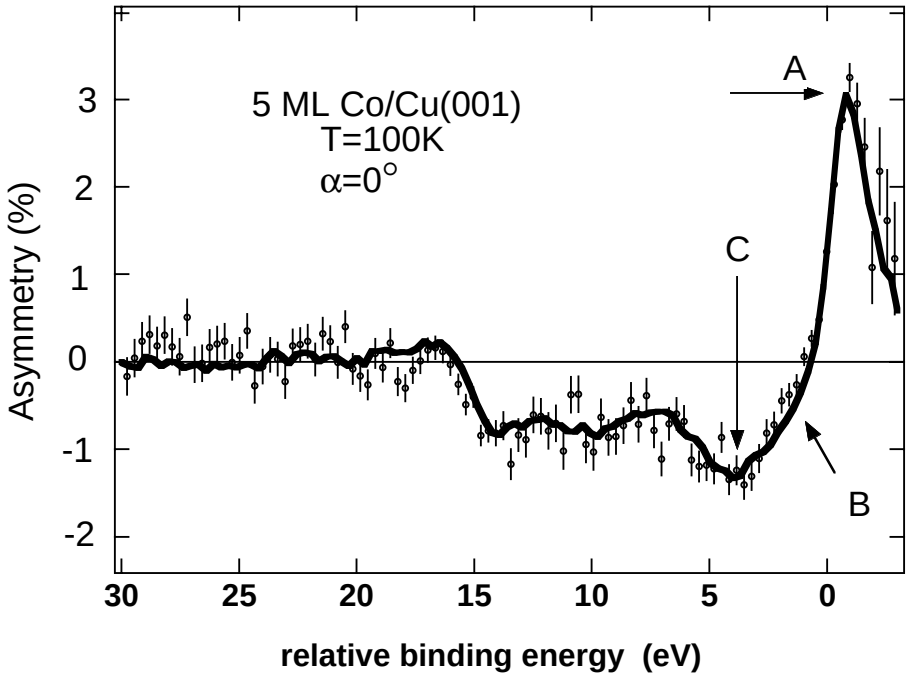

Figure 4.5: Dichroic asymmetry spectrum as Fig. 4.4b, but after baseline correction by the template fit (filled circles). The solid line is the scaled template spectrum. The features A, B, and C are as in Fig. 4.4b.

Because the goal is to study the angular dependence of the magnetic dichroism,

and these angular dependencies sometimes can be rather weak, it is crucial to have a reliable criterion to fix the baseline. In the experiments, the intensity of the x-ray radiation will change, especially in the first few hours after starting the source (cf. Fig. 3.4). The MDAD spectra are taken as two interleaved sets of scans with opposite magnetization directions. In each scan the spectrum is measured from lower to higher kinetic energies. Therefore the time-dependent variation of the intensity and some other changes of the experimental situation during the measurement can cause the baseline of the asymmetry spectrum to be tilted, which cannot be corrected just by simply rescaling. As the time needed for the acquisition of one dichroism spectrum is short compared to the time constant of the experimental decay of the x-ray intensity (cf. Fig. 3.4), the baseline can simply be assumed to have a linear slope. Such a linear slope in the baseline is also seen from Fig. 4.4b, where the baseline seems to be tilted down at lower binding energies. In all the reported MLDAD experiments of Co films in this thesis, the shape of the asymmetry spectra of the $2p$ levels is very similar (this will be demonstrated later). Performing a more systematic data analysis to overcome the tilted baseline, a **template** asymmetry spectrum was used to fit every asymmetry spectrum $Asy(E)$. This procedure will be called "template fit" in the following. The idea is to minimize the chi-square:

$$\chi = \sum_i ((Asy(E_i) - c_0 \cdot \mathbf{template}(E_i) - c_1 - c_2 E_i)/\sigma_i)^2 \tag{4.1}$$

by variation of the parameters c_0, c_1, and c_2. Here i is the index for the data points, E_i is the respective binding energy of data point i in this asymmetry spectrum, and σ_i is the standard deviation for each data point from Poisson statistics correlated to the count rate N_i by $\sigma_i = 1/\sqrt{N_i}$. In this case, the parameter c_0 is the scaling factor for this dichroic asymmetry spectrum with respect to the template spectrum, c_1 a constant offset of the baseline, and c_2 responds to the slope of the tilted baseline. In this way, the baseline shape can be systematically adjusted by the parameters c_1 and c_2 to the baseline of the template curve. The corrected data points can then be obtained from the results of $Asy(E_i) - c_1 - c_2 E_i$. As the parameter c_0 describes the relative size of the magnetic dichroism, it can be used to study the angular dependence of the magnetic dichroism for all spectra.

Now the most important point is to find a suitable dichroic asymmetry spectrum as template for the analysis of the Co asymmetry spectra in this work. The best candidate must have very high counts to have a good signal-to-noise ratio. Because 10 ML is the thickest Co film that was measured, and thus shows the highest counts rate and therefore the best signal-to-noise ratio, the spectrum of 10 ML Co/Cu(001) is a good candidate. As mentioned before, spectra at different emission angles and different thicknesses exhibit the same shape, so the average of asymmetry spectra of

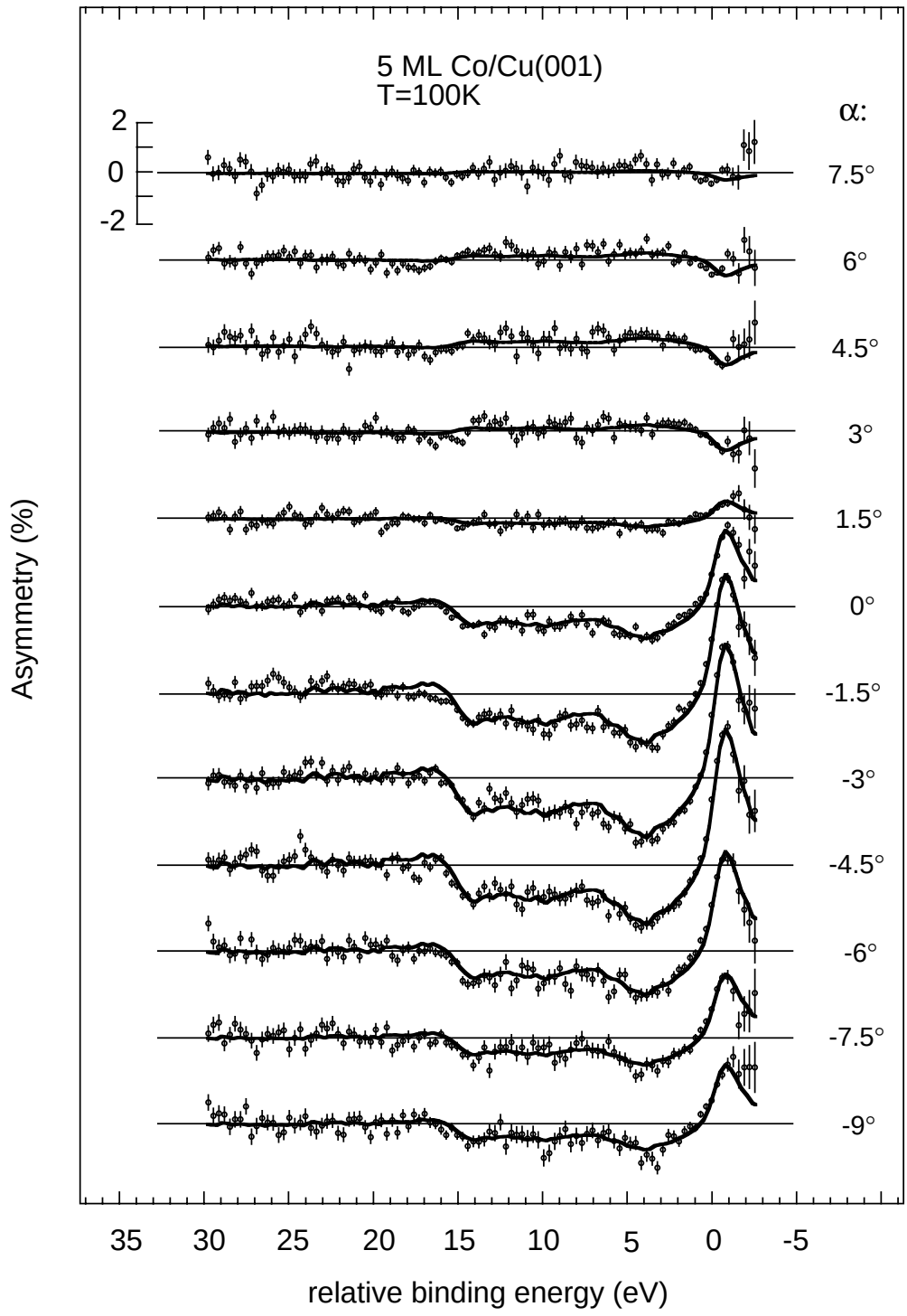

Figure 4.6: Dichroic asymmetry curves after correction of the baseline (filled circles) for a 5 ML Co/Cu(001) film at the emission angles indicated on the right hand side. The solid line is the template curve scaled with a constant parameter c_0 at each angle. The asymmetry scale is in percent, and it is reported in the upper left side of the figure as reference. The curves are horizontally offset for clarity. The horizontal lines indicate zero asymmetry for each curve.

the 10 ML Co film at emission angles 0°, −1.5°, −3°, −4.5°, −6° and −7.5° was used as template. In this way, a good signal-to-noise ratio for the fitting purpose is obtained. The template fit of the data of Fig. 4.4 is shown in Fig. 4.5. The corrected data are shown as filled circles, the template spectrum times the parameter c_0 as solid line. From Fig. 4.5 it is clear that the template curve fits the 5 ML data well. Note that the baseline is now well calibrated within the error-bars, and a tiny "plus" feature is now present at $2p_{1/2}$. Besides being much smoother, the template spectrum is similar to Fig. 4.4b in all details. It is here noticeable that the fit parameter c_0 relates to the total spectrum and not only to one or two data in the spectrum, therefore, the size of the dichroism is now represented by c_0, and is independent from baseline uncertainties.

In Fig. 4.6 the dichroic asymmetry spectra for the 5 ML Co/Cu(001) film at 100 K after baseline correction cover an emission angle range of $\alpha = -9°$ to $\alpha = +7.5°$. The data points (filled circles) are corrected with a line slope $c_1 + c_2 E_i$, as explained above. The solid line is the template asymmetry spectrum scaled with a constant factor of c_0 at each angle. It is obvious that the template fits all the spectra well within the experimental error bars. The asymmetry curves of Fig. 4.6 present the "plus/minus" and "minus/plus" features related to the $j = 1/2$ and $j = 3/2$ levels, respectively. An energy shift of these features as a function of α, as it was observed in Ref. [17], cannot be confirmed from the present data within the spectral resolution. Fig. 4.6 shows that the size of the asymmetry varies strongly even when the emission angle is changed by a very small value around the surface normal direction $\alpha = 0°$. The asymmetry even changes its sign at $\alpha \approx 3°$.

As mentioned before, the scaling parameter c_0 of the template fit is a good measure of the size of the dichroism. Therefore, it is very suitable to study its angular dependence with the emission angle α. In order to give an absolute value of the dichroism, the parameter c_0 scaled with the maximum peak-to-peak asymmetry of the template curve, which is the maximum peak-to-peak asymmetry at each emission angle, is used in this study. As discussed in the previous section, the effect of forward scattering can be studied by following the photoemission intensity of the $2p_{3/2}$ peak as a function of the emission angle. Except for scattering, other mechanisms influencing the photoemission intensity in the present geometry are the change of the transition matrix element due to the change of the incidence angle with respect to the surface normal, and the influence of the different path lengths of the photoelectrons at different emission angles (which will be discussed later in the context of angular scans over an extended angular range). However, the angular range studied here is less than 20°, and the effect of forward scattering should dominate. This is proven in Fig. 4.7, which shows the angular distribution of the total intensity (by adding the I^+ and I^-) of the Co-$2p_{3/2}$ photoemission peak of 5 ML Co/Cu(001) at 100 K in panel a), and

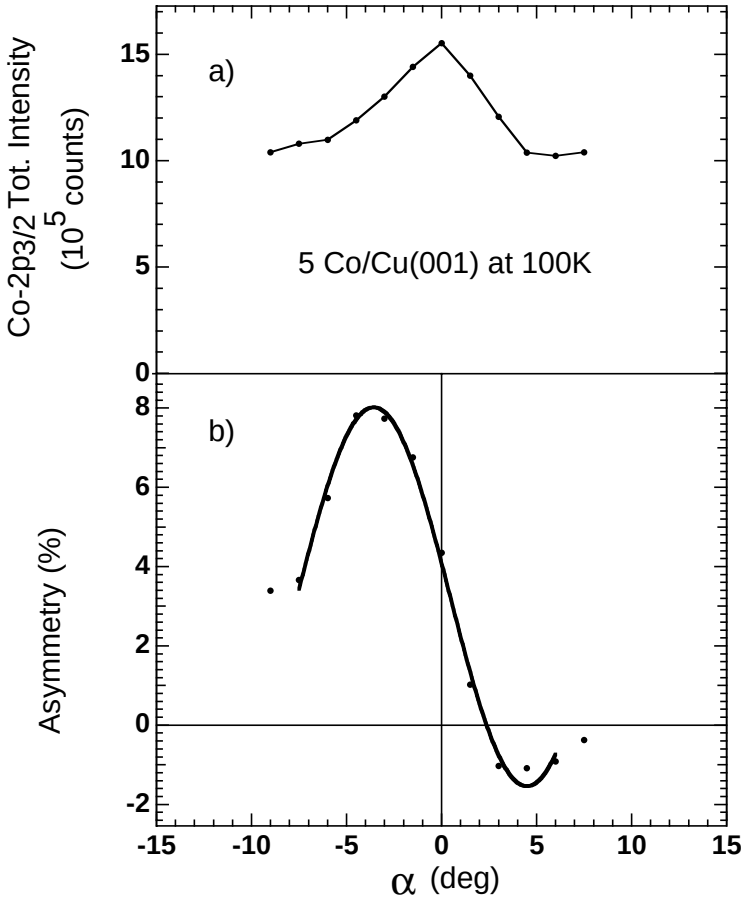

Figure 4.7: a): The angular dependence of the Co-$2p_{3/2}$ peak height ($I^+ + I^-$) on the emission angle α, measured on 5 ML Co/Cu(001) at 100 K. b): The angular distribution of the maximum peak-to-peak asymmetry, taken from the parameter c_0 of the template fit. The error-bars are included but too small to be recognized. The line is a guide to the eye.

the corresponding maximum peak-to-peak asymmetry taken from the parameter c_0 of the template fit in panel b). The angular distribution of the photoemission intensity in Fig. 4.7a exhibits a clear peak located at $\alpha = 0°$, which indicates strong forward scattering for the 5 ML Co/Cu(001) film along the <001> direction. As discussed before, Co films on Cu(001) have an fct structure adopting the lateral Cu(001) spacing with a vertical interlayer contraction. Therefore along the normal direction, which is the <001> axis of the Cu crystal, there should be strong forward scattering in a thick Co film such as 5 ML Co/Cu(001). This forward scattering proves that the film has a well ordered structure. Otherwise there would not be any enhancement of the photoemission intensity. In Fig. 4.7b, the angular distribution of the maximum peak-to-peak asymmetry presents a clear antisymmetric shape around normal emission.

As discussed in the introduction and section 2.3, in a simple free-atom description of the photoemission process, the magnetic dichroism using unpolarized light is only

governed by the angle between the light incidence direction and the electron emission direction. There is no relationship between the dichroism and the crystal lattice in that model. In the present experiment, this angle is fixed at 45°, and any variation in the dichroism upon changing the angle α must therefore be related to the crystal lattice. From Figs. 4.6 and Fig. 4.7b, it is clear that the dichroism varies strongly as α is varied around normal emission ($\alpha = 0°$). This cannot be explained by the free-atom model, and has to be related to final state effects or diffraction effects, which include the crystalline structure of the sample. As forward scattering dominates in the photoemission around the sample normal, the strong variation of the dichroism around normal emission immediately means that the forward scattering plays a dominant role in the diffraction effects.

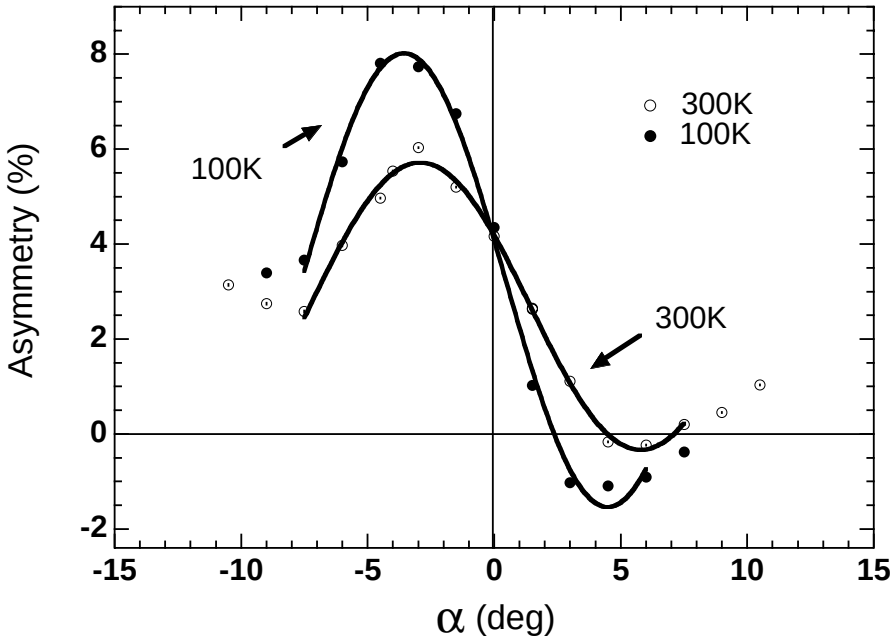

Figure 4.8: Angular distribution of the maximum peak-to-peak asymmetry, taken from the parameter c_0 of the template fit, of 5 ML Co at 300 K (open circles) and at 100 K (filled circles). The error-bars are included but too small to be recognized. The lines are guides to the eye.

As the temperature affects both the diffraction and the magnetism, it is now interesting to study the influence of the temperature on the angular dependence of MLDAD, in which there are diffraction effects. In Fig. 4.8, the angular dependences of the parameter c_0 from the template fit for the dichroic asymmetry spectra in 5 ML Co/Cu(001) at 300 K (open circles) and 100 K (filled circles) are shown in maximum peak-to-peak asymmetry. The data were taken from two different films, which were prepared under identical conditions at room temperature as discussed before. From Fig. 4.8, it is clear that the amplitude of the variation of the dichroic signal is reduced

at $T = 300$ K with respect to 100 K, but the signal at normal emission remains almost unchanged. This reduction of the variation amplitude must be due to the reduced diffraction effects at higher temperature.

4.2.3 MDAD of Co/Cu(001) at different thicknesses

In this subsection, Co/Cu(001) films with different thicknesses of 1.5 ML, 2 ML, 3 ML, 5 ML and 10 ML have been studied. 1.5 ML and 2 ML have been measured at a sample temperature of 100 K; 3 ML and 5 ML have been measured both at 100 K and 300 K; 10 ML has been measured only at 300 K.

In Fig. 4.9 and Fig. 4.10 the dichroic asymmetry curves for the 2 ML and 1.5 ML Co films are reported, respectively. In both curves, the data points (open circles) were obtained by the same analysis process as in the previous subsection. The solid lines in the spectra are the scaled template curves as in Fig. 4.6. The scaling parameter c_0 was obtained from the template fit to the dichroic asymmetry spectrum in each film at every emission angle. It is clear that the template asymmetry spectrum fits well every spectrum in both figures, although statistics is worse than for 5 ML (cf. Fig. 4.6). For both 2 ML and 1.5 ML films, the emission angle was varied between $-9°$ and $+7.5°$, like for the 5 ML film of subsection 4.2.2. The 2 ML Co film exhibits a weaker variation of the asymmetry with the emission angle compared with the case of the 5 ML Co film, and the dichroism is reduced as compared to the 5 ML case. For the 1.5 ML Co film the spectra for all the angles are almost identical to each other, and the dichroism is quite independent of α except the two spectra with $\alpha \geq 4.5°$. Also the dichroism is further reduced with respect to the 2 ML case.

From looking at the series of asymmetry spectra of 5 ML, 2 ML, and 1.5 ML, it becomes clear that the angular variation of the dichroism is reduced when the thickness is reduced from 5 to 1.5 ML. In order to show how the dichroic signal responds as a function of thickness, in Fig. 4.11 the maximum peak-to-peak asymmetry, taken from the parameter c_0 of the template fit, is reported as a function of the emission angle for the three films presented up to here (5 ML, 2 ML, and 1.5 ML) and a 3 ML Co film (measured also at 100 K). The angular distributions of the total intensity of the Co-$2p_{3/2}$ peak, obtained by summing the $2p$ intensity spectra for the two opposite magnetizations of the same measurements, are shown in Fig. 4.12. In the angular dependences of the intensity there is a clear peak located at $\alpha = 0°$ for the 5 ML and 3 ML films, while for the 1.5 ML and 2 ML films only weak indications of a maximum along the sample normal are present. As discussed in the previous subsection, forward scattering will lead to clear peaks of the photoemission intensity along low index axes of the crystal. When the film thickness is reduced to just 1 ML, along the surface normal (for any crystal structure) there would be no more forward scattering,

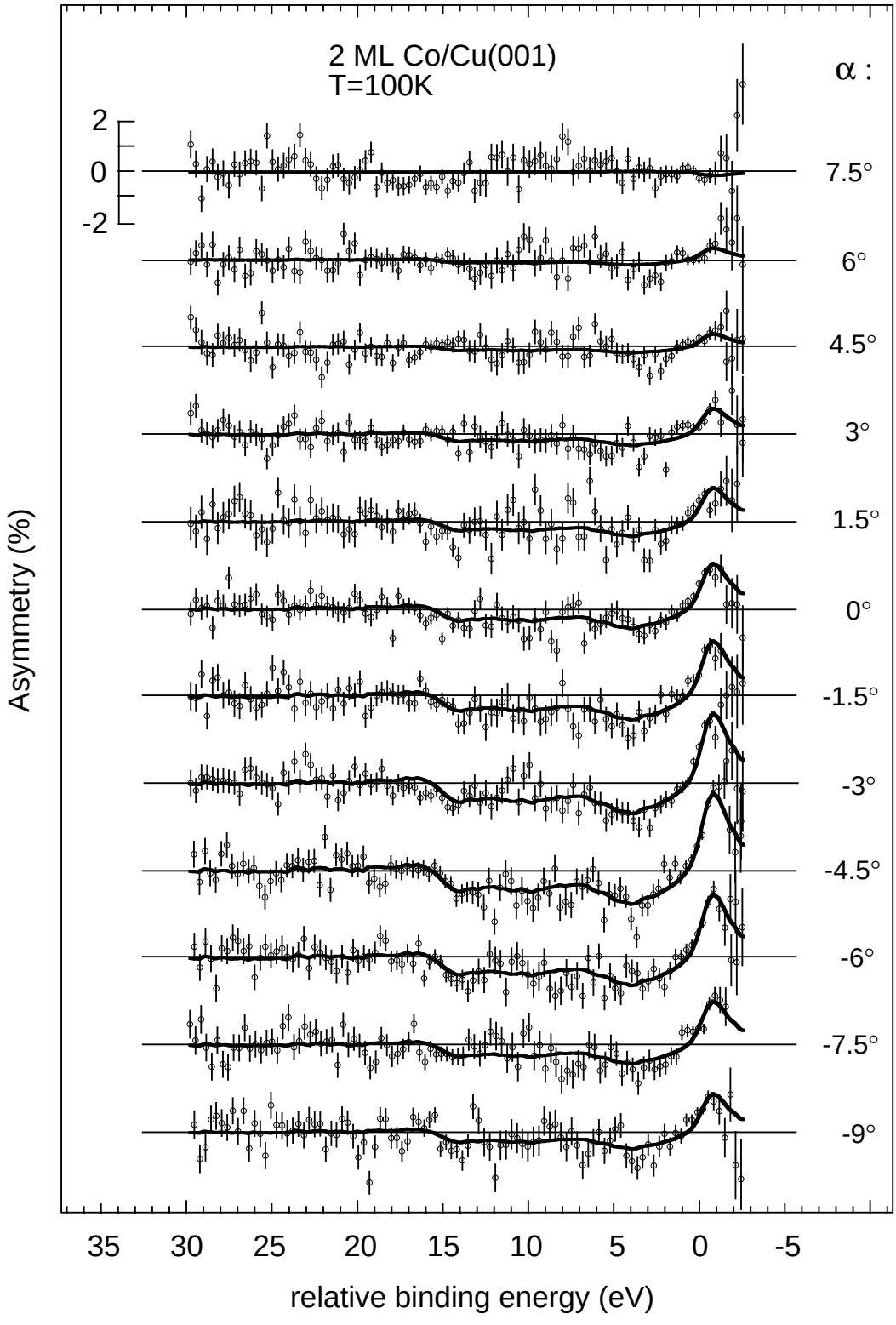

Figure 4.9: As Fig. 4.6, but for a 2 ML Co/Cu(001) film.

because no atoms are available to focus the photoelectrons coming from the film atoms. Therefore no angular variation of the photoemission intensity around the normal

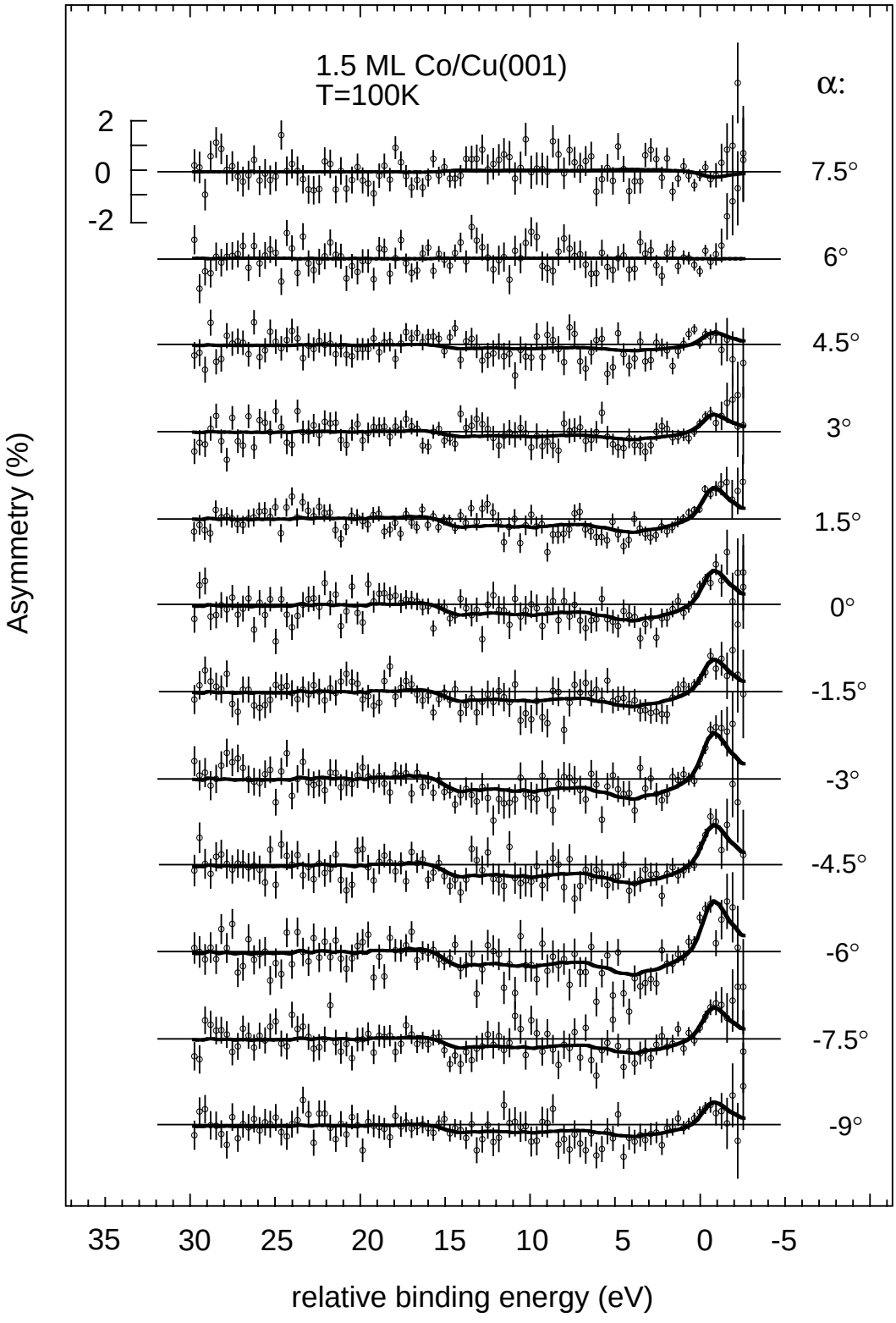

Figure 4.10: As Fig. 4.6, but for a 1.5 ML Co/Cu(001) film.

should be observed, either. Along the <001> axis of an fcc structure, there are no atoms available to focus the photoemission intensity along the surface normal already

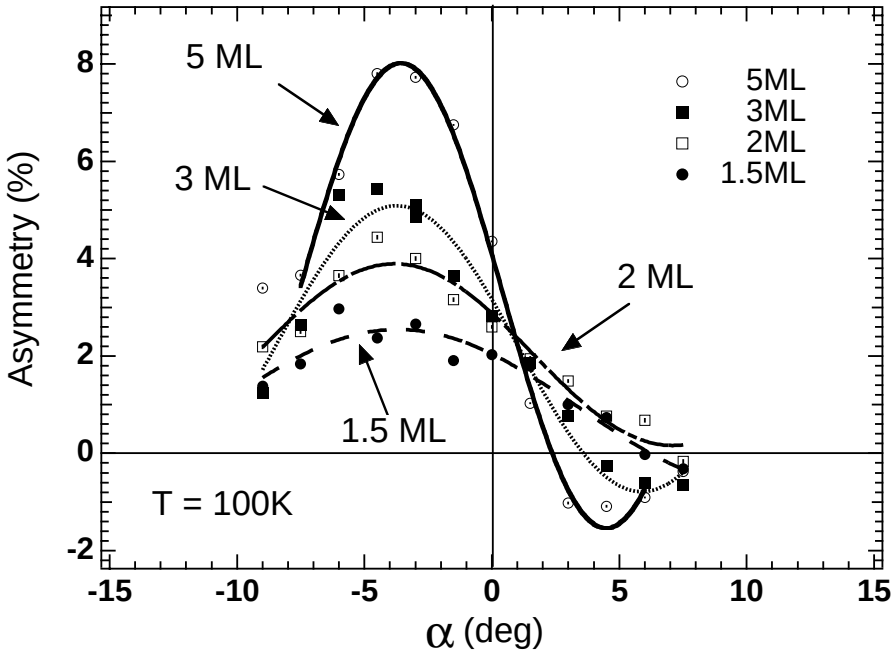

Figure 4.11: The angular distribution of the maximum peak-to-peak asymmetry, taken from the parameter c_0 of the template fit, for 1.5 ML Co/Cu(001) (filled circles), 2 ML Co/Cu(001) (open squares), 3 ML Co/Cu(001) (filled squares), and 5 ML Co/Cu(001) films (open circles) at 100 K. The error-bars are included but too small to be recognized. The lines are guides to the eye.

at a thickness of less than 2 ML. This is consistent with the angular dependence of the photoemission intensity in Fig. 4.12, which shows for 1.5 ML and 2 ML only weak indications of a maximum along the sample normal.

In Fig. 4.11 the angular distribution of the dichroism for 5 ML Co film presents a strong antisymmetric modulation around $\alpha = 0°$, which was already shown in the subsection 4.2.2. For 3 ML, the amplitude of the modulation is reduced, and for the 2 ML and 1.5 ML thick films, even if less visible, there is still a similar modulation present. The amplitude of the modulation of the asymmetry around the surface normal is thus decreasing with decreasing film thickness. Also this modulation becomes broader from 5 ML to 1.5 ML. The results, therefore, show that diffraction effects in magnetic dichroism are reduced at thinner films.

In order to show how the sample temperature influences MLDAD, measurements have been performed on a 3 ML, a 5 ML, and a 10 ML Co/Cu(001) film at a sample temperature of 300 K. The data were analyzed as before, using the same template fit. The angular distributions of the maximum peak-to-peak asymmetry, taken from the parameter c_0 of the template fit, for 3 ML, 5 ML and 10 ML Co/Cu(001) at 300 K are depicted in Fig. 4.13. (Because the Curie temperature for 1.5 ML is less than 300 K, and for 2 ML is about 300 K [22], magnetic measurements on these two films at 300

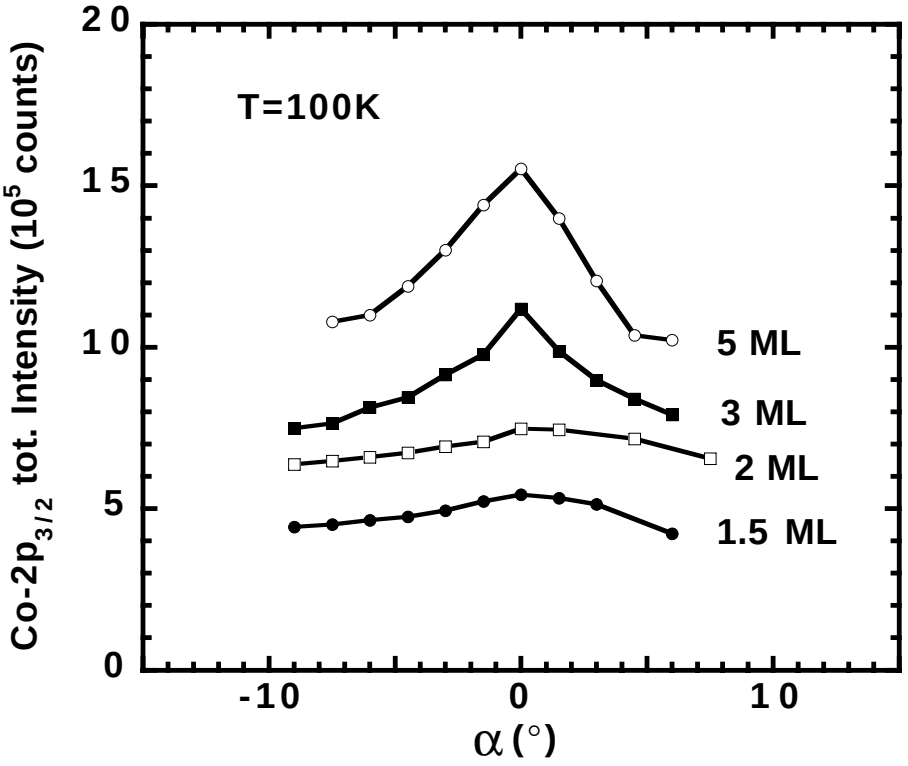

Figure 4.12: The angular dependence on the emission angle α of the Co-$2p_{3/2}$ peak height ($I^+ + I^-$) of 1.5 ML Co/Cu(001) (filled circles), 2 ML Co/Cu(001) (open squares), 3 ML Co/Cu(001) (filled squares), and 5 ML Co/Cu(001) films (open circles) at 100 K. For clarity the angular distribution of the 3 ML and 2 ML films has been shifted up along the vertical axis by $2.5 \cdot 10^5$ and $2 \cdot 10^5$ counts, respectively. All data points have been acquired under identical experimental conditions.

K are impossible.) All three films measured at 300 K show strong forward scattering along the surface normal. Going from 3 ML to 5 ML, forward scattering was found to increase slightly, similar to the measurements at 100 K. Between 5 ML and 10 ML thickness, almost no difference for forward scattering along the sample normal was found. However, the variation of the dichroic asymmetry along the sample normal increases strongly when going from 3 ML to 5 ML, and still increases from 5 ML to 10 ML (see Fig. 4.13). By comparing Fig. 4.13 to Fig. 4.11, it becomes clear that the variation of the dichroic asymmetry at the same thickness is strongly reduced at 300 K. This can only be explained by reduced diffraction effects at higher temperature than at lower temperature.

To quantitatively describe the angular behavior of the asymmetry of different films in a narrow angle range around normal emission, the data points of Figs. 4.11 and 4.13 have been fitted in the α range between $-8°$ and $6°$ by $c_0 \sin(c_1\alpha + c_2) + c_3$, where c_0, c_1, c_2 and c_3 are fitting parameters. The strength of the angular variation

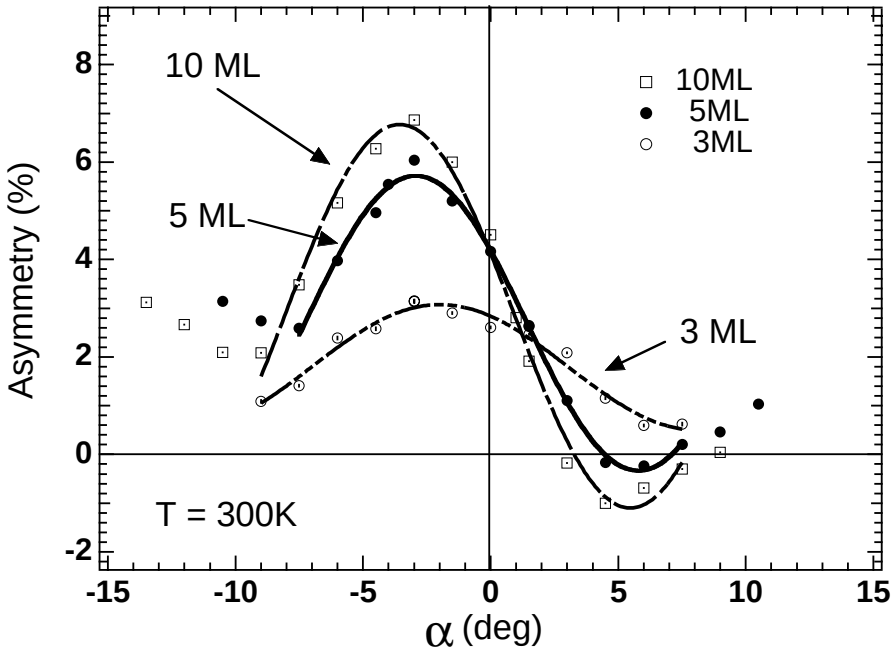

Figure 4.13: The angular distributions of the maximum peak-to-peak asymmetry, taken from the parameter c_0 of the template fit, for 3 ML (open circles) , 5 ML (filled circles), and 10 ML (open squares) Co/Cu(001). The sample temperature is now 300 K. The error-bars are included but too small to be recognized. The lines are guides to the eye.

of the dichroism then can be represented by the amplitude parameter c_0 and the period $360°/c_1$ of the fit. Fig. 4.14 summarizes the result of these fits, showing the amplitudes and periods of all of the films presented in this subsection. It is clear that the amplitude and period are strongly influenced by the thickness and the sample temperature. Generally at the same temperature, the amplitude will increase and the period will decrease as the thickness is increased. From Fig. 4.14, it becomes clear that the increase of the amplitude is very fast from 1.5 to 5 ML, and slow from 5 to 10 ML. At all thicknesses, at 300 K the amplitudes are smaller and the periods are larger than at 100 K. At the thin film limit (1.5 ML), the amplitude is strongly reduced, and the period is strongly increased. The above results show that the thickness and temperature are very important in diffraction effects in MLDAD and will be discussed fully in the next chapter.

4.2.4 MDAD in an extended angular range including several low index axes

It was shown in the previous subsection that there is a strong variation of the dichroism around the <001> axis in thick Co films. It is therefore interesting to study if these variations exist also around other low index axes of the film. To approach

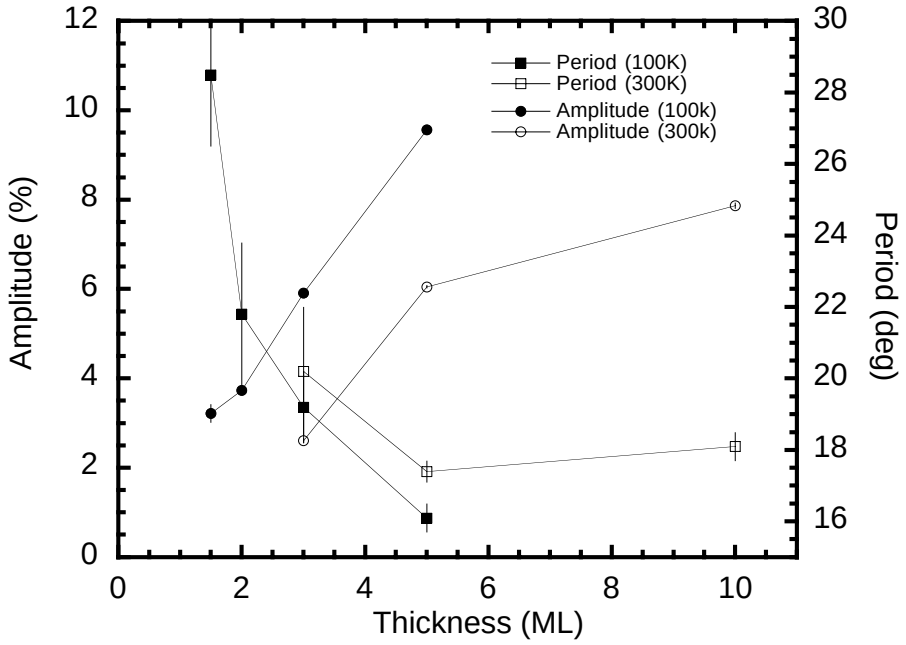

Figure 4.14: The amplitude and period of the fit for the α-angular distribution of the dichroic asymmetry (Figs. 4.11 and 4.13) for all the films studied here as a function of thickness. The filled circles and filled squares are the amplitudes and periods for films respectively measured at 100 K. The open circles and open squares are the amplitudes and periods for films respectively measured at 300 K.

other low index directions like for example the <011> axis in the present geometry, the angular dependence of MLDAD can be measured by rotating the sample around the <100> axis as before, but using a more extended angular range. To approach, for example, the direction <112>, the azimuthal angle of the sample has to be rotated to have the magnetization of the sample along <110>, and to measure the same angular dependence by rotating the sample along the <110> axis in an extended range of the emission angle α. In both cases, a method is needed to measure the angular dependence of MLDAD quickly to obtain spectra at as many α angles as possible. To measure a complete dichroism spectrum around the Co-2p levels takes normally about 20 minutes in a 5 ML Co film. To get the information of the angular dependence of, for example, $\alpha = -16°$ to $\alpha = 60°$ in steps of 2° or 3°, about 30 to 40 spectra have to be taken, which would take more than 10 hours. For thinner films, even more time would be needed. During such a long time, the film will be contaminated even under UHV conditions. To save time in the study of the angular dependence of magnetic dichroism, only the photoemission at the peak of the dichroic asymmetry at $2p_{3/2}$ may be followed as a function of emission angle. Thereby it is assumed that the shape of the asymmetry spectra does not change as a function of the emission angle α, as was demonstrated in the previous subsections. If the baseline for each spectrum is

well calibrated, the rest of the spectra of Co-2p level at each α angle is then less important in the study of diffraction effects in MLDAD. In order to analyze the data, it is also necessary to measure some points at kinetic energies above the $2p_{3/2}$ peak, and some points at kinetic energies below the $2p_{1/2}$ peak. This allows one to remove the background at the higher kinetic energy side of the $2p_{3/2}$ peak and to rescale the spectra at the lower kinetic energy side of $2p_{1/2}$ to fix the baseline in the dichroic asymmetry. Although this procedure does not allow to use the template fit, it is good enough for a quick study of a film with a high enough dichroic signal. In this way for a 5 ML Co film, now only about 8 minutes are necessary to acquire the spectra at $2p_{3/2}$ at one angle with the same count rate as before. This makes the measurements more than twice as fast than before. It is now possible to study the angular dependence of MLDAD in an extended angular range including several low index directions.

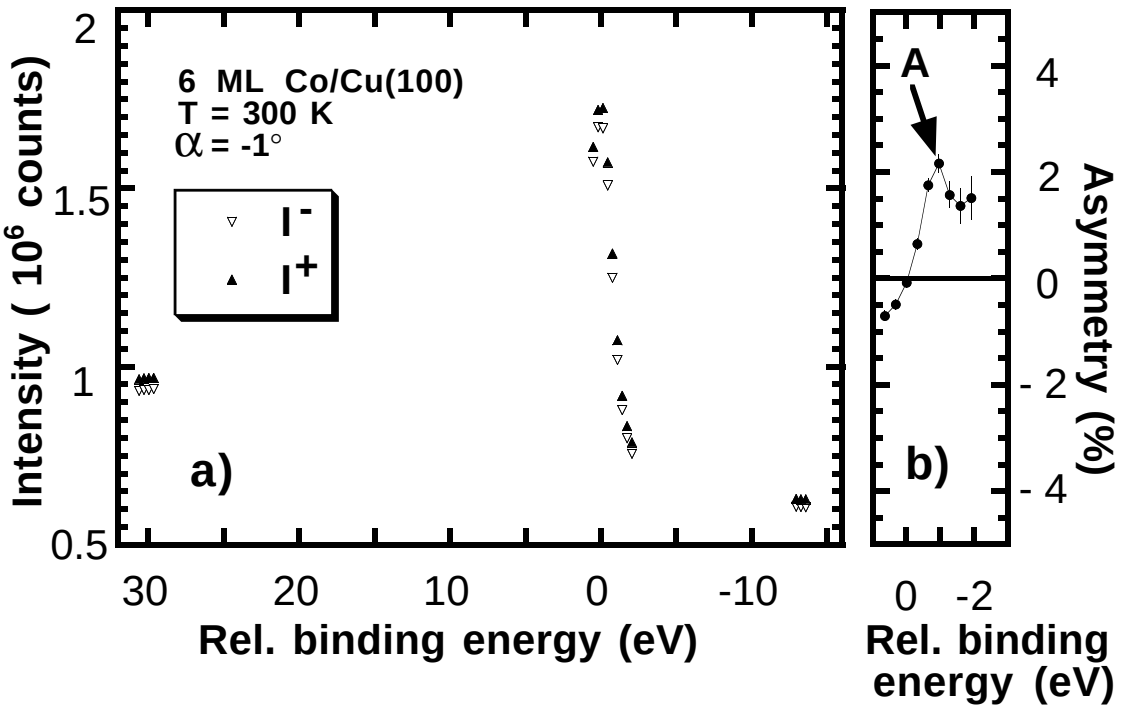

Figure 4.15: a): Co-2p intensity spectra for both magnetizations (I^+ and I^-), measured on 6 ML Co/Cu(001) at $\alpha = -1°$ at a temperature of 300 K. From left to right, the first data points at left hand side are used for rescaling, the middle data are from $2p_{3/2}$ peak, and the data at the right hand side are used for the subtraction of the background. b): Dichroic asymmetry spectrum calculated from the photoemission intensity spectra of a). Feature A indicates the "plus" feature of the Co-$2p_{3/2}$ dichroism, which is the same as in Fig. 4.4b.

Fig. 4.15a shows Co-2p intensity spectra for both magnetizations (I^+ and I^-), which were measured on 6 ML Co/Cu(001) at α=$-1°$ at 300 K. Shown are raw

spectra vs. a relative binding energy scale. In this figure, the data are presented in three parts, otherwise the spectra are just like the spectra in Fig. 4.4a before any analysis process. The data at the left and right hand side are used for rescaling and for subtracting the background, respectively. The $2p_{3/2}$ peak is also clear in this figure. In Fig. 4.15b, the calculated dichroic asymmetry is reported. The analysis process is as mentioned before, and the "plus/minus" feature of the Co-$2p_{3/2}$ shows up clearly in the spectra. The feature A is the same as in Fig. 4.4b, the height of which is used in the following to study the angular dependence of the magnetic dichroism.

As discussed before, when studying the angular dependence of the dichroic signal, the angular dependence of the intensity gives information on the structure of the film. By rotating the sample by a large angle with respect to the light incidence and the analyzer, the intensity change due to the changing geometry must be considered in order to obtain exact information about the intensity distribution due to the structure of the film. Although the photon flux per surface area changes with the light incidence direction, it is not relevant to the present question. Because the film is much thinner than the penetration depth of the x-rays and the sample is always fully illuminated due to its small size, the number of absorbed photons within the film is constant and there is no change of the photoemission intensity due to the change of the light incidence direction.

Another possible reason for a photoemission intensity change due to sample rotation is connected to the variation of the emission angle. For a thick film, the photoemission intensity varies when the emission angle is changed due to the limited free path length of the photoelectrons. At larger emission angles from the surface normal, the path traveled by photoelectrons in the film is longer, so that the photoemission intensity is reduced. In order to quantitatively discuss this effect, the mean free path length λ must be used to describe the attenuation of photoelectrons in the film. As the path traveled by electrons in the film depends on the emission angle α and the distance d of the emitters to the surface, the total photoemission intensity can be calculated to be proportional to $\cos(\alpha)$ for a thick film. Therefore the intensity of the photoemission will be reduced by factor of $\cos(\alpha)$ when the emission angle is not along the normal. This effect is referred to as "reduced effective probing depth" in this thesis and it is less important when the measurement is limited to a narrow angle range around the surface normal as in the previous subsections. However, when the measurements are far away from normal emission, this reduction will be significant and must be considered. In order to separate the effect coming from this effect and the real forward scattering effect, the intensity dependence in the following will be normalized by a factor $1/\cos(\alpha)$.

Fig. 4.16a shows the angular dependence of the intensity of the Co-$2p_{3/2}$ peak

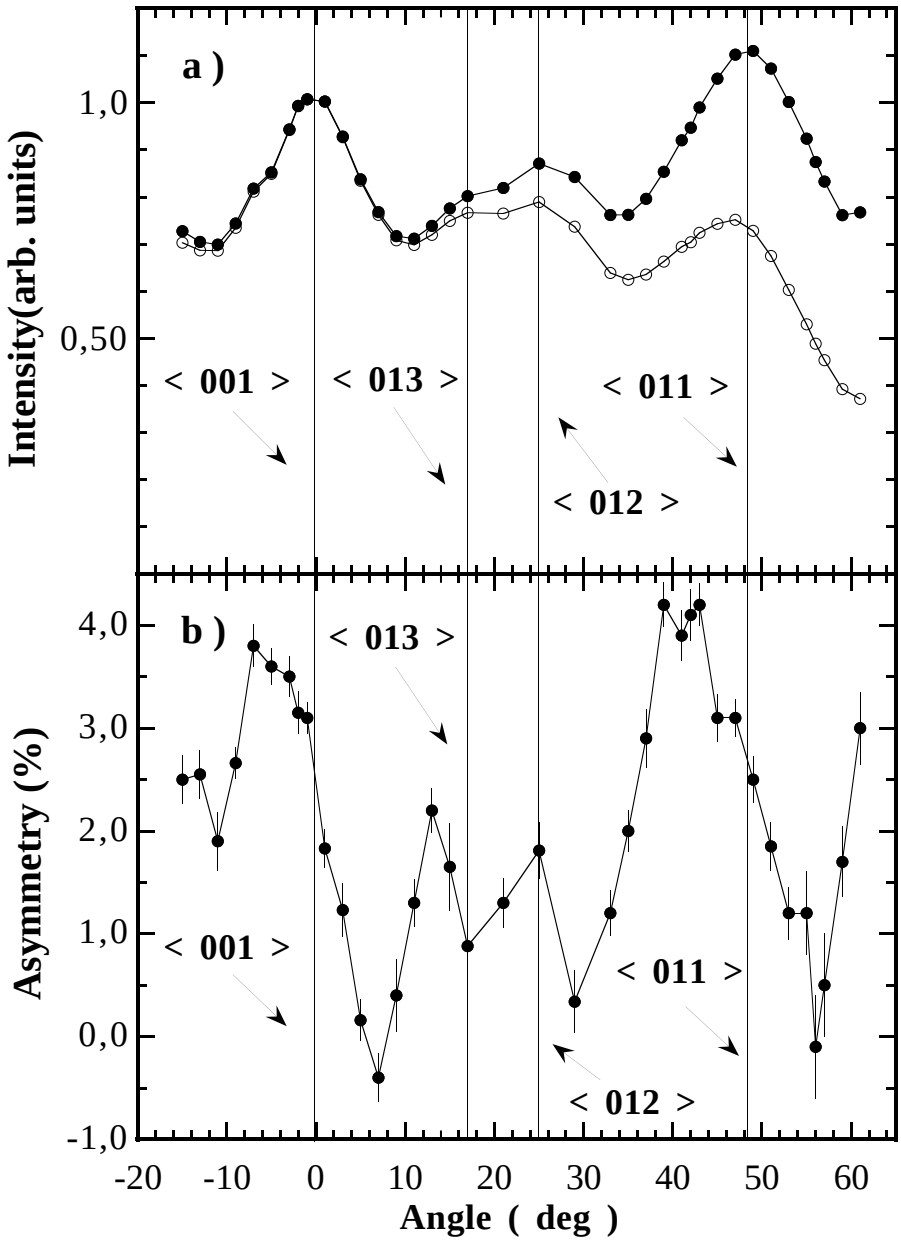

Figure 4.16: a): Angular distribution of the intensity of the Co-$2p_{3/2}$ peak (by adding the I^+ and I^-) (open circles) and after the normalization by $1/\cos(\alpha)$ (filled circles). The data were measured at a 6 ML Co/Cu(001) at 300 K as shown in Fig. 4.15a. Vertical lines indicate the low index directions. b): Angular dependence of the maximum dichroic asymmetry at Co-$2p_{3/2}$ (feature A in Fig. 4.4b and in Fig. 4.15b.) Vertical lines indicate the angles for low index axes.

without and with the normalization by $1/\cos(\alpha)$. The sample was a 6 ML Co/Cu(001) film, which was measured at room temperature. The magnetization is along <100> as before. By rotating the sample around this axis, the photoemission to the analyzer will pass through the <001>, <013>, <012> and <011> axes of the Co fct structure.

In the intensity angular distribution, the forward scattering peaks along these low index axes should be observed. However, as seen in the raw data the photoemission intensity always drops when the emission direction turns away from the normal due to the reduced effective probing depth of the photoelectrons. This effect complicates the angular distribution, especially along the <011> direction. However, the normalized data show pronounced forward scattering peaks along both the <001> and <011> directions. The forward scattering peak around the <011> axis is at 48° from the normal. From the figure, other forward scattering intensity peaks along <013> and <012> are also visible, which are about 19° and 27° away from normal emission, respectively. The angle of 48° (for <011> direction) is about 2° bigger than 45.7° calculated from data of Ref. [25] for an fct structure of 6 ML Co/Cu(001). This discrepancy is, however, still within the experimental angular resolution of 3°. The whole intensity distribution is in sound consistence with Ref. [57] in most details (see Fig. 4.2). Especially after normalization, the intensity peak at <011> is even higher than <001>, which is also in agreement with Ref. [57]. The reason is maybe that the next-nearest-neighbor atom (along the <001> direction) is further away and redirects a smaller fraction of the total emitted electron wave into the forward direction than the nearest-neighbor atom (along the <011> direction).

In Fig. 4.16b, the angular dependence of the maximum dichroic asymmetry at Co-$2p_{3/2}$ (feature A in Fig. 4.15b) is depicted. The strong variation of the signal around the normal is very similar to the case of 5 ML and 10 ML Co films reported before (see Fig. 4.13). At the same time, a similar strong variation around the <011> axis is observed. Around the <013> and <012> axes, the situation is more complicated. However, some small variation around both axes is still visible.

In order to study the influence of the azimuthal angle of the sample, the sample is now rotated around the surface normal at an emission angle $\alpha = 47°$. This angle corresponds to the direction of the <011> axis when the azimuth is along <100>. Fig. 4.17 reports the results for this measurement with the α angle fixed and the azimuthal angle Φ varied. In Fig. 4.17a the angular dependence of the intensity of the Co-$2p_{3/2}$ peak is reported. The first maximum is due to the forward scattering along the <011> axis, when the magnetization direction is along <100>. The second smaller maximum is from forward scattering along the <334> axis, when the magnetization direction is along <110>. The two maxima are separated by 45°, which is the angle between the <100> and <110> azimuths. From Fig. 4.17b, a strong oscillation of the dichroic asymmetry is observed around the <011> direction. The asymmetry variation has a similar amplitude as before when the magnetization was along <100> and the polar angle was varied. A weaker variation of the dichroic asymmetry around the <334> direction is observed.

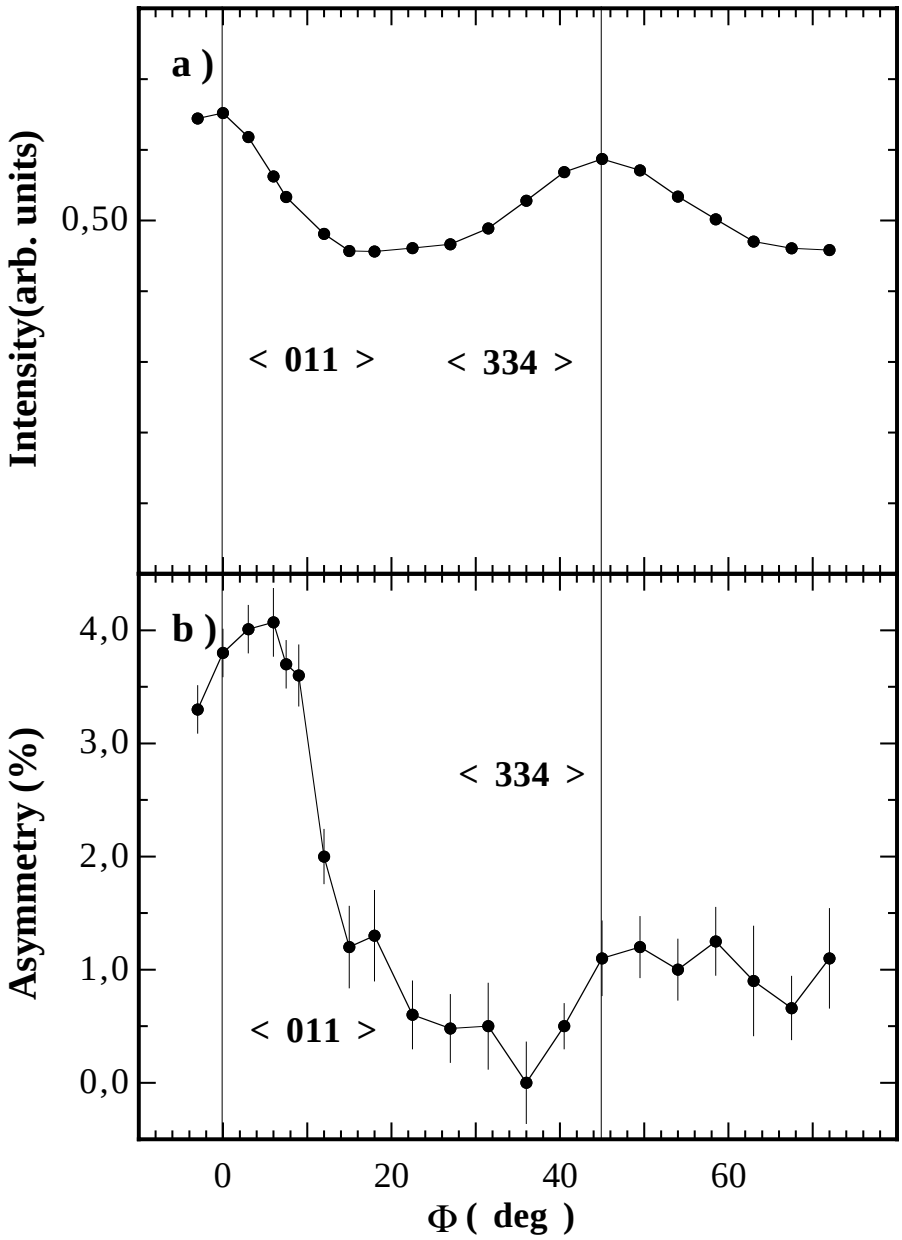

Figure 4.17: a): The Co-$2p_{3/2}$ peak intensity (sum of I^+ and I^-) as a function of the azimuthal angle Φ of the sample, with fixed emission angle α of 47°. The data were measured from a 7 ML Co/Cu(001) film at 300 K using the method described in the text. b): The azimuthal angular dependence of the maximum dichroic asymmetry at Co-$2p_{3/2}$ (feature A in Fig. 4.15b.) Vertical lines indicate the angles for low index axes.

In order to show the angular dependence of the dichroism around other low index axes like <112> and <111>, the azimuth of the sample is now set to <110>, with the magnetization along the same direction. Fig. 4.18a and b display the angular dependence of the intensity of the Co-$2p_{3/2}$ peak and the angular distribution of the

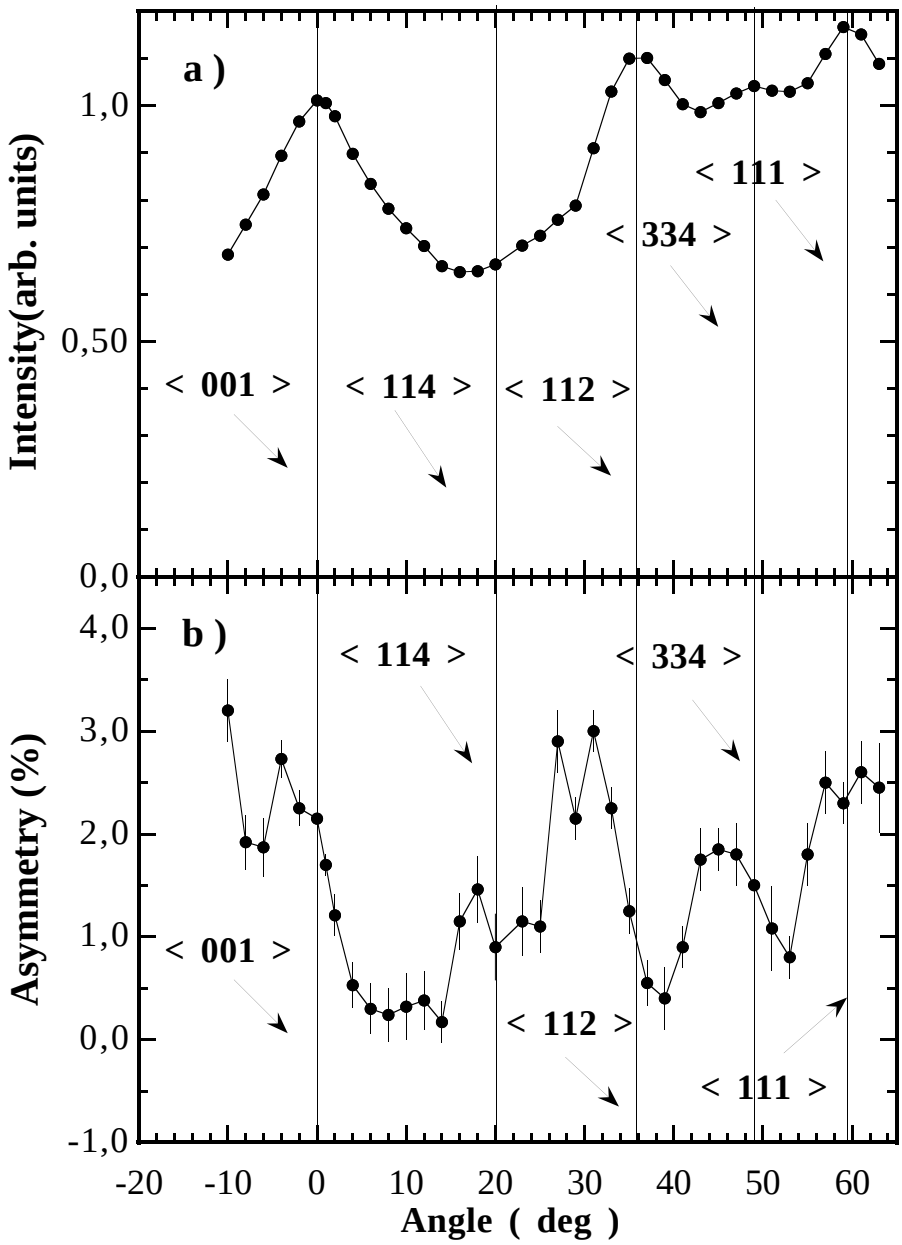

Figure 4.18: a): The angular distribution of the Co-$2p_{3/2}$ peak intensity (sum of I^+ and I^-) after the normalization of $1/\cos(\alpha)$ at azimuth of 45° (along <110>). The data were measured from a 7 ML Co/Cu(001) at 300 K using the method described in the text. b): The corresponding angular dependence of the maximum dichroic asymmetry at Co-$2p_{3/2}$ (feature A in Fig. 4.15b.) Vertical lines indicate the angles for low index axes.

maximum dichroic asymmetry at the Co-$2p_{3/2}$, respectively. As before, the intensity distribution is normalized to the reduced effective probing depth. In Fig. 4.18a, forward scattering peaks along <001>, <112>, <334> and <111> can be clearly recognized. However, the intensity distribution around <114> is too broad to show

a distinct peak. The <112>, <334> and <111> axes are found at emission α angles of 36°, 49°, and 59°, respectively. Form the data in Ref. [25], the theoretical α angles for <112>, <334> and <111> axes can be calculated to be 36°, 46.7°, and 55.4°, respectively. The biggest discrepancy between the experimental value and the calculated is the angle for <111> axis. One possible explanation is the change of the transition matrix element due to the change of the incidence angle of the light.

In Fig. 4.18b, it is shown how the asymmetry varies around each of the low index axes, including <114>. Around the <001> axis the asymmetry varies very similarly to the case when the sample is magnetized along the <100> axis (see Fig. 4.16b), however with a smaller amplitude. Along <112>, where there is strong forward scattering, a strong oscillation of the dichroic asymmetry is also observed. However, the value of the dichroic asymmetry along <112> is much smaller than the one along <001>. Weaker oscillations are also observed around the <334> axis and <111> axis.

What will happen if the sample is rotated to vary α around a direction which is not a low index direction? In order to answer this question, the sample was set to an azimuth in between <100> and <110>, to have the magnetization at an angle of about 27° with the <100> axis and 18° with the <110> axis. The sample measured is 5.5 ML Co/Cu(001), grown under the same conditions as before. Fig. 4.19a reports the angular dependence of the normalized intensity of the Co-$2p_{3/2}$ peak, and Fig. 4.19b the corresponding angular dependence of the maximum dichroic asymmetry at Co-$2p_{3/2}$. Around the normal emission angle there is only little influence of the azimuthal angle, so that there is no big difference in both the intensity and dichroic asymmetry angular distributions around the normal compared to the results presented above. However, the forward scattering maximum along <001> is now found at $\alpha = 1°$, which is still within the experimental angular error. The strong oscillation of the dichroic asymmetry around the normal is reproduced, which does not require the rotation axis to be along any low index axis. The oscillation amplitude is in between the results of Fig. 4.16b and Fig. 4.18b.

At about $\alpha = 20°$ in Fig. 4.19a, there is a very flat intensity maximum. At about $\alpha = 43°$, there is another maximum, which is also flat but much higher compared to the one at $\alpha = 20°$. Both maxima are weaker than the forward scattering peak along the <001> axis. The second maximum are mostly produced by forward scattering along the <110> direction, which is in the neighbourhood. In this thesis, this kind of intensity maximum is called a shoulder of forward scattering. Other shoulders from forward scattering along <334> or <111> are possibly much weaker. The first weak maximum then could be the shoulder of forward scattering along <112> and <012>. Because these two maxima are produced by forward scattering along

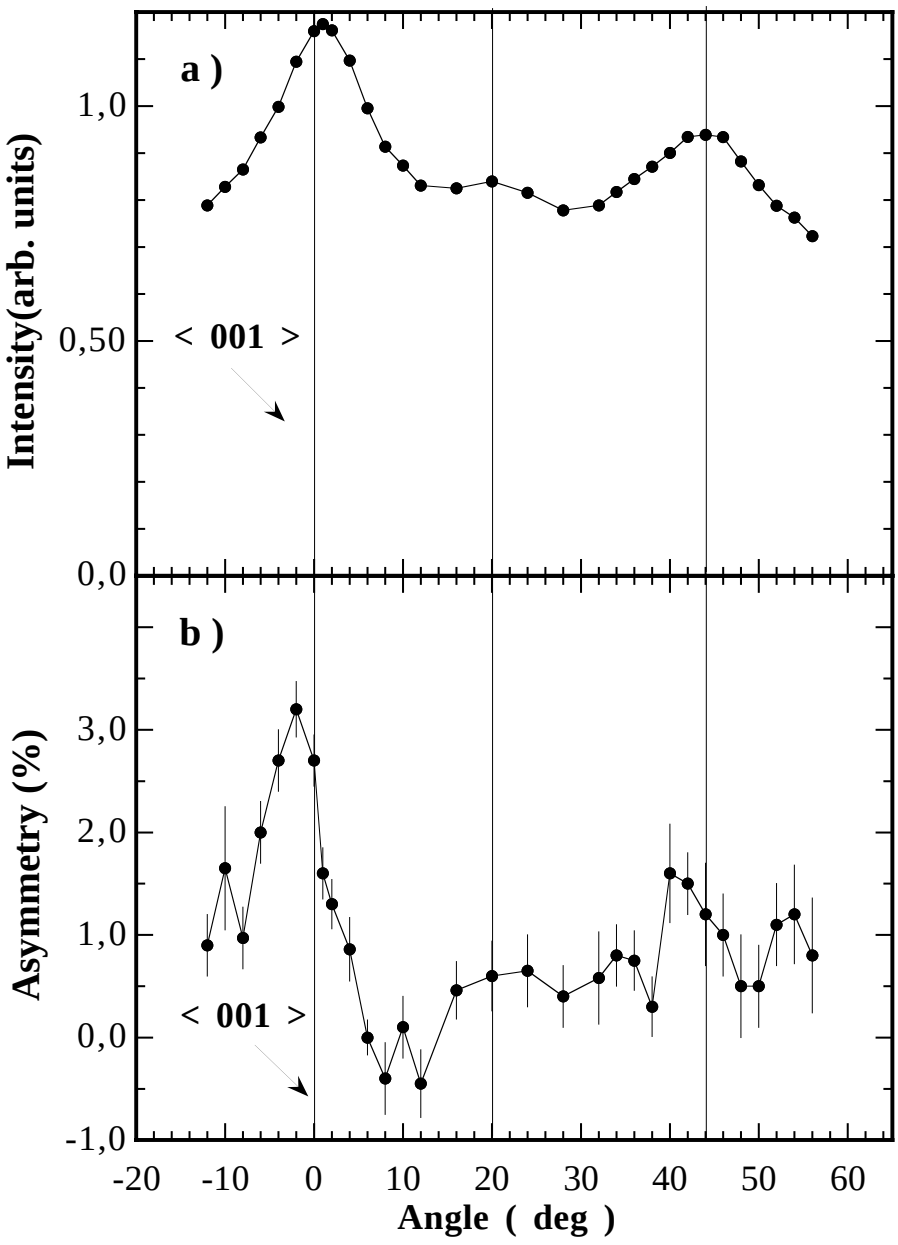

Figure 4.19: a): The angular distribution of the Co-2$p_{3/2}$ peak intensity (sum of I_+ and I_-) after the normalization of $1/\cos(\alpha)$. The data were measured from a 5.5 ML Co/Cu(001) at 300 K. b): The corresponding angular dependence of the maximum dichroic asymmetry at Co-2$p_{3/2}$ (feature A in Fig. 4.15b.) Vertical lines indicate the angles of the intensity maxima, except the one at the sample normal.

low index axes in the neighbourhood, they are much weaker than an actual forward scattering peak. While any one of the two maxima is composed of several peaks at different positions, which are related to different low index axes, the angular intensity distribution is therefore also broader. Around the emission angles of these maxima, the dichroic asymmetry shows also small variations. However, these variations are

very complicated compared to the one around the <110> direction.

4.2.5 MDAD of 5 ML Co/Cu(001) using circular light with lower photon energy

As discussed before in section 4.1, when the kinetic energy of the photoelectrons is low enough, there will be no forward focusing of photoelectrons along the low index directions of the crystal. As forward scattering plays a dominant role in the diffraction effects in MLDAD, it is very interesting to study how the magnetic dichroism varies around these low index directions under these conditions. However, a light source delivering a lower photon energy than the Mg-K_α x-ray tube is necessary for such a study. Around the low index directions, it will also be interesting to see if there are diffraction effects in circular magnetic dichroism in core-level photoemission (MCDAD), *i.e.*, using circularly polarized light. For both purposes, synchrotron radiation is needed, which allows access to circularly polarized light with variable photon energy. As introduced before, beamline ID12b at the ESRF delivers very intense circularly polarized light, which is suitable for photoemission measurements, especially at an energy range around 900 eV.

First the results for LMDAD measured at room temperature using circularly polarized light with a photon energy of 1000 eV will be discussed. The sample is 5 ML Co/Cu(001), which was prepared as mentioned before. In this experiment, the geometry is almost the same as in Fig. 4.3, except that the azimuthal angle of the sample is rotated by 45° from <100>. Therefore the sample was magnetized along the <110> direction, which is vertical to the plane containing **k** and **q**. The measurement procedure was the same as the procedure using unpolarized light in the laboratory. Circularly polarized light can be considered as coherently superimposed *s*- and *p*- linearly polarized light. Of these just the *p* component generates a magnetic dichroism in such a geometry. By reversing the magnetization of the film for a fixed helicity of the circular light (left circularly polarized light in this thesis), there should be a magnetic dichroism qualitatively identical to that observed using unpolarized light. Therefore the magnetic dichroism measured in that geometry is called LMDAD in this thesis.

In Fig. 4.20a intensity spectra at $\alpha = 0°$ for both magnetizations, I^+ and I^-, are shown. The data were analyzed as before in Fig. 4.4a. In Fig. 4.20b, the dichroic asymmetry of the spectra is depicted. The data points (open circles) are analyzed after a template fit as in subsection 4.2.2, and the solid line is the template scaled with scaling parameter c_0 (about 2). The template curve here is the same as before.

With a photon energy of 1000 eV, the Co-$2p_{3/2}$ peak appears at a kinetic energy of about 216 eV, and the Co-$2p_{1/2}$ peak at about 201 eV. The two peaks are thus

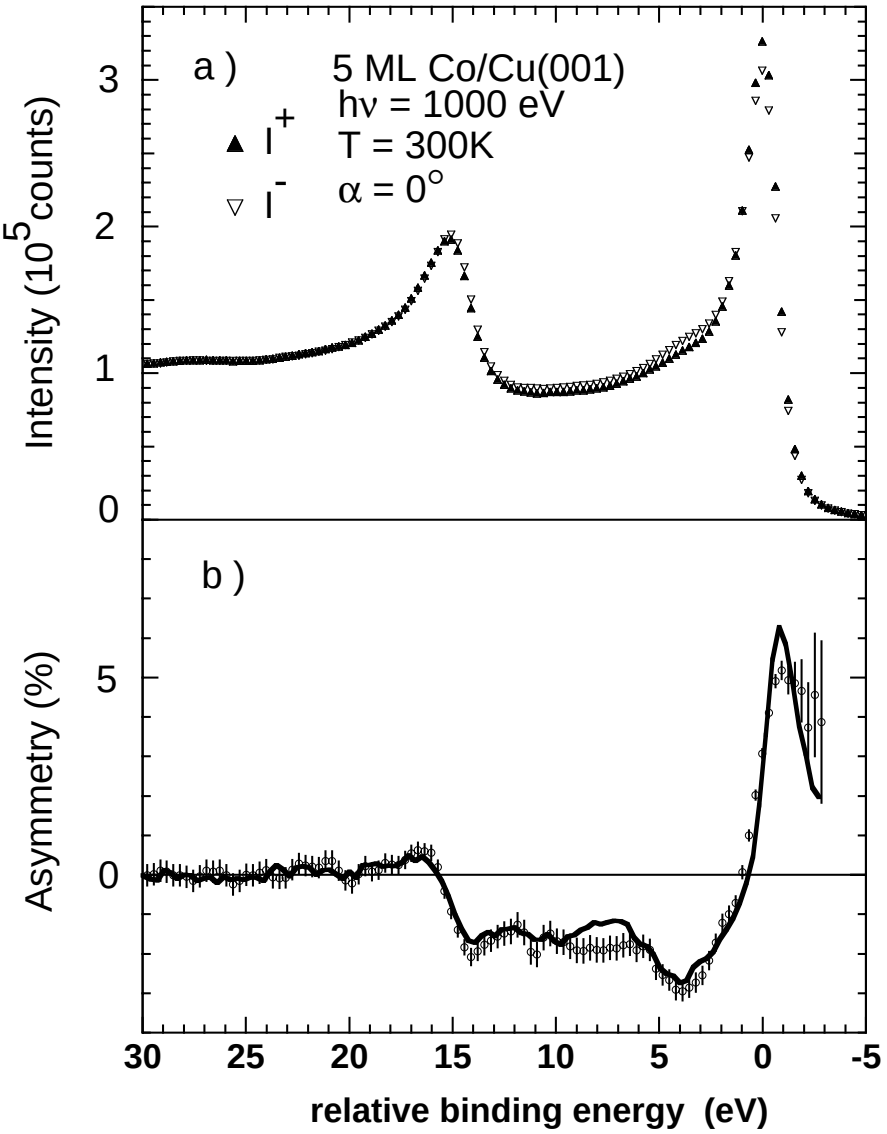

Figure 4.20: a): Co-2p intensity spectra for both magnetizations (I^+ and I^-) measured on a 5 ML Co/Cu(001) at normal emission angle at a temperature of 300 K in the MLDAD geometry, using circularly polarized light of 1000 eV photon energy. b): Dichroic asymmetry spectrum calculated from the photoemission intensity spectra of a). The baseline has been corrected after the template fit (open circles). The solid line is the template curve scaled with a parameter $c_0 = 2.06$.

separated by $\sim$ 15 eV, which is consistent with literature [59]. A broad structure centered at $\sim$ 4 eV is also clearly seen as in the case of unpolarized light, having higher intensity for the magnetization "down".

The asymmetry spectrum in Fig. 4.20a presents clearly the "plus/minus" features of the 2p lines. The feature C of Fig. 4.4a is also clearly seen, which is related to many body effects as discussed before. It is obvious that the template created from the measurements at 1254 eV photon energy fits well the dichroic asymmetry

spectrum at a photon energy of 1000 eV. When the photon energy changes, the transition matrix elements should change. As discussed in section 2.3, in the simple one-electron model a change of the matrix elements just changes the size of Δ_{MDAD}, and the shape of the asymmetry spectrum should be conserved for the same film at different photon energies. This is plausible from the above experimental results, which show a strong similarity of the asymmetry spectrum with the scaled template spectrum at higher photon energy. However, certain deviations are found at relative binding energies below 15 eV, especially in the range from 6 eV to 9 eV. This could be attributed to a different background intensity due to inelastic scattering of the photoelectrons at different kinetic energies. Furthermore, the circularly polarized light from the synchrotron source is monochromatized and does not contain other spurious photons with comparable photon energies. The spurious photons in the x-ray tube will also induce photoemission processes which will increase the background between the $2p_{3/2}$ and $2p_{1/2}$ peaks. This could be another explanation for this slight difference. Generally, both the intensity and asymmetry spectra reported here agree well in shape with the spectra which were reported in Fig. 4.4.

The angular dependence of the maximum peak-to-peak asymmetry, quantified by the parameter c_0 of the template fit, is plotted in panel b) of Fig. 4.21. The angular distribution of the $2p_{3/2}$ peak height is shown in panel a) (open squares). The results are clearly not symmetric with respect to normal emission. This non-symmetric distribution must be connected to the light incidence, contrast to the experiments using the x-ray tube, where the whole sample is evenly illuminated. In the experiments using circularly polarized light, the size of the light spot on the sample is smaller than 1 mm^2, and the sample is of size cm^2. By changing the incident angle of the light, the size of the illuminated area on the sample will thus be changed. Because the samples in this work are ultrathin films with just several ML ($t \approx 10$ Å), the x-ray mean penetration depth will be much larger than the film thickness. The change of the illuminated size on the sample means then a change of the total number of atoms which contribute to the photoemission signal. When the light is incident under some angle, which is in the present experimental geometry $(45^\circ + \alpha)$, the photoemission intensity is scaled by $1/\sin(45^\circ + \alpha)$. Therefore the angular dependence of the photoemission intensity from this experiment must be corrected by a scale factor $\sin(45^\circ + \alpha)$. In Fig. 4.21a, the angular dependence of the $2p_{3/2}$ intensity after such a correction is also shown (filled squares). It is almost independent from the emission angle, and symmetric around the normal direction. There is a very small maximum at normal emission. This indicates that forward scattering is not prominent here. This is consistent with the energy dependence of the angular distribution of the photoemission intensity in section 4.1. The Co-$2p_{3/2}$ photoelectrons here have a kinetic energy of 216 eV. At

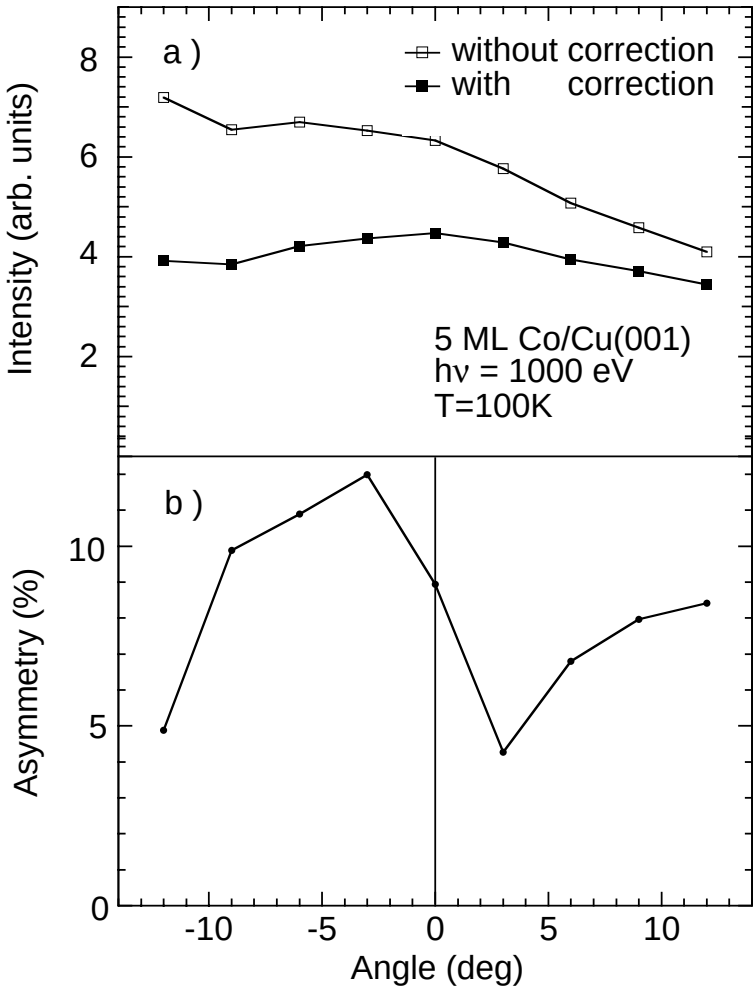

Figure 4.21: a): Dependence on the emission angle α of the Co-$2p_{3/2}$ peak height $(I^+ + I^-)$, measured on a 5 ML Co/Cu(001) at a sample temperature of 300 K (open squares). Filled squares show the data after correction of the illuminating effect of the incidence light. b): The α-angular distribution of the maximum peak-to-peak asymmetry of the magnetic dichroism, obtained from fitting to a template curve.

this energy, forward scattering is very weak [57]. The probability for diffraction into larger angles will increase quickly from higher to lower kinetic energy. This can make the angular dependence of the intensity complicated, especially along <001>, which has already been discussed in section 4.1.

From Fig. 4.21b, a variation of the dichroic asymmetry around the sample normal is still present. The variation here is not as strong as with unpolarized light at higher photon energy and the same thickness (cf. Fig. 4.8). However, the variation of the dichroic signal is still antisymmetric around normal emission, which can be seen from Fig 4.21b. The above results immediately show, that diffraction effects in magnetic dichroism still exist without prominent forward scattering.

Until now all the results were obtained in the geometry for LMDAD measurements.

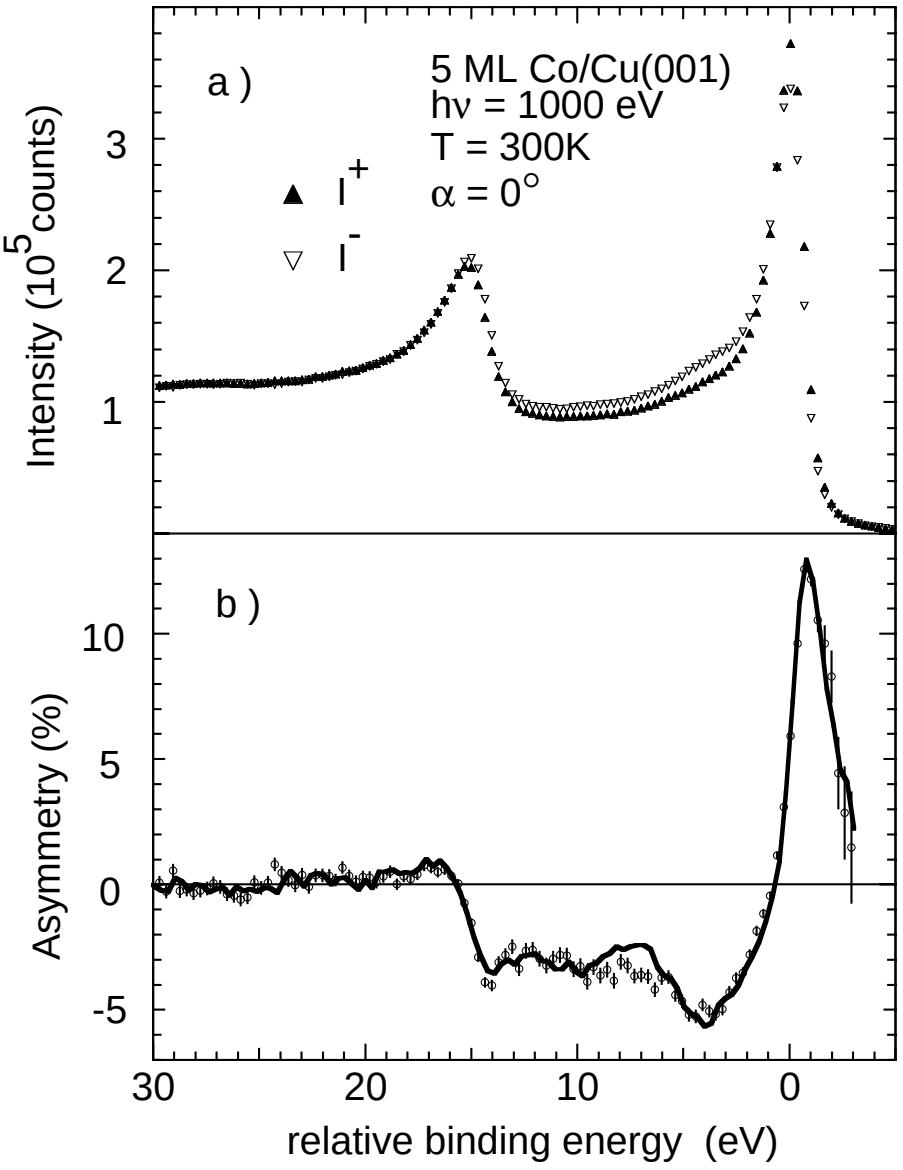

Figure 4.22: a): Co-2p intensity spectra for both magnetizations (I^+ and I^-), measured on a 5 ML Co/Cu(001) film at normal emission and a temperature of 300 K in the MCDAD geometry. b): Dichroic asymmetry spectrum calculated from the photoemission intensity spectra of a). The data points have been corrected after the template fit (open circles). The solid line is the scaled template curve.

In the following the results from the MCDAD measurement are presented. As Co films on Cu(001) always have an in-plane magnetization, the experiment for MCDAD will be performed in a setup similar to the one shown in Fig. 4.3, but with the magnetization in the plane containing $\mathbf{q}$ and $\mathbf{k}$. In this way, the circularly polarized light will be in the same plane as the magnetization, and there will be the same circular magnetic dichroism observed by either reversing the magnetization or the helicity of the light. The measured sample was a 5 ML Co/Cu film, which is exactly

the same one measured in LMDAD geometry using circularly polarized light. The rotation axis for the sample is again along <110>, which means the magnetization is along <$\bar{1}$10>. The sample was magnetized using the pulse coil 1 (see Fig. 3.1 and Fig. 3.2), and the full magnetization was checked by MOKE. The dichroism was then measured as a function of α, as before.

In Fig. 4.22a, intensity spectra at $\alpha = 0°$ in this geometry for both magnetizations I^+ and I^- are reported. The data have been analyzed in analogy to the results in Fig. 4.4a. Fig. 4.22b depicts the dichroic asymmetry spectrum of the spectra of Fig. 4.22a. The data points (open circles) are analyzed by a fit to a template asymmetry curve like in subsection 4.2.2. The solid line shows the scaled template spectrum. The template curve is the same as before.

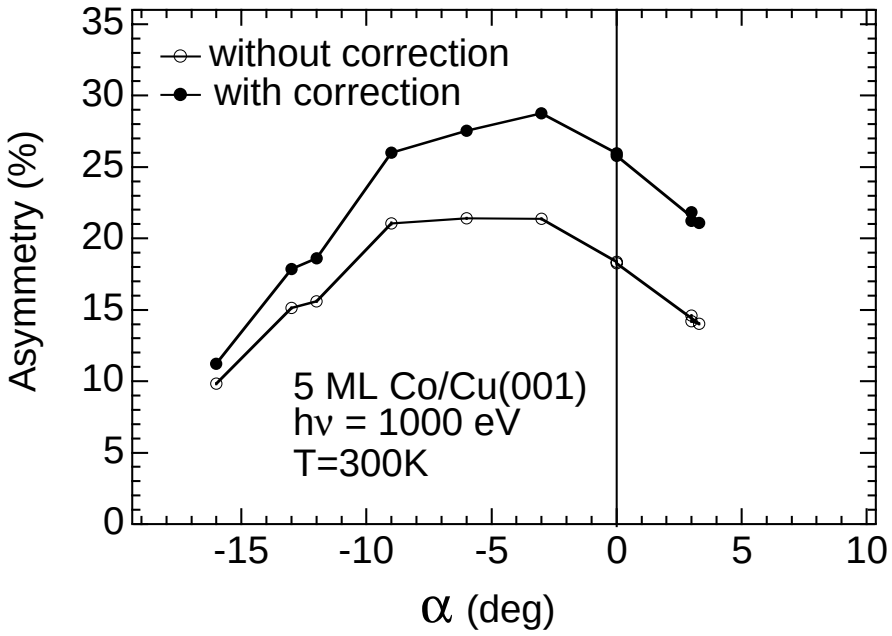

Figure 4.23: The angular distribution of the maximum peak-to-peak asymmetry without correction for the projection of the incoming light onto the magnetization direction (open circles) and with correction (filled circles).

The intensity spectra for both magnetizations are very similar to the ones in Fig. 4.20a. The asymmetry spectrum is also very similar to Fig. 4.20b, but with a much larger value (the maximum peak-to-peak asymmetry at $2p_{3/2}$ is more than 18%). It has the same "plus/minus" feature at $2p_{3/2}$ and a "minus/plus" feature at $2p_{1/2}$ as the linear dichroism spectrum. This is consistent with the one electron theory prediction as mentioned before in section 2.3. More interesting is that the many body feature at about 4 eV is also the same as the one in Fig. 4.20b, this is consistent with Refs. [48]. It is noticeable that the same template as used before fits also very well

here, except for relative binding energies between 6 and 9 eV. This slight discrepancy between the scaled template and the asymmetry spectrum can be explained due to a different background intensity as before for Fig. 4.20b.

In this geometry, the angle between light incidence and magnetization direction is changed by varying α. This will influence the angular dependence of the dichroic asymmetry, since the circular magnetic dichroism depends on this angle. For a free atom, equation (6) of Ref. [21] gives the angular dependence of the magnetic dichroism for that geometry:

$$I^{MCDAD} \propto \cos(\theta) \tag{4.2}$$

where θ is the angle between the magnetization and the incident light, which in our geometry is $\theta = 45° + \alpha$. In order to get rid of this effect in MCDAD, the angular dependence from the experiment should be corrected by a factor of $1/\cos(45° + \alpha)$. Fig. 4.23 gives the angular distribution of the scaling parameter c_0 in percent maximum peak-to-peak asymmetry before and after the correction by $1/\cos(45° + \alpha)$. After the correction, the dichroic asymmetry varies strongly as a function of α. This variation then must be explained by diffraction effects in MCDAD.

4.3 Fe/Co/Cu(001)

4.3.1 Review of Fe/Co/Cu(001)

Ultrathin epitaxial magnetic films permit one to extract information about magnetism on surfaces and interfaces. These films often grow in a metastable structure which cannot exist in the bulk state. This is the reason for the current strong interest in the study of these films. A good example is the Fe/Cu(001) system. Theoretical calculations suggest that for fcc iron a non-magnetic phase, a high-spin or a low spin phase, or an antiferromagnetic phase could be the stable state, depending on the lattice spacing [68-71] Ultrathin Fe films grown on Cu(001) indeed exhibit a variety of different magnetic properties and crystalline structures depending on growth technique, film thickness and temperature [72]. It is well-known that Fe grown on Cu(001) by thermal deposition epitaxy at room temperature presents various magnetic phases with increasing thickness [30, 73, 74] : (1) Fe films less than 4 ML have a ferromagnetic fct structure, with an easy axis of magnetization perpendicular to the surface. (2) Films between about 4 and 11 ML have an antiferromagnetic fcc structure with a ferromagnetic top layer. The easy axis of the magnetization is perpendicular to the surface, and the Néel temperature is below room temperature. (3) Films of more than about 11 ML Fe have an in-plane ferromagnetic bcc structure.

A challenge is whether the metastable fct and fcc structures of iron can be observed on other substrates, and whether the magnetic properties would be the same.

As is known, Co films grown on fcc Cu(001) have a fct structure which adopts the the lateral structure of the the underlying Cu(001) surface [25]. Fe films grown on Co/Cu(001) should therefore have a strong similarity to Fe/Cu(001) films due to the lateral lattice match between the fcc Co film and Cu(001). Of course in this case Co is magnetic, and it is very interesting to study the influence of the magnetic substrate on the Fe films. Recent experiments showed that at room temperature Fe grows on fcc Co(001) in a similar way as on the Cu(001) [75-78]. In the same thickness range of Fe the Fe/Co(001) film is also structurally similar to the Fe/Cu(001) system. Fe films on Co(001) also presents the three distinct magnetic phases known from Fe/Cu(001) [75-77]. The easy magnetization axis of Fe/Co(001) films is rotated to in-plane for all thicknesses due to exchange coupling to Co [75-78]. In phase 2 (thickness between 5 and 11 monolayers), a strongly reduced integral magnetic signal has been found compared to that of thinner or thicker films using magneto-optical Kerr effect (MOKE) and magnetic circular dichroism in x-ray absorption (XMCD) [75-77]. An interesting question arises concerning the position of the remaining ferromagnetic response of Fe in phase 2. From the structural similarity to the Fe/Cu(001) system it would be plausible if it also came from a ferromagnetic Fe layer at the surface. Recent spin- and angle-resolved photoemission experiments of Fe films grown on 15 ML Co/Cu(001) film show indeed that there is a magnetic surface in phase 2 [79]. It was also suggested that the live magnetic layers in the Fe/Co system are located at the Fe/Co interface due to the Fe-Co interaction at the interface [77]. It has indeed been concluded from oxygen adsorption experiments [75, 76] and XMCD [75] that the observed remaining Fe ferromagnetic response should be due to the deeper layers around the Fe/Co interface. However these techniques, namely XMCD and MOKE, are not especially surface sensitive, and it is difficult to distinguish between effects connected directly to the surface of the film or to the Fe/Co interface. For example in the optical wavelength region, the light has a mean free path length inside the sample of more than a few hundred ångstroms. The Kerr signal is not selective for a particular elemental species, therefore a MOKE experiment will average over all contributions from a few hundred ångstroms inside the sample. It cannot deliver magnetic information about ultrathin films grown on magnetically active substrates. For XMCD in soft x-ray absorption the detected signal comes from more than 20 ångstroms when measured as electron yield. To study ultrathin films of just 1-10 monolayers, although this technique is element-specific, it is still relatively difficult to distinguish whether the Fe magnetic response comes from Fe on the surface, from Fe on the interface, or from Fe throughout the film. From the theoretical point of view, it is also difficult to understand that the surface layer of Fe/Co/Cu(001) has an expanded fct structure as the Fe/Cu(001), but is not ferromagnetic, if it is the lattice parameter which determines the phase of

Fe.

As shown for Co films, there are diffraction effects in MDAD, which could give magnetic and structural information of the ultrathin magnetic films. In the Fe/Co/Cu(001) film, the magnetic properties are non-uniform over the thickness, it is therefore very interesting to see if the study of the angular dependence of the MDAD permits one to obtain information about the distribution of magnetic properties within a single film of the same element.

4.3.2 Different angular dependencies of 3 ML and 8 ML Fe/Co/Cu(001) in MDAD using unpolarized light

The experimental setup for the MDAD measurements on Fe/Co films using unpolarized light is exactly the same used before for the Co/Cu(001) measurements (cf. Fig 4.3). The light source is also the same Mg-K_α x-ray tube. Co and Fe films were grown on a Cu(001) substrate at room temperature by electron bombardment of cobalt and iron wires of high purity. The potoemission measurements were performed as described before for the experiments for Co/Cu(001), but the energy range is changed according to the Fe binding energy ($\approx 450-550$ eV electron kinetic energy, the binding energy of Fe-$2p_{3/2}$ and Fe-$2p_{1/2}$ are 707 and 720 eV, respectively). Photoemission spectra of 1 and 3 ML Fe/5 ML Co were recorded at room temperature, and spectra of 8 ML Fe/5 ML Co both at room temperature and 100 K. No significant deviation of the spectra of 8 ML Fe/Co films for both temperatures was found; here the latter are presented because of better statistics. The dichroism is again quantified in terms of the intensity asymmetry.

On these films also MOKE experiments have been performed. Hysteresis loops measured in the longitudinal geometry exhibited a rectangular shape, and showed a reduction of the Kerr signal of about 15% when going from 3 ML to 8 ML Fe on 5 ML Co/Cu(001), which is consistent with results of other groups [76, 77].

Fig. 4.24a displays photoemission spectra of the Fe $2p$ level for 3 ML Fe on Co/Cu(001) at $\alpha = 0°$, obtained by summing the intensity for opposite magnetization directions I^+ and I^- (topmost curve). Depicted are the raw data with just a constant background subtracted at the low binding energy side of the Fe-$2p_{3/2}$ line and rescaled. The corresponding dichroic asymmetry is shown below. Its shape is in good agreement with asymmetries presented in the literatures [3, 6, 14, 15]. A prominent "plus/minus" feature at the $2p_{3/2}$ level is observed (labeled A and B), while at the $2p_{1/2}$ level a weaker "minus/plus" feature appears. The absolute value of the asymmetry of the latter in the present measurement is somewhat lower compared to, for example, Fig.1 of Ref. [14], which was measured on bcc Fe with Al-K_α radiation. This may be related to experimental uncertainties in the determination of the asymmetry baseline,

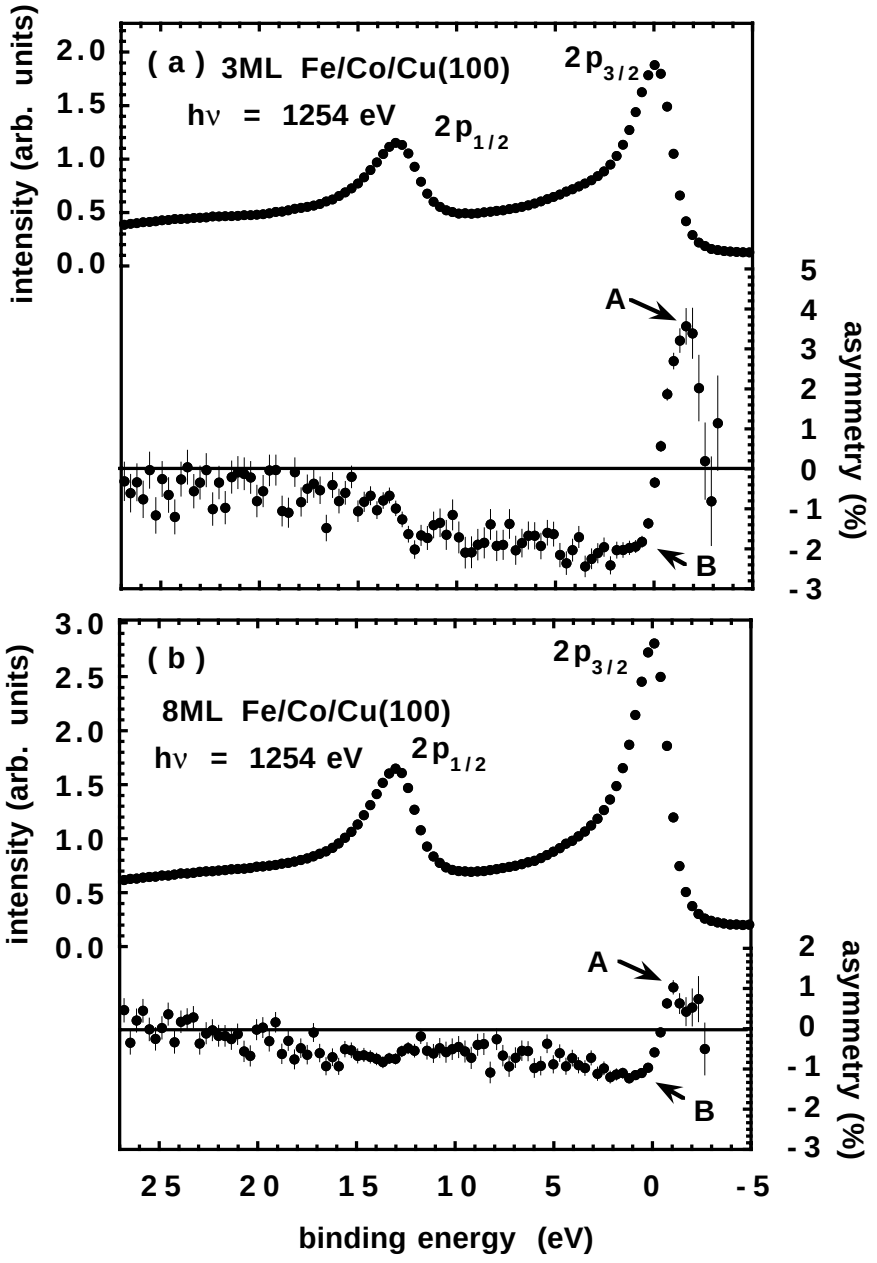

Figure 4.24: a): Fe-2p intensity spectra ($I^+ + I^-$) and dichroic asymmetry spectrum, measured on a 3 ML Fe/Co/Cu(001) at normal emission and a temperature of 300 K. Features A and B indicate the "plus" and "minus" features of the Fe-2$p_{3/2}$ dichroism, respectively. b): As a) but measured on a 8 ML Fe/Co/Cu(001) at 200 K.

which is very sensitive to, e.g., small long-term variations of the x-ray intensity. This uncertainty could be corrected by template fit, as was shown for Co/Cu(001) films. However, only the angular dependence of the dichroism is of interest in the present study. For a simple quantitative analysis of the asymmetry therefore the peak-to-peak asymmetry at the $2p_{3/2}$ level was used (the difference between the asymmetries at A

and B), which is largely independent of baseline uncertainties.

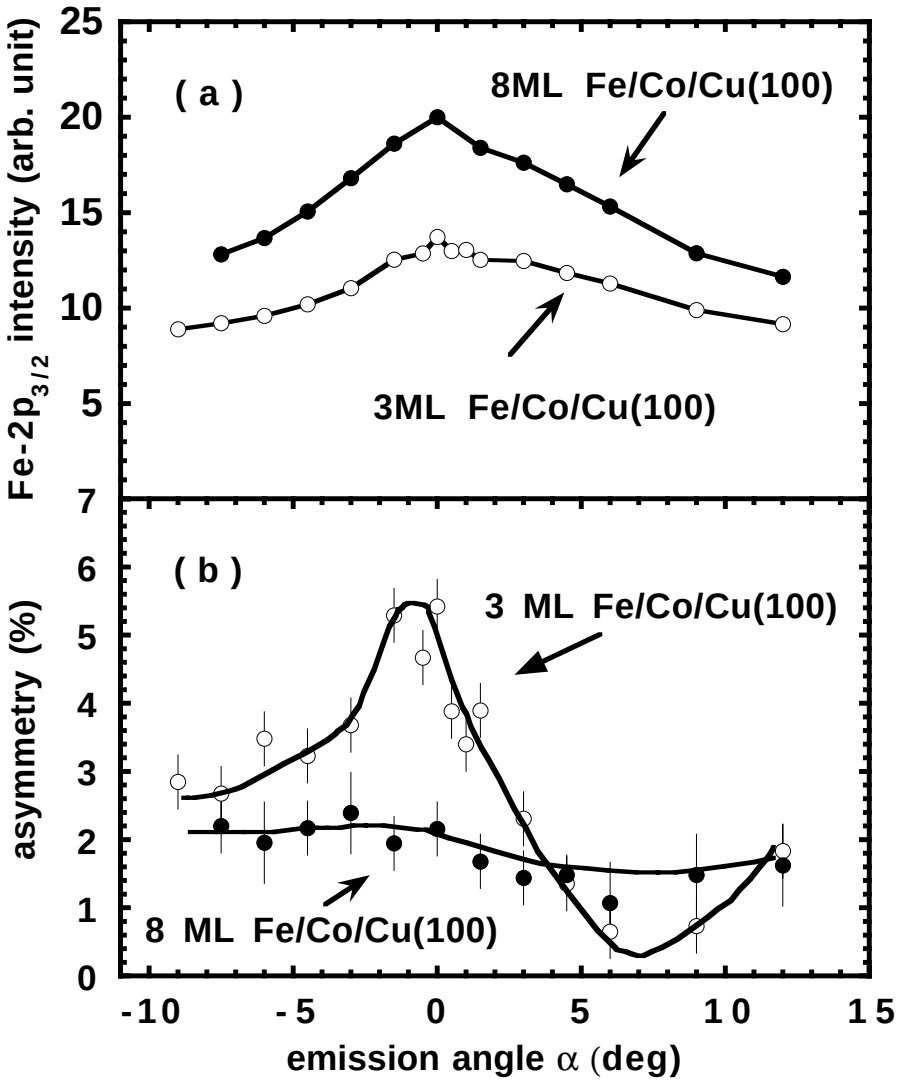

Figure 4.25: a): Intensity of the Fe-2p$_{3/2}$ photoemission peak as a function of the emission angle α for 3 ML Fe (open circles), and 8 ML Fe (filled circles) on 5 ML Co/Cu(001). b): Fe-2p$_{3/2}$ peak-to-peak asymmetry between points A and B (see Fig. 4.24) as a function of the emission angle α for 3 ML Fe (open cirlces), and 8 ML Fe (filled circles) on 5 ML Co/Cu film. The lines in panel (b) are guides to the eye.

Results of the 8 ML Fe/Co film are qualitatively very similar to those of the 3 ML film, but show a higher intensity and a smaller dichroism. This is seen from Fig. 4.24b, where the Fe $2p$ photoemission intensity and asymmetry of 8 ML Fe/5 ML Co/Cu(001) are shown on the same scales as for 3 ML at the same emission angle $\alpha = 0°$. The measured increase of the $2p_{3/2}$ intensity between 3 and 8 ML of Fe by a factor of 1.55$\pm$0.05 corresponds to a mean free path of the 500 eV photoelectrons in Fe of 3.5$\pm$0.4 ML ($\approx$ 6–7 Å), in good agreement with previously published values [23, 67].

By contrast, the asymmetry should stay the same if nothing but the thickness was changed. The decrease of the asymmetry proves that the decrease of the MOKE signal (which integrates over the whole layer stack) is due to a loss of net magnetization in the Fe film at higher thickness. The comparison of the sign of Fe $2p$ with the Co $2p$ dichroic asymmetry (not shown here) shows that the net Fe magnetization is aligned parallel to the magnetization of the Co underlayers. This rules out the possibility that an antiferromagnetic coupling of the Fe film as a whole to the Co layer causes the reduction of the Kerr signal, and confirms that a significant portion of the Fe film is not ferromagnetic.

The electron emission angle α with respect to the surface normal is now varied, and the behavior of both the photoemission intensity and asymmetry as a function of α is measured. In Fig. 4.25 this dependence of the Fe-$2p_{3/2}$ intensity (a) and peak-to-peak asymmetry (b) on the emission angle α is shown. Filled and open circles refer to 3 and 8 ML Fe on Co/Cu(001), respectively. Both films exhibit an intensity maximum at normal emission ($\alpha = 0°$), indicative of <001> forward scattering in epitaxially ordered films. From inspection of the angular behavior of the corresponding asymmetries (Fig. 4.25b), the following important observation becomes obvious: Whereas the 3 ML film displays a strong angular variation of the dichroism, it is essentially constant in the case of 8 ML Fe, even if a very weak modulation may still be present. This different angular dependence of the dichroism must be directly related to the difference of the magnetism and structure in the two thicknesses.

4.3.3 MCDAD of Fe/Co/Cu(001) at different thicknesses

This subsection deals with MCDAD experiments on Fe/Co/Cu(001) films with different thicknesses. The experimental setup is exactly the same as in Fig. 4.3, except that the magnetization is in the plane consisting of $\mathbf{q}$ and $\mathbf{k}$, and that the rotation axis is along the <110> direction of the sample. Photoemission spectra for opposite magnetization directions were measured as a function of the angle α at room temperature. The sample consists of Fe films, grown on 5 ML Co/Cu(001) at room temperature. The incident light is left circularly polarized with a photon energy set to 900 eV. The binding energies for Fe-$2p_{3/2}$ and Fe-$2p_{1/2}$ are 707 and 720 eV, respectively [59]. The kinetic energy range of the spectra was set to 150 eV to 195 eV. The Fe-$2p_{3/2}$ peak was found at about 186.5 eV. This kinetic energy is even lower than the Co-$2p_{3/2}$ at 216 eV in the earlier experiments, using light with a photon energy of 1000 eV. At this kinetic energy, the photoelectrons are easier diffracted by large angles, and forward scatterring is even less important.

Fig. 4.26a reports intensity spectra for both magnetization directions of the Fe-$2p$ level of a 0.5 Fe/Co/Cu(001) film at normal emission. Fig. 4.26b shows the corre-

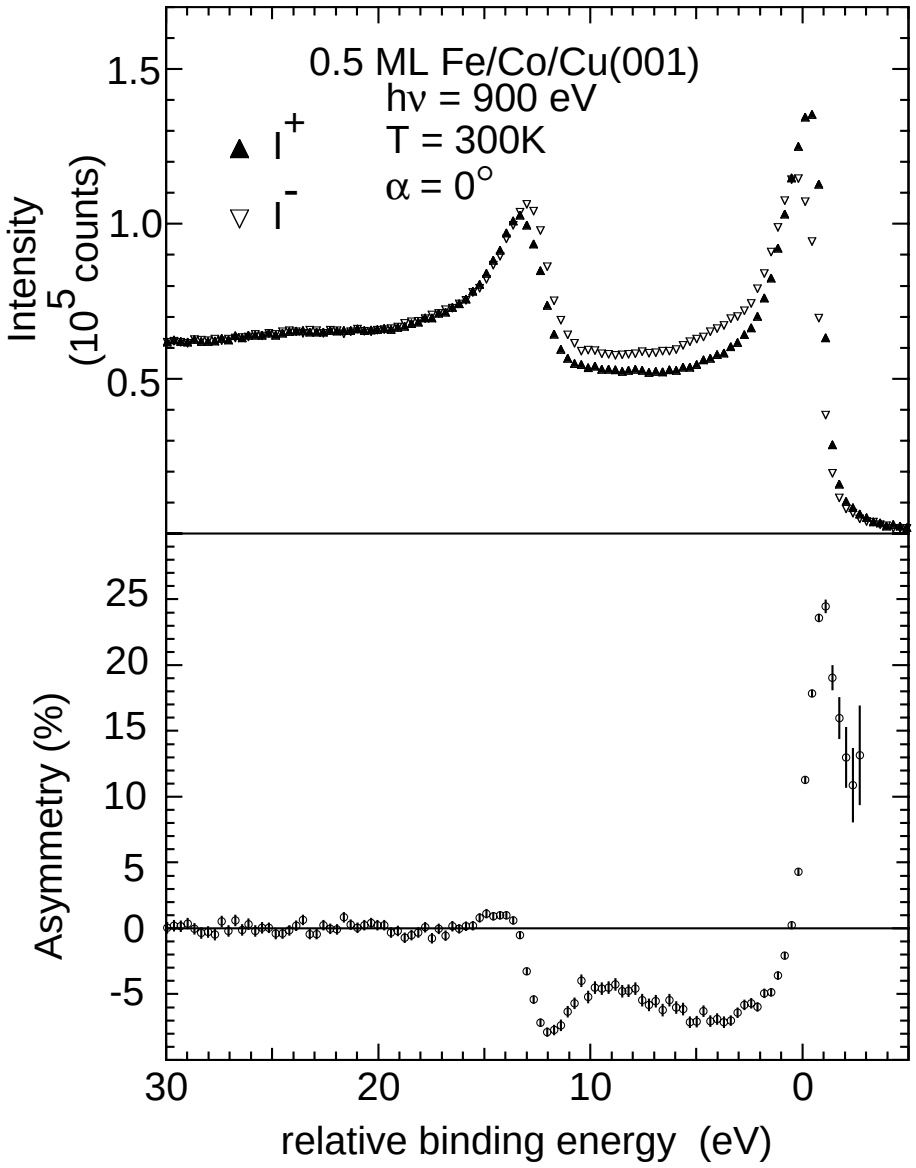

Figure 4.26: a): Fe-2p photoemission intensity spectra for both magnetization directions (I^+ and I^-), measured on a 0.5 ML Fe/Co/Cu(001) at normal emission at 300 K in the MCDAD geometry. b): Dichroic asymmetry spectrum calculated from the photoemission intensity spectra of a).

sponding dichroic asymmetry spectrum. The intensity spectrum is comparable to the spectra using unpolarized light, as were reported before (Fig. 4.24). As already discussed, the circularly polarized light from the synchrotron is monochromatized, the intensity between the $2p_{3/2}$ and $2p_{1/2}$ peaks, and at the high binding energy side of the $2p_{1/2}$ peak with respect to the intensity of the peaks should be thus smaller than using the x-ray tube. However, it is clear from comparing Fig. 4.24 and Fig. 4.26a that the intensity at both energy ranges are much higher. The reason is that the kinetic energy of these photoelectrons is lower than 200 eV. At this energy range the photoe-

mission intensity from secondary electrons will increase from higher kinetic energy to lower kinetic energy. As the photoemission intensity of 0.5 ML is relatively small, the background is therefore higher at higher binding energy range. In Fig. 4.26b, strong "plus/minus" features are observed at both of the $2p$ lines. The whole spectrum is very similar to the asymmetry spectrum measured with unpolarized light, but with a much larger asymmetry value. For the $2p_{3/2}$ level, the maximum of the dichroic asymmetry reaches about 25%, and the minimum about -6%. A small positive peak is now also found at the $2p_{1/2}$ level, which in the case of unpolarized light was not resolved. In Fig. 4.26b a small broad structure centered at ~ 4 eV is visible, which could be due to many-body effects as in the case of the Co/Cu(001) film. However, this feature is much smaller compared with Co.

The Co-$2p$ dichroism was also measured (at $\alpha = -3°$), and it was found by comparing the signs of the "plus/minus" features of the Co-$2p$ lines and Fe-$2p$ lines that the magnetization of Co and Fe are ferromagntically aligned. The kinetic energy of the Co-$2p_{3/2}$ photoelectrons is about 116 eV at this photon energy. This means that these photoelectrons are much closer to the low energy end of the emission spectrum, and will be influenced more strongly by secondary electrons. For that reason, the dichroism of the Co-$2p$ levels was calculated as the normalized intensity difference instead of the dichroic asymmetry in this case.

During the measurement of the angular dependence of the magnetic dichroism, the photoemission intensity varied due to instabilities in the beam position in the storage ring. Although these instabilities of the light intensity can bring some artifacts in the dichroic asymmetry spectra, this influence will be minimized when the template fit can be performed as in subsection 4.2.2. Because the dichroic asymmetry spectrum in Fig. 4.26b has a flat baseline and a good signal-to-noise ratio, it will be used as template for all the analysis of other Fe dichroic asymmetry spectra.

Although this intensity instability of the light was always present, it was found to be less strong during the measurement of 0.5 ML Fe/Co/Cu(001). Therefore, it is possible to get a general view of the angular distribution of the photoemission intensity in this case. Fig. 4.27a shows the α angular dependence of the intensity of Fe-$2p_{3/2}$ peak by adding both the I^+ and I^- spectra. It is clear that there is no intensity enhancement due to forward scattering at normal emission and the photoemission intensity exhibits almost no angular dependence after being corrected by a factor of $\sin(45° + \alpha)$. (This correction has been discussed in subsection 4.2.5 in the case of a 5 ML Co film.) The photoemission intensity around the surface normal is even lower than that at angles far away from the normal. It must be noticed that first at this thickness even at very high kinetic energy there should be no forward scattering along the surface normal. Second, at the chosen kinetic energy there should be no

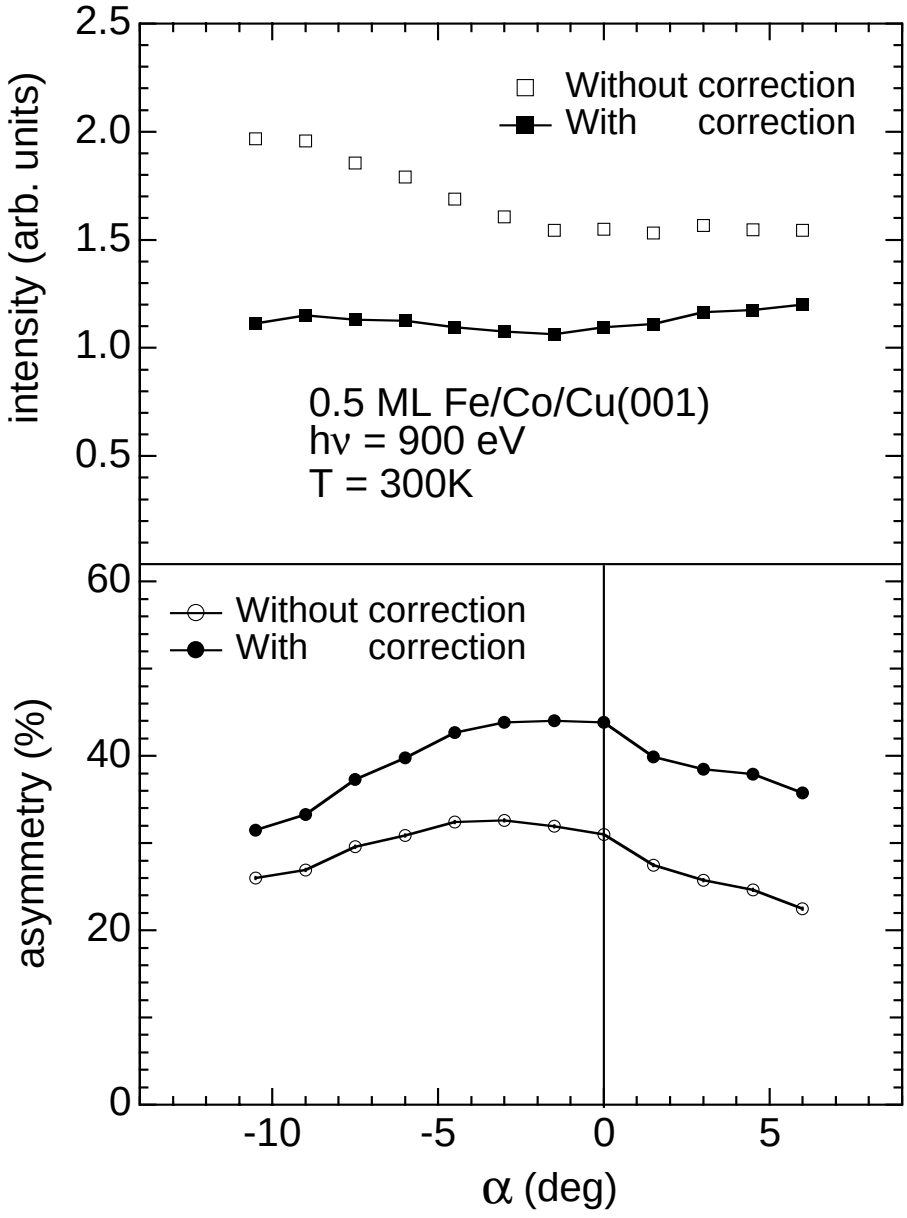

Figure 4.27: a): The α-angular dependence of the peak intensity of Fe-$2p_{3/2}$ ($I^+ + I^-$), measured on 0.5 ML Fe/Co/Cu(001) at 300 K (open squares), and corrected for a light incidence (filled squares). b): Angular distribution of the dichroism, represented by the fit parameter c_0 in maximum peak-to-peak asymmetry, (open circles) and after correction to the change of the direction of the sample magnetization (filled circles).

forward scattering also for thicker films. (This will be demonstrated from the intensity dependence of the 6 ML Fe/Co/Cu film.)

In Fig. 4.27b, the angular distribution of the maximum peak-to-peak, determined from the parameter c_0 of the template fit, is depicted. As discussed in subsection 4.2.5, in this geometry the direction of $\mathbf{M}$ is also changed by varying α. In order to get rid of the influence of that in the angular dependence, the dichroic asymmetry

is corrected by a factor of $1/\cos(45° + \alpha)$. In Fig. 4.27b, both curves, the dichroism asymmetries before (open circles) and after this correction (filled circles) are shown. It is immediately clear that there is an angular variation of the dichroic asymmetry. However, the relative amplitude of this variation is not very strong. The dichroic asymmetry (after correction) exhibits a constant part of about 37% and varies between 31% and 43%.

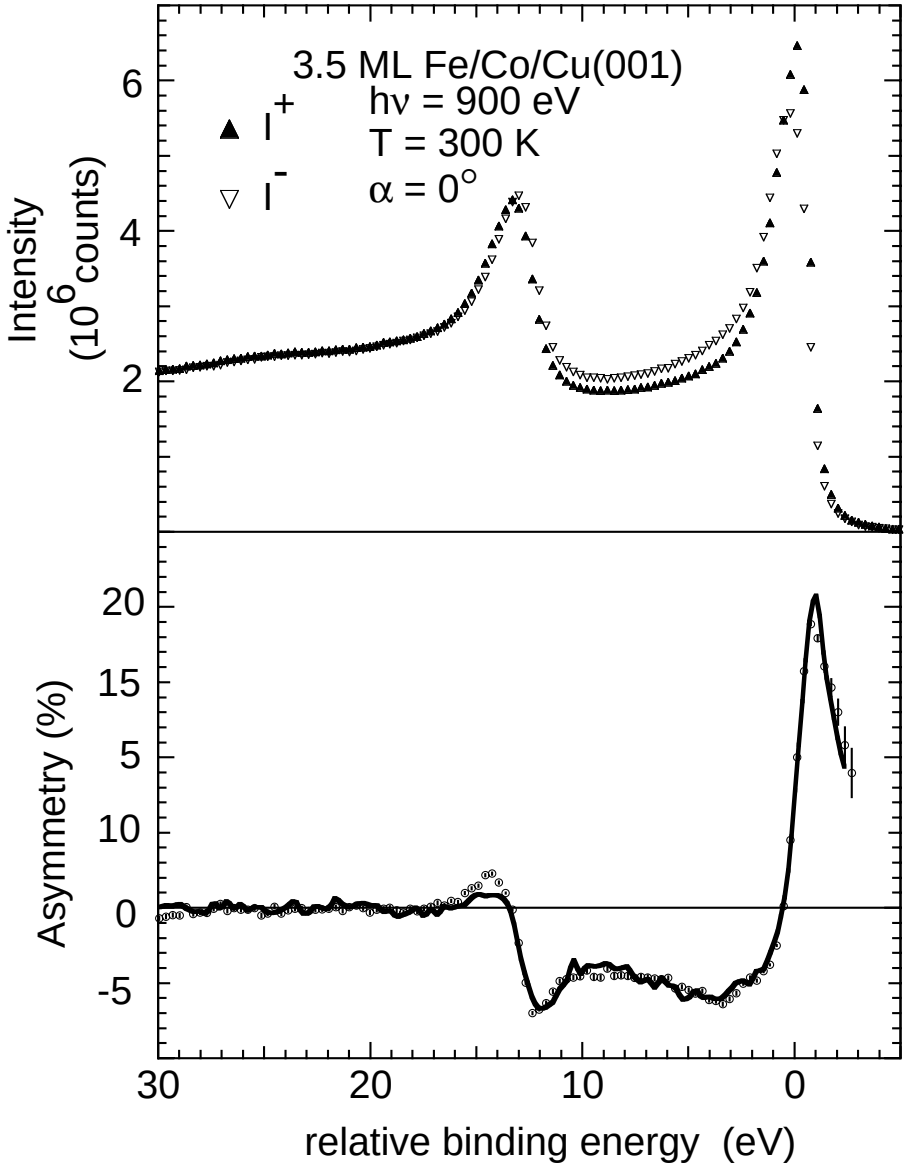

Figure 4.28: a): Fe-2p photoemission intensity spectra for both magnetizations (I^+ and I^-), measured on 3.5 ML Fe/Co/Cu(001) at normal emission and 300 K in the MCDAD geometry. b): The corresponding dichroic asymmetry spectrum after baseline correction by a template fit (open circles), and the template curve, scaled by the fit parameter c_0 (solid line).

Fig. 4.28a shows the photoemission intensity spectra for both magnetization di-

rections of the Fe-2p levels, measured on 3.5 ML Fe/Co/Cu(001) at normal emission. Fig. 4.28b reports the corresponding dichroic asymmetry spectrum after baseline correction by means of a template fit. The solid line is the scaled template curve. It is clear that the template spectrum fits the spectrum well except for small differences at the $2p_{1/2}$ level. A slightly higher positive peak than the one in the template curve can be attributed to the higher photoemission intensity for 3.5 ML Fe compared to 0.5 ML Fe, and therefore a relatively lower background at the $2p_{1/2}$ level (cf. Fig. 4.26a). Comparing Fig. 4.28b with Fig. 4.26b, it is also clear that the whole dichroic asymmetry spectrum is lower than for 0.5 ML Fe. This reduction can be due to the different magnetic moment in 0.5 ML and 3.5 ML. As in the case of 0.5 ML Fe film, the dichroic asymmetry of Co-2p level at $\alpha = -3^\circ$ was measured and it was found that the magnetization of Co and Fe are ferromagnetically aligned.

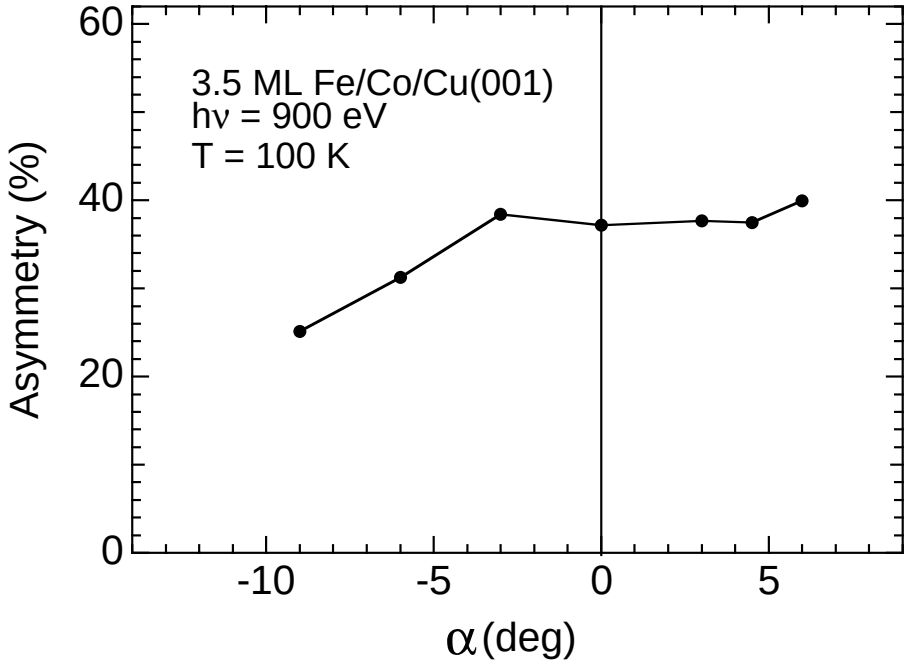

Figure 4.29: Angular distribution of maximum peak-to-peak asymmetry of a 3.5 Fe/Co/Cu(001) film, taken from the fit parameter c_0. The data are shown after correction for the different directions of the sample magnetization (open circles).

Because the intensity of the circularly polarized light changed strongly in this measurement due to instabilities of the beam position, the intensity of photoemission varied strongly. For that reason in Fig. 4.29, only the dichroic asymmetry (represented by parameter c_0) as the function of the angle α is shown. The asymmetry has again been corrected by a factor of $1/\cos(45^\circ + \alpha)$. In this figure, the dichroism shows a small angular variation. The dichroic asymmetry for each angle is smaller than the asymmetry of the 0.5 ML film at the same angles. The amplitude of the variation is

from about 25% to 40%.

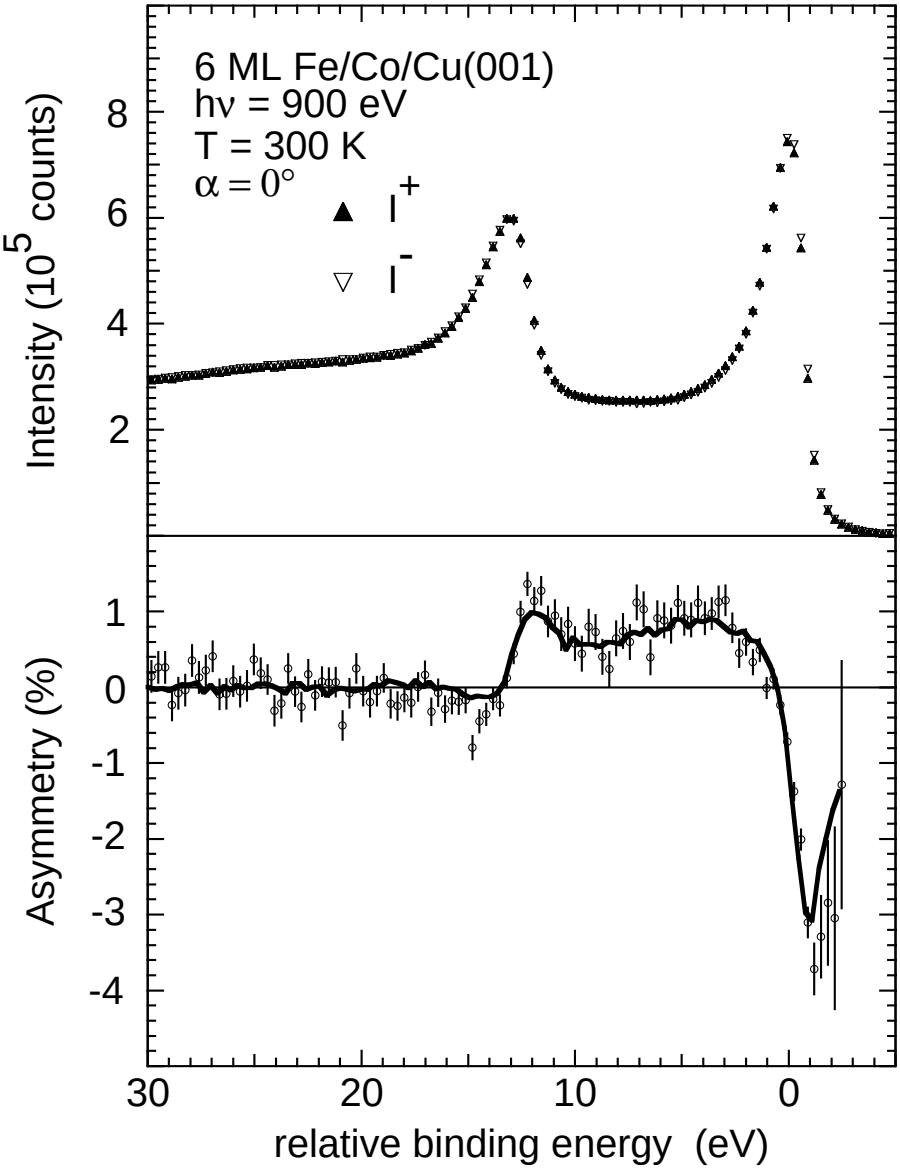

Figure 4.30: a): Fe-2p intensity spectra for both magnetizations (I^+ and I^-) of a 6 ML Fe/Co/Cu(001) film at normal emission and 300 K in the MCDAD geometry. b): The corresponding dichroic asymmetry spectrum after baseline correction by the template fit (open circles), and the scaled template spectrum (solid line).

For comparison, a 6 ML Fe/Co/Cu(001) film was also prepared and measured. Fig. 4.30a reports the intensity spectrum for both magnetizations of the Fe-2p levels at normal emission. Fig. 4.30b shows the corresponding dichroic asymmetry spectrum. The data are baseline-corrected after a template fit (open circles). The solid line is the scaled template curve. Two things become immediately clear: the asymmetry spectrum shows a reversed sign, and the value of the dichroic asymmetry is much smaller compared to the 3.5 and 0.5 ML Fe films. Otherwise, the whole dichroic

spectrum is in every detail in shape similar to those of 0.5 ML and 3.5 ML Fe, as seen by the well fitting template curve. The maximum asymmetry at Fe-2$p_{3/2}$ is about -3%, with a reversed sign. In order to understand why the sign of the asymmetry spectrum is reversed, the dichroic asymmetry of Co-2p level at $\alpha = -3°$ was measured as in the case of 0.5 ML and 3.5 ML Fe film. However, the sign of the asymmetry spectrum of Co is not reversed compared to that in the 0.5 ML and 3.5 ML Fe samples. This immediately shows that the net magnetizations of Co and Fe are antiferromagnetically aligned. By comparing the normalized intensity difference of Co-2$p_{3/2}$ for the three films at $\alpha = -3°$, it was found that the value and shape are exactly the same within the experimental error (less than 20% of the dichroism). This shows immediately that the Co film underneath is fully magnetized in 6 ML/Co/Cu(001) film, like it is at other thicknesses. The reversed dichroic signal of Fe indicates antiferromagnetic coupling between the Co film and the net magnetization of the Fe film.

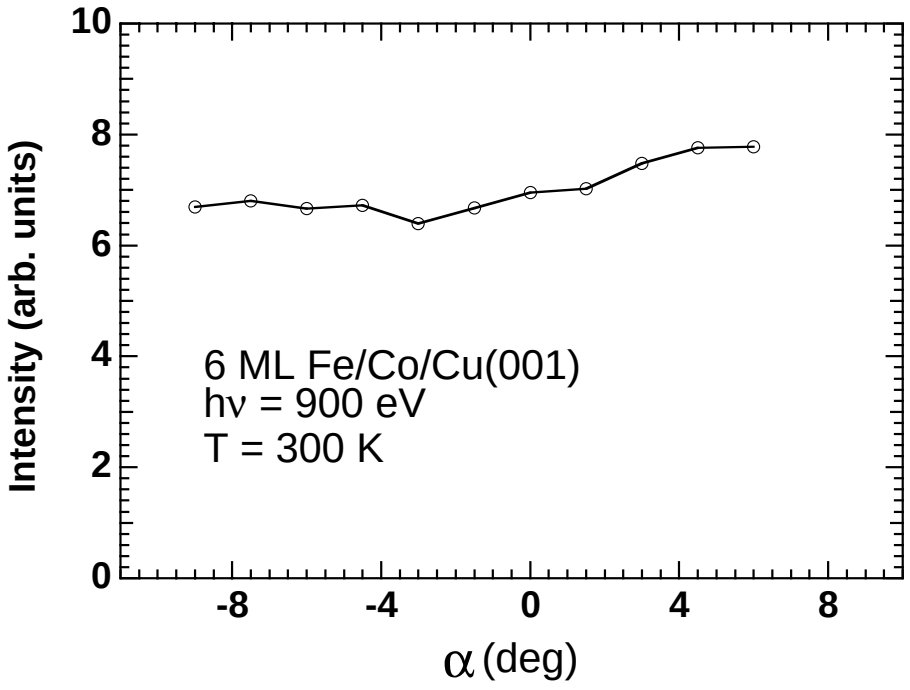

Figure 4.31: Angular distribution of the peak intensity of Fe-2$p_{3/2}$ ($I^+ + I^-$). The sample is a 6 Fe/Co/Cu(001) film, measured at 300 K.

The dichroic spectra have also been measured, as before, as a function the emission angle α. However, it was found that during these measurements for different angles the dichroic signal dropped as a function of time. By comparing the asymmetry at the same angle ($\alpha = -3°$), this drop is about 60% from starting the experiment about half hour after the film growth to one hour later (The spectra in Fig. 4.30 have been measured at about 20 minutes after the first experiment). The vacuum conditions

here are the same as before ($< 2 \times 10^{-10}$ mbar), and no such strong magnetic signal drop has been found for 0.5 ML and 3.5 ML film. This strong reduction means that this film could be in a metastable magnetic state. More experiments need to be done in order to find out the exact reason for this behavior. With such a strong time-dependent reduction of the magnetic signal, it is difficult to measure the angular dependence of the dichroism. However, it is at least possible to measure the angular dependence of the photoemission intensity.

This is shown in Fig. 4.31, in which the angular dependence of the intensity of the Fe-$2p_{2/3}$ photoemission peak by adding the I^+ and I^- is depicted. Although the stability problem of the incident light brings some scatter in this distribution, it is still clear that there is no enhancement of forward scattering. The angular distribution is very similar to the case of 0.5 ML Fe in Fig. 4.27a.

5 Discussion

5.1 Co/Cu(001)

From the angular dependences of MDAD of Co films, it has been shown that there are variations of magnetic dichroism around the sample normal and other low index axes, which cannot be explained by the free-atom model and must be due to diffraction effects in the present geometry. The strength of these variations around the sample normal was found to be dependent on the thickness (cf. Figs. 4.11 on page 36 and 4.13 on page 38), the sample temperature (cf. Fig. 4.8 on page 32), the photon energy of the light source (cf. Figs. 4.7b on page 31 and 4.21b on page 51) and the experimental geometry (cf. Figs. 4.21b on page 51 and 4.23 on page 53). Around a low index axis in a thick Co film, this strength is then mainly dependent on the strength of forward scattering along this low index axis (cf. Figs. 4.16b on page 42 and 4.18b on page 45). In this section, after a simple model is introduced to understand the underlying physics of diffraction effects in MLDAD, discussion will be made in detail about all the above factors, which influence the diffraction effects.

5.1.1 The principle of the diffraction effects in MLDAD

As mentioned in the introduction, the angular distribution of the dichroic signal measured in an MLDAD experiment is influenced by two contributions.

The first one is well described using a simple atomic model, and depends on the dipole excitation matrix elements for the two channels available as final states (atomic-like term). It depends only on the relative orientation of the photon and photoelectron wavevectors, and magnetization direction, in agreement with theories developed in Ref. [21] by Cherepkov and in Ref. [35] by Menchero. In reality, in a solid the photoelectron will experience a non-spherical potential, differently from the case of an isolated polarized atom, and the outgoing electron wave (direct wave) could present a small angular dependence [61]. Moreover, in the present experimental geometry, by varying the emission angle the direction of light incidence with respect to the surface normal is also changed. The excitation process depends on the angle of incidence. In particular it has to be recalled that MLDAD involves a phase shift difference $\delta = \delta_0 - \delta_2$ between the two interfering final state channels with $l = 0$ and $l = 2$ angular momentum (s and d waves), in agreement with the transitions allowed by the dipole interaction, whereby the dichroism scales with $\sin\delta$ (see section 2.3). In a purely atomic theory this phase shift does not depend on the incidence angle. However, *a priori* the same behavior cannot be assumed for atoms interacting in a solid.

The second contribution is due to the scattering of the photoelectrons with the

atoms in the solid (diffraction-related term). This term does not give origin to a new dichroism, but merely modulates the dichroic signal. In other words, the dichroism is already present as soon as the photoelectron is excited from the atom, and is modified by photoelectron scattering.

The observed strong angular dependence of the dichroism around normal emission for a thick Co film (cf. Figs. 4.11 on page 36 and 4.13 on page 38) immediately indicates thus that photoelectron diffraction is a dominant effect in off normal emission geometries. A simple diatomic heuristic picture of the underlying physics has been

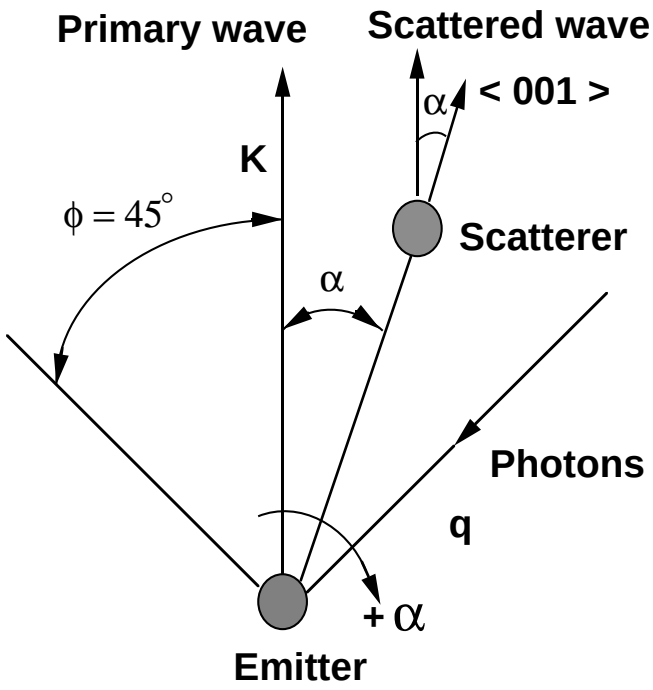

Figure 5.1: The geometry for emission and scattering in the two atom cluster model. The angles α and ϕ are both defined for rotation around the magnetization being perpendicular to the plane of the figure.

given in Ref. [17]. Because in thick Co/Cu(001) films forward scattering dominates at kinetic energies used in the present experiments ($\sim$ 500 eV), only interference with diffracted forward scattering electrons is taken into account. In this model, only d-channel emission from the two-atom cluster, with a geometry as shown in Fig. 5.1, is considered. This means that no magnetic dichroism in the pure sense, which depends on the interference between the s and d channels, is included. As already known, only the p-component of unpolarized light has to be discussed, because the s-component does not contribute to the dichroism. In the dipole approximation, the p-component of the unpolarized light yields photoelectron amplitudes for the $|3/2 \ \pm 3/2\rangle$ core states that are proportional to $1 + 3e^{\pm 2i\phi}$ [17], where ϕ is the electron emission angle

(see Fig. 5.1). The amplitudes of the primary waves at the electron detector are thus $1 \pm 3i$ for the primary unscattered wave at $\phi = 45°$. At the position of the scatterer $\phi = 45° + \alpha$, so the amplitudes at the scattering atom are proportional to $1 \pm 3ie^{\pm 2i\alpha}$. The scattered wave at the electron detector can be written as proportional to:

$$A_{sc}(3/2,\ \pm 3/2) = (1 \pm 3ie^{\pm 2i\alpha})|f(\alpha)|e^{i\delta(\alpha)}, \tag{5.1}$$

where $|f(\alpha)|$ is the magnitude of the scattering factor, and $\delta(\alpha)$ is the total phase shift due to both scattering and path-length difference. Assuming the same overall phase shift $\delta(\alpha)$ for both $|j,\ \pm m_j\rangle$ states, the total amplitude at the electron detector is the sum of the primary and scattered waves. Then the intensity difference between the two levels is proportional to:

$$I(3/2,\ \ 3/2) - I(3/2,\ \ -3/2) = 12|f(\alpha)|\sin[\delta(\alpha)](1 - \cos 2\alpha - 3\sin 2\alpha). \tag{5.2}$$

The same calculation for the $m_j = \pm 1/2$ levels yields the result:

$$I(3/2,\ \ 1/2) - I(3/2,\ \ -1/2) = 4|f(\alpha)|\sin[\delta(\alpha)](1 - \cos 2\alpha - 3\sin 2\alpha). \tag{5.3}$$

As discussed in section 2.3, the intensity difference between $|j,\ m_j\rangle$ and $|j,\ -m_j\rangle$ gives precisely the magnetic dichroism. Especially, equation (5.2) gives the unnormalized magnetic dichroism for the $j = 3/2$ level. For small angles α, equation (5.2) can be simplified to first order in α as:

$$I(3/2,\ \ 3/2) - I(3/2,\ \ -3/2) = 12|f(\alpha)|\sin[\delta(\alpha)]\alpha. \tag{5.4}$$

As discussed in Ref. [17], $\delta(\alpha)$ and $f(\alpha)$ are non zero and slowly varying with α close to the forward scattering peak, therefore equation (5.2) gives a dichroism proportional to α and antisymmetric around $\alpha = 0°$. For the $j = 1/2$ level, similar results can be deduced from Eq. 5.3 but with a different factor. The proportionality of the dichroism in (5.2) and (5.3) to $|f(\alpha)|\sin[\delta(\alpha)]$ makes clear that such a term requires scattering and diffraction, which means that $|f(\alpha)|\sin[\delta(\alpha)] \neq 0$. Equation (5.2) is zero for $\alpha = 0°$, showing that along the sample normal the contribution due to scattering disappears within this simple heuristic diatomic model. However, this does not mean that along the normal there is no dichroism. Even if along the normal there is no diffraction contribution to the dichroism, there is still the contribution from the atomic-like term, which is not considered in this simple model, where only the d-channel photoemission is included to show the influence of diffraction. For MDAD using unpolarized light, the interference of the $s - d$ channels is essential, as pointed out before. Considering this interference and using the diatomic model of Ref. [19], Schellenberg *et al.* show, to first order in α, that the dichroism consists

of the diffraction-related term plus one term related to the $s-d$ phase shift. The latter term is related to the atomic-like dichroism, but with a factor depending on $f(\alpha)$ and $\delta(\alpha)$ [19]. Along the normal this term still exists, and depends on $f(\alpha)$ and $\delta(\alpha)$ [19]. This shows that the dichroism will not disappear along the normal, and that the dichroism due to scattering can give residual effects also at $\alpha = 0°$. However, generally along the low-index axes (in the present case the sample normal) the atomic-like term dominates in the magnetic dichroism [19]. In Fig. 4.7b on page 31, the data for 5 ML Co/Cu(001) film can be described by a constant part plus an antisymmetric part with an angular shift of $\sim 0.5°$ off the normal direction. The data for other films can be similarly described, but with a different constant part plus an antisymmetric part with a different angular shift (cf. Figs. 4.11 and 4.13). This kind of angular shift from the normal direction could be due to residual diffraction effects along the normal direction. Another possible explanation for this kind of shift could be that the variation of the light incidence angle has also an influence, which in this model is not included.

Because the template curve fits well every spectrum $Asy(E, \alpha)$ at different emission angle α in Fig. 4.6 on page 29, and the parameter $c_0(\alpha)$ in Fig. 4.7b has an antisymmetric dependence with respect to $\alpha = 0.5°$, the diffraction contribution at each binding energy for the 5 ML Co film can be thought to be proportional to the dichroism in the template curve at the same binding energy with an angle-dependent factor. This is true also for other Co films, as they have similar angular dependence and the template curve fits well every spectrum $Asy(E, \alpha)$ (cf. Figs. 4.9 on page 34 and 4.10 on page 35). From equations (5.2) and (5.3), it is clear that the asymmetries for both levels have the same angular dependence with just a different factor $(1 : 3)$. Remember that from one electron theory (cf. section 2.3), the magnetic dichroism ratio for the two levels is exactly $1 : 3$. Therefore diffraction effects in this simple model are proportional to the atomic dichroism, scaling with the same angular-dependent factor for the two levels. This is consistent with the present experimental results.

If the effects due to the variation of the light incidence angle in the present geometry are negligible, from a simple symmetry consideration it can be also concluded that the asymmetry signal should be antisymmetric around normal emission. Reflection at the mirror plane containing $\mathbf{M}$ and the surface normal changes the α angle between $\mathbf{k}$ and the surface normal to $-\alpha$. Without considering the influence of the light incidence direction, which is also changed by this reflection, the result is exactly like a measurement at $-\alpha$. In this mirror operation $\mathbf{M}$ changes its sign, so that the sign of the asymmetry will be changed. This immediately shows that the dichroism should be antisymmetric around the normal direction.

From above discussion, it can be concluded that the diffraction effects induce the

antisymmetric variation of the dichroism around normal emission and that the atomic-like term should dominate for normal emission [19, 10]. It is now of importance to discuss both the absolute size of the magnetic dichroism of the atomic-like term and the dichroic spectrum itself. The former depends mostly on the magnetic moment, which will be discussed in the next subsection. Here, therefore, only the dichroic spectrum itself will be discussed. As the template curve fits well every dichroic spectrum at any emission angle for different films, at different temperatures, with different photon energies and different geometries, the dichroic spectrum of 5 ML Co/Cu(001) at normal emission could be used for this discussion. From Fig. 4.5 on page 27, the peak height of the $2p_{3/2}$ is found to be 3.3% at normal emission. It should be noticed that there is a contribution to the dichroism also in the region between the $2p_{3/2}$ and $2p_{1/2}$ peaks, where no dichroism is expected from one-electron theory. The strong similarity between the $2p_{3/2}$ and $2p_{1/2}$ lineshapes in the intensity spectrum suggests to exclude this difference as being due to spin dependent scattering effects. Moreover, as discussed in detail in Ref. [18], this dichroism cannot be attributed only to secondary electrons, because their number would be proportional to the Co-$2p_{3/2}$ intensity, which is very similar for the two magnetizations. As also discussed previously in Fig. 4.4a, a feature at $\sim$ 5 eV was observed. A similar feature appears also in the Fe-$2p$ photoemission curves, in experiments which use monochromatized linearly-polarized light [18]. For this reason it cannot be due to spurious photons with higher energy, created in the x-ray source. This can be proven by the Co-$2p$ dichroic spectrum using monochromatized circularly polarized light in Fig. 4.20b on page 49, where this feature was also found. As discussed in Ref. [15], a similar feature in energy position and lineshape has been attributed to a reminiscence of the localized nature of the d electrons of cobalt, and arises due to the interaction of valence states with the core hole formed in the photoemission process (screening), which leads to discrete satellites in the intensity spectra. A typical example of this kind of satellite is the "6 eV" satellite of the Ni $2p$-spectrum [63]. A narrow d band in Ni is responsible for the formation of correlation-induced spectral features. In a similar context this feature in the Co-$2p$ spectrum could be discussed. For Ni, Co, and Fe, the satellites are spin-polarized and carry information about spin dependent correlations and the screening process. The spin polarization of these many body satellites gives rise to the characteristic features in the magnetic dichroism, which are responsible for the multiplet structure in the region between the $2p_{3/2}$ and $2p_{1/2}$ peaks [15]. An indication of this feature is also found in the MLDAD spectrum, calculated by Thole and Van der Laan [64].

It is now known that there are two contributions: atomic-like term and diffraction-related term. In the next subsection, it will be discussed how the two terms behave

upon the changing temperature and changing thickness.

5.1.2 Temperature effect and thickness dependence

By comparing Fig. 4.13 on page 38 and Fig. 4.11 on page 36, it is clear that the temperature is an important factor in the diffraction effects in MDAD. As an example, the angular dependences of MLDAD for the 5 ML Co/Cu(001) film at 100 K and at 300 K will be discussed (cf. Fig. 4.8 on page 32). The amplitude of the variation of the dichroic signal for the 5 ML Co/Cu(001) film is reduced at 300 K with respect to 100 K, however, the signal along the sample normal remains almost unchanged. As already discussed, along the sample normal the dichroism is mainly of atomic character. The atomic-like dichroism depends on the magnetic moment. From Ref. [22], the Curie temperature T_c of 5 ML Co/Cu(001) can be deduced to be 850 K. The temperature dependence of the magnetization close to the critical temperature can be described by the power law:

$$M(T) \propto (1 - T/T_c)^{\beta_c}, \tag{5.5}$$

where β_c is the critical exponent of the phase transition [65]. The theoretical value of β_c in a two-dimensional system corresponding to a spin system that can take only two spin orientations (Ising model) is 1/8 [66], while for a three-dimensional system it is between 0.3–0.4 [65]. From these parameters, the reduction in the magnetization of 5 ML Co can be estimated to be $4 - 12\%$ for decreasing the temperature from 300 K to 100 K ($M_{300\mathrm{K}}/M_{100\mathrm{K}} \sim 0.91 - 0.88$ when $\beta = 0.3 - 0.4$, and $M_{300\mathrm{K}}/M_{100\mathrm{K}} \sim 0.96$ when $\beta = 1/8$). This would be consistent with the data at normal emission, assuming the size of the dichroism at $\alpha = 0°$ to be purely dependent on the magnetic moment. At this angle the dichroism is observed to be $\sim 5\%$ lower at 300 K with respect to 100 K (cf. Fig. 4.8).

As discussed before, the diffraction-related term can be thought of as a product of the atomic-like term and an angle-dependent factor, the reduction in magnetic moment should also influence this term. However, this influence is very tiny for the 5 ML Co film and cannot explain the difference in the angular dependence of the dichroism between 100 K and 300 K in Fig. 4.8. The film temperature mainly affects the photoelectron intensity, and consequently the dichroic asymmetry through the Debye-Waller factor [2]. In particular a loss of constructive interference between the undiffracted and diffracted photoelectron waves is expected for higher temperatures, that should be reflected in a reduction of the scattering effects and a broadening of the angular distribution of the intensity, and consequently of the asymmetry. From Fig. 4.8, a decrease of the amplitude (from 9.5% to 6.0%) and an increase of the width

of the angular modulation of the asymmetry is observed for changing the sample temperature from 100 K to 300 K.

Generally for a Co film at a given thickness, the temperature can influence the angular dependence of MDAD in two ways. The first one is the Debye-Waller effect, which reduces the angular variation of the dichroism, as discussed for the 5 ML Co film. The second one comes from the change of the magnetic moment, when the temperature changes and the Curie temperature is comparable with the sample temperature. It actually affects the atomic-like term mainly, however, the change of the atomic dichroism should also change the amplitude of the dichroism variation. As Curie temperature changes strongly upon the varying thickness with thickness of several monolayers [27], this second effect is strongly dependent on the film thickness. This shows already the importance of the thickness, which will be discussed in the following.

It was shown that forward scattering plays a dominant role in the diffraction effects in MLDAD. Because forward scattering is especially sensitive to the film thickness in the range of only a few atomic monolayers, and was widely used to study the surface structure of thin films [53, 54, 58], it was a logical consequence to study the thickness dependence of diffraction effects in MDAD.

At both 100 K and 300 K, it was shown that the variations of the dichroism around the sample normal are reduced when going from thick to thin films (cf. Figs. 4.11 and 4.13). This can be explained by a reduction of the diffraction effects for the thinner films. When the film thickness is reduced to 2 ML or less, along the <001> surface normal in an fcc structure, there would be no more forward scattering, because no atoms are available to focus the photoemission coming from the film atoms. This is the main reason why the amplitudes of the 1.5 ML and 2 ML are strongly reduced compared to 5 ML (cf. Fig. 4.11). There is, however, as shown in Fig. 4.11, still a small variation of the dichroism around the normal for 1.5 ML and 2 ML. The origin of the residual small modulation visible in Fig. 4.11 for both 2 and 1.5 ML will be discussed in the following.

At small thicknesses (less than 2 ML), the epitaxial Co films are found to be composed by a significant amount of bilayer islands resulting in a strong deviation from the ideal layer-by-layer growth [22]. Starting from 2 ML, the growth mode changes towards a more perfect layer-by-layer growth, but the film still contains a certain number of voids and additional islands [22]. The roughness at thicknesses of integral numbers of layers is found to be confined to the uppermost layer, and to be of the order of ± 1 ML [22]. Actually even at 1.5 ML thickness, there will be many islands with 2 monolayer thickness, which allow emission along <011> diffracted by 45° into the normal direction. Of course, there will be also other scattering processes

into normal direction by nearby atoms along other low index directions with a larger diffraction angle than 90°. It is also noticeable that there will be emission along the normal into the Cu substrate which can be diffracted by 180° out of the sample surface. Although these diffraction events by a large angle are comparatively rare at kinetic energies of several hundred eV, they may still be important when forward scattering along the normal is absent. This could be a reason for the weak maximum along the sample normal in the intensity angular distribution at 2 and 1.5 ML (Fig. 4.12 on page 37). Therefore one possible explanation for the small modulation in the dichroism data of 1.5 and 2 ML Co/Cu(001) relies on diffraction effects due to interference with photoelectrons emitted into other crystallgraphic directions and then diffracted into the normal <001> direction, which could enhance the photoelectron intensity along the sample normal, as it is shown in Fig. 4.12. Another possible explanation could be related to a few islands with 3 ML thickness at the 1.5 ML and 2 ML films, because there is roughness of ±1 ML. In that case there would be forward scattering along the normal <001> direction of these islands, which could induce the small modulation in the dichroism.

There are clear forward scattering peaks along the normal direction for films thicker than 3 ML, as was shown in Fig. 4.12. However, the diffraction effects still increase from 3 ML to 5 ML at 100 K (cf. Fig. 4.11). The reason must be the intensity contribution from atoms deeper than 3 ML in the 5 ML film. Except for forward scattering in photoemission along the normal, there will be photoemission coming from the top two layers which are not scattered in forward direction and experience only little diffraction effects. In an ideal 3 ML film there is only 1 layer at which photoelectrons can be scattered forwardly, while there are 3 layers in the 5 ML film. Even considering the photoelectron mean free path length (about 3 ML at the present kinetic energies) [67], the contribution from lower layers will still significantly increase from 3 ML to 5 ML. Because the dichroic asymmetry is the total intensity difference of I^+ and I^- divided by the sum of both, the additional photoemission intensity with the characteristics of forward scattering diffraction effects in the 5 ML film coming from lower layers will result in stronger diffraction effects in the magnetic dichroism compared to the 3 ML film. In the same way, the increase of the diffraction effects at 300 K can be explained (cf. Fig. 4.13).

As mentioned above, there are two contributions to the MDAD: the atomic-like term and the diffraction-related term. It is reasonable to discuss also the atomic-like term for films of different thickness.

An interesting point appears from the comparison of the 5 and 1.5 ML Co-2$p_{3/2}$ dichroism along the sample normal, where the diffraction effects are negligible, and the atomic-like term dominates in the dichroic asymmetry (see previous subsection)

[19, 10]. From Fig 4.11, at $\alpha = 0°$ the maximum peak-to-peak asymmetry for 1.5 ML (2.0%) is 47% of that of 5 ML (4.4%). Recently Schellenberg *et al.* [19] performed an MLDAD experiment using unpolarized light in an Fe-based amorphous sample ($Fe_{78}Si_{13}B_9$ metallic glass). They found the atomic-like dichroism of Fe in the metallic glass to be reduced by about 30% with respect to that in epitaxial Fe films. This reduction was explained as being mostly due to the smaller Fe magnetic moment in the metallic glass (86% of that in epitaxial Fe films). Within this picture the difference between 1.5 ML and 5 ML Co films may be explained considering the smaller magnetic moment of Co in the 1.5 ML film compared to the 5 ML films as due to temperature effects. From Ref. [22], the Curie temperatures for 1.5 ML and 5 ML are found to be 130 K and 850 K, respectively. For a second order phase transition Eq.(5.5) can be used to calculate the ratio between the magnetic moments for the two films at 100 K to be $M(100\ \mathrm{K})_{1.5\mathrm{ML}}/M(100\ \mathrm{K})_{5\mathrm{ML}} \sim 85 - 87\%$. However, the magnitude of the dichroic asymmetry does not provide direct quantitative information on the magnetic moment, but rather indicates the trend. From this consideration, the discrepancy between the value obtained in the present investigation (47%) and calculated ratio ($\sim 85\% - 87\%$) using an Ising model can be understood.

Another possible explanation could be connected to a different value of the phase shift $\delta = \delta_0 - \delta_2$ for Co atoms in different films, which cannot be considered a *priori* as identical, and that could influence the atomic-like dichroism differently in the two films. Another possible explanation is related to the residual diffraction effects along the sample normal, which should be different for 1.5 ML and 5 ML. As discussed previously, from the Eq.(3) of Ref. [19], which gives the magnetic dichroism including diffraction effects in a two atom cluster model, it is clear that along normal emission there could still be residual diffraction effects. As the small angular dependence of the dichroic asymmetry in the 1.5 ML case could possibly be due to diffraction effects from larger angle scattering, it is understandable that these effects could possibly also have an influence on the dichroic asymmetry along the surface normal. In a 5 ML film diffraction effects are mainly coming from forward scattering along the sample normal, which does not exist in 1.5 ML. Therefore, if there are still residual diffraction effects, these should be qualitatively different between 1.5 ML and 5 ML. As the atomic-like term dominates along the sample normal, the comparison of the dichroic asymmetry in normal emission for different thicknesses will provide also information on the change of magnetic moment due to different Curie temperatures.

As discussed before, the magnetic moment of the 1.5 ML Co film is strongly reduced with respect to the 5 ML Co film. A smaller atomic dichroism for a thinner film related to a smaller magnetic moment could also lead to a smaller amplitude of the angular modulation of the dichroism, especially at 1.5 ML. The strongly reduced

amplitude of 1.5 ML in Fig. 4.14 could partially explained by this effect. However, the strong increase of the period for the modulation in Fig. 4.14 can only be explained by the stronly reduced diffraction effects in MLDAD.

Generally, diffraction effects from forward scattering dominate in thick films, are reduced in thinner films, and become almost negligible in 1.5 ML film. This thickness dependence of diffraction effects then can be applied to study the magnetic and structural properties of the ultrathin magnetic film on the surface.

5.1.3 Other low index axes

It was shown that around the sample normal there is a strong variation of the dichroism mainly due to the forward scattering along <001> axis of the sample. Such an effect should also exist around other low index axes, where there is also strong forward focusing. In Fig. 4.16b on page 42, strong variations of the magnetic dichroism were observed along both the <001> and <011> directions, where strong intensity peaks were found for both directions (cf. Fig. 4.16a). There are also variations of the dichroism around other low index axes (cf. Figs. 4.16b and 4.18b on page 45), which are generally smaller due to the weaker forward scattering effect there. When one of these axes is close to another axis, the influence of neighboring low index axes complicates the angular dependence of the magnetic dichroism (for example the <013> and <012> axes in Fig. 4.16b). The fact that the size of the modulation of the dichroism around a low index axis correlates to the strength of the forward focusing proves that the forward scattering dominates the diffraction effects at the present kinetic energies.

It is very interesting to compare the variation of the dichroism around the <001> axis and around the <011> axis, especially the dichroic asymmetry along these two axes, where the atomic-like term should dominate. It is clear in Fig. 4.16b that the amplitude of this variation around the <011> axis is not smaller than that around the <001> axis. In Ref. [19], in which a bcc Fe(001) sample was studied, Schellenberg *et al.* found a reduced variation amplitude along the <011> axis. A possible reason for this discrepancy could be due to the different structure. In a bcc structure along the <011> axis forward scattering occurs in every second layer. On the contrary, in an fcc structure every layer contributes to forward scattering in <011> direction. Forward scattering along the <011> axis in the fcc Co film, which is even stronger than that around the <001> axis in Fig. 4.16a, gives a strong variation of the corresponding dichroic asymmetry. As discussed before, the atomic contribution should dominate at exactly the low index directions of the crystal. This is again proven from the present data, where the asymmetry at <011> is about 2.6%, identical to the one at <001> (2.5%) (cf. Fig. 4.16b). Along the <011> axis there will be forward scattering in films thicker than only 1 ML, whereas for the <001> direction this effect exists only

when the thickness of the film is at least more than 2 ML. For that reason, diffraction effects in MLDAD for the <011> axis will be expected to have a much stronger thickness dependence when the film thickness is between 1 ML and 2 ML. Moreover, the forward scattering effect along <011> exists at lower photoelectron energies than along <001> [57]. This kind of difference will give more possibilities to choose different axes to study diffraction effects in MLDAD to obtain more structural and magnetic information than from just one low index direction. However, the disadvantage to study diffraction effects along the <011> axis are firstly, the photoemission intensity decreases around the <011> axis due to the reduced effective probing depth of the photoelectrons, as mentioned before. Secondly, the <100> axis must be set along the rotation axis with very high accuracy to have the <011> axis in the plane defined by **q** and **k**. The angular dependence of both intensity and dichroism will be very different if the rotation axis is not well adjusted. Along the <001> axis, the precise adjustment of the azimuth is not so crucial, because at the surface normal the exact setting of the azimuthal angle is not important. Very similar diffraction effects in MDAD around the normal were shown in the <110> azimuth (cf. Fig. 4.18b), or in other azimuthal directions in between <100> and <110> (cf. Fig. 4.19b on page 47). The amplitude of the oscillation, however, can be slightly different.

Although it is complicated to discuss the exact behavior of the dichroism by rotating the azimuthal angle with a fixed emission angle, there should be also a variation of the asymmetry around the low index axis from the same consideration as before in the two atom cluster model. This is demonstrated from Fig. 4.17 on page 44, where a strong oscillation of the dichroic asymmetry is observed around the <011> direction. By rotating the azimuthal angle, the difference in the path lengths of the primary waves and the diffracted waves will also be changed, which causes the dichroic asymmetry to vary around the low index axes.

5.1.4 Lower kinetic energies

Using circularly polarized light with a photon energy of 1000 eV, the kinetic energies of the photoelectrons from Co-2p levels are relatively low so there is no prominent forward scattering effect along the <001> axis (cf. Fig. 4.21a on page 51). Fig. 4.21b shows that a variation of the dichroic asymmetry around the sample normal is still present in the geometry for MLDAD, which is smaller compared to the one using unpolarized light of higher photon energy at the same thickness. At lower energies the diffraction probability does not strongly vary with the diffraction angle, all possible diffraction paths must be considered. Although these interference processes are complicated, from the consideration of the symmetry of the experimental geometry, disregarding the change of light incidence, this variation of the dichroic asymmetry

should be still antisymmetric around the sample normal. This is proven by Fig. 4.21b.

In the geometry for MCDAD, the dichroic asymmetry in Fig. 4.23 on page 53 varies as a function of α even after the influence of the change of $\mathbf{M}$ direction is taken out. This shows that the diffraction effects also exist in MCDAD. After the correction by $1/\cos(45°+\alpha)$, an antisymmetric angular dependence of the dichroism in MCDAD (like in MLDAD) should be expected from a simple symmetry consideration. Reflection at the mirror plane, which is vertical to the sample surface and the reaction plane containing $\mathbf{q}$ and $\mathbf{k}$, changes the angle between $\mathbf{k}$ and the surface normal $\mathbf{n}$ from α to $-\alpha$. Without considering the influence of the light incidence direction, which is also changed by this reflection, the result is exactly like the measurement at $-\alpha$. In this mirror operation, $\mathbf{M}$ will not change the sign, but the helicity σ will. As reversing the magnetization generates the same magnetic dichroism as reversing the helicity in the geometry of MCDAD (see section 2.3), the sign of the asymmetry will be changed. This immediately shows that the dichroism should be antisymmetric around the normal like in MLDAD. Although there is not enough data at $\alpha > 0°$ to demonstrate the antisymmetric angular behavior in Fig. 4.23 like in MLDAD, diffraction effects in MCDAD are shown to be equally important than in MLDAD. To compare the absolute value of the dichroism in MCDAD with theoretical results or other measurements, it is very important to carefully include these effects.

5.2 Fe/Co/Cu(001)

In the Fe/Co/Cu(001) film, the magnetic properties are non-uniform over the thickness, and a method is needed which permits one to obtain information about the distribution of magnetic properties within a single film of the same element. For such a purpose the techniques which provide integral information, such as MOKE and XMCD in absorption, are not suitable. The diffraction effects in MDAD should allow to study structural and magnetic properties of thin films and surfaces at the same time, as was shown for Co/Cu(001) films. The diffraction effects in the photoelectron intensity angular distribution and in MDAD will give information about the film structure, and about the structure of the ferromagnetic portion of the film, respectively.

In Fig. 4.25b on page 58 a strong angular variation of the Fe dichroism due to diffraction effects was found for 3 ML Fe/Co/Cu(001). For evenly magnetized films, the angular variation in the case of 8 ML Fe is expected to show qualitatively the same behavior as for 3 ML, with possibly stronger effects due to the higher number of layers. Compared to the case of 3 ML Fe, however, this angular variation is strongly damped in the 8 ML Fe film, where the experiment reveals an almost vanishing dependence of the asymmetry on the emission angle α with a value of about

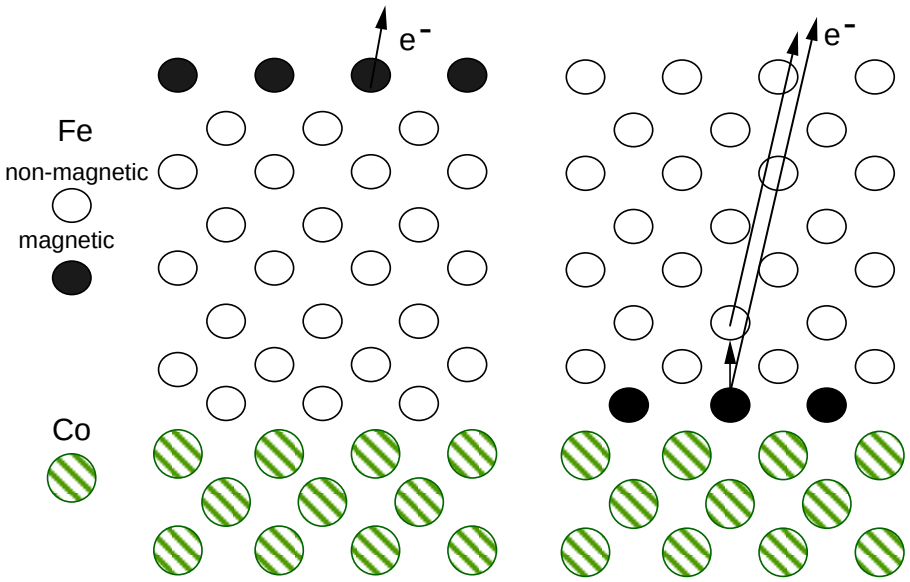

Figure 5.2: A schematic picture of the two possible distributions of the magnetism in 8 ML Fe/Co/Cu(001) film.

1.6% (Fig. 4.25b). This cannot be attributed to structural disorder in the film, since the Fe-$2p_{3/2}$ photoemission intensity (Fig. 4.25a) shows a clear maximum at normal direction, which is the forward scattering along the <001> in a good ordered fcc film. As shown in the Co/Cu(001) system, forward scattering dominates in the diffraction effects at these kinetic energies of the photoemission. The portion of Fe photoelectrons which contribute to the dichroism, i.e., which stem from ferromagnetically ordered Fe atoms, are thus not subject to forward scattering. They must consequently originate from atoms in the topmost two layers at the surface, because in an fcc(001) crystal these are the only ones which do not have scatterers in the <001> emission direction. This leads to the conclusion that within the probing depth of the present experiment the ferromagnetism of the 8 ML Fe film is restricted to the two topmost atomic layers. From thickness dependent studies of Co/Cu(001) in subsection 4.2.3, it has been shown that diffraction effects in the energy region of prominent forward scattering become negligible in monolayer films.

From above, the almost vanishing angular dependence of the asymmetry in 8 ML excluded the existence of an evenly magnetized film with a lower magnetic moment. The two possible distributions of the magnetism mentioned in subsection 4.3.1 have two different locations for the magnetic Fe atoms: the Fe surface on non-ferromagnetic underlayers or the Fe/Co interface under non-ferromagnetic layers. Fig. 5.2 shows schematically the difference between the two possibilities in 8 ML Fe/Co/Cu(001): the photoemission from Fe atoms at the magnetic surface will experience no diffraction, but that from Fe atoms at the magnetic interface will experience diffraction. It is clear

from that picture that an almost vanishing angular dependence of the asymmetry in 8 ML can only be explained by a magnetic live layer *at the surface* of the Fe film on non-ferromagnetic underlayers.

The weak modulation still visible in the curve of 8 ML Fe in Fig. 4.25b may be a hint towards the presence of some amount of ferromagnetic Fe in deeper layers, e.g. at the Fe/Co interface. It may, however, also be attributed to the minor contribution of non-forward scattering to the photoemission signal, the size of which at the present electron energies is expected to be about one order of magnitude weaker than that of forward scattering. This kind of small modulation is also found in the 1.5 ML Co/Cu(001) film, as was reported in subsection 4.2.3.

As a final consideration, one could think that the focusing effect of forward scattering, which leads to the intensity enhancement at normal emission (cf. Fig. 4.25a), correspondingly should lead to a reduction of the asymmetry around $\alpha = 0°$. In the simple picture, where one assumes the enhancement of forward emission to be solely due to photoelectrons from deeper, and, in the present interpretation, non-ferromagnetic layers, such a reduction should be inverse to the intensity curve of Fig. 4.25a, and amount to about 35%. The experimental points of the 8 ML Fe film in Fig. 4.25b do not seem to follow such a reduction at normal emission; the experimental uncertainty, indicated by the error bars, however, may easily mask such an effect.

For a more quantitative analysis of the present data the dichroism of the 8 ML Fe/Co film, which shows no diffraction effects and represents thus the atomic-like contribution, is compared with the atomic-like contribution of the 3 ML Fe film, which is entirely magnetized. For that it is assumed that in the 3 ML film diffraction imposes a modulation on the dichroism as a function of the emission angle around the atomic-like contribution [17, 19]. Taking hence the average between the extrema of the 3 ML curve of Fig. 4.25b as the atomic-like contribution yields about 3.2%. This agrees with the dichroism of a 1 ML Fe film, where in a similar experiment a value of 3.4% was measured, and with the dichroism calculated in Ref. [35]. The dichroism in photoemission from a magnetic layer of thickness t_{mag} is reduced by a factor of $(1-\exp(-t_{mag}/\lambda))\,/\,(1-\exp(-t_{tot}/\lambda))$ if this layer sits on top of a non-ferromagnetic film of thickness t_{nm} of the same material ($t_{tot} = t_{mag}+t_{nm}$). Comparing the dichroism in 8 ML Fe ($\approx 1.6\%$) and the dichroism for the atomic model ($\approx 3.2\%$), this factor can be calculated to be about 0.5. Taking $\lambda = 3.5$ ML as before, for $t_{tot} = 8$ ML we can calculate the thickness of the magnetic layer t_{mag} to be about 2 ML. There is, however, a considerable uncertainty in that estimate because of the separation of atomic and diffraction contributions, possible differences in the magnetic moments, or in $2p$ multiplet splitting in the different films.

It has been proposed that a ferromagnetic ordering could be induced in the bottom Fe layer of Fe/Co/Cu(001) by the coupling to the Co at the Co/Fe interface [77]. Because in 8 ML Fe the signal of the bottommost Fe layer contributes only about 4% to the total Fe photoemission intensity, this possibility of ferromagnetism in the bottom layer cannot be excluded from the present photoemission measurements. From comparison of the MOKE data of 0, 3, and 8 ML Fe films on Co/Cu(001), however, the total amount of ferromagnetic Fe in the 8 ML film can be determined to be 1.8 ± 0.3 ML equivalent. Under the assumption that the Fe film is saturated by the lower fields of the MOKE coil ($\approx$ 1500 Oe) as it is by the field pulses applied during the photoemission measurements, there can be only a very small contribution to the Fe ferromagnetism from the Fe/Co interface. What can unequivocally be excluded is the possibility of a non-magnetic surface, and the possibility of a fully magnetized Fe film with a reduced magnetic moment. Both the absence of diffraction in MDAD, and the strength of the dichroism signal are only consistent with the presence of ferromagnetic ordering at the surface, and no ferromagnetic ordering in deeper layers.

Like in 5 ML Co films, variations of the dichroism using circularly polarized light were found in Fe/Co/Cu(001) films at 0.5 and 3.5 ML (Figs. 4.27a on page 62 and 4.29 on page 64). These variations can be attributed to diffraction effects. Using circularly polarized light with a photon energy of 900 eV, the kinetic energies of the photoelectrons were too low for forward scattering to be prominent (cf. Fig. 4.31 on page 66). The photoemission along any direction will be the result of an interference between the primary wave and all the waves diffracted into the same direction by nearby atoms. By comparing the angular dependence of the dichroic asymmetry of 0.5 ML and 3.5 ML Fe, one thing is clear, namely that diffraction effects in MCDAD of 0.5 ML are comparable with these in thicker films. Although for 0.5 ML all the Fe atoms are at the surface, and all photoelectron diffraction in 0.5 ML involve at least an angle of 90°, diffraction effects in MDAD are still present and similarly strong than in the thicker film. By comparing the dichroic signal of 3.5 ML with 0.5 ML at normal emission (Figs. 4.27a and 4.29), it is clear that there is a strong increase from 3.5 ML to 0.5 ML. As already known both from theory and experiment, the Fe magnetic moment is strongly enhanced by about 30% to 40% at the bcc Fe(001) surface [80, 81]. Similar to this, the increase of the magnetic moment in 0.5 ML Fe film may be explained. A recent theoretical calculation has shown that there is an enhancement of the Fe magnetic moment at the bcc Fe/Co(001) interface [82]. Such an enhancement may also be possible for the fcc Fe/Co(001) interface. For that reason, the enhancement of the Fe magnetic moment in the case of 0.5 Fe/Co film can be even more. Assuming 3.5 ML Fe to have a homogeneous magnetic moment, and a linear dependence between the dichroism and the magnetic moment, the increase

of the magnetic moment can be estimated to be $\sim 30\%$. In reality the asymmetry does not scale linearly with the magnetic moment, and the 3 ML Fe film may also exhibit an enhancement of the magnetic moment at the surface and the Fe/Co interface. However, it is clear that the enhancement is big, and that this enhancement is comparable with bcc Fe.

Fig. 4.30b on page 65 shows that the net magnetizations of Co and Fe are antiferromagnetically aligned in the 6 ML Fe/Co/Cu(001) film. As discussed in subsection 4.3.1, the 6 ML Fe film consists of an fct structure at the surface and nonferromagnetic fcc structure in the lower layers. It is possible that there is some induced ferromagnetism of Fe atoms at the Fe/Co interface. From an energy consideration, ferromagnetic Fe atoms at the Fe/Co interface then must have the same magnetization direction as the Co film, because they are directly in contact with the Co film. It is therefore clear that it is the ferromagnetic surface layer which has a reversed magnetization with respect to the Co film. Because the Co film is found to be fully magnetized, the Fe surface layer cannot have domain structures and must be fully magnetized but with a reversed direction. Remember that the Fe magnetization in 8 ML Fe/Co/Cu(001) film was found to be ferromagnetically coupled with the magnetization of the Co underlayers. It seems that there is an oscillation in interlayer exchange coupling as a function of Fe thickness. It is well-known that the exchange coupling between two ferromagnetic layers separated by a nonmagnetic spacer material oscillates with varying spacer thickness [83-85]. In Ref. [77], an oscillation of the exchange coupling between two Co layers across fcc Fe spacer layer (Co/Fe wedge/Co) was also observed. As discussed before, there is a ferromagnetic Fe layer on top of non-ferromagnetic Fe underlayers in the Fe/Co/Cu(001) system at 6 and 8 ML. There are possible some induced ferromagnetic Fe atoms at the Fe/Co interface, but they are directly in contact with the Co film and must always have the same magnetization direction as the Co film. Therefore, it is the magnetic Fe surface and the Co underlayers that have an exchange coupling, which oscillates with varying Fe thickness (the nonmagnetic Fe thickness).

In conclusion, MLDAD measurements with unpolarized light shows that the observed decrease of ferromagnetic response in Fe/Co/Cu(001) at 8 ML is neither due to a non-ferromagnetic film on top of an induced-ferromagnetic interface, nor to a uniform reduction of the Fe magnetic moment. The results instead show that 8 ML Fe on 5 ML Co/Cu(001) consists indeed of a ferromagnetic layer on top of non-ferromagnetic Fe underlayers, ferromagnetically aligned to the Co substrate. Moreover from MCDAD measurements, the net Fe magnetic response of 6 ML Fe on top of 5 ML Co/Cu(001) was found to be antiferromagnetically aligned to the Co film. Combining both MCDAD and angle-resolved MLDAD measurements, this net anti-

ferromagnetic moment has to be definitely attributed to the Fe surface layers. Upon varying Fe thickness, there is an oscillation in interlayer exchange coupling between the ferromagnetic Fe surface and the Co film. This is in contrast to Ref. [79], where no Fe antiferromagnetic orientation with respect to the Co film has been observed. This discrepancy could possibly be due to the different thickness of the Co film used in the experiment presented here, namely 5 ML in contrast to 15 ML in Ref. [79].

Zusammenfassung

Die vorliegende Arbeit befaßt sich mit Beugungseffekten im magnetischen Dichroismus in der winkelaufgelösten Rumpfniveau-Photoemission. Zunächst wurden Experimente an fcc Co/Cu(001) durchgeführt, um Kenntnisse über das Wesen dieser Effekte zu erhalten. Die Ergebnisse belegen, daß gleichzeitig Informationen über die Struktur und den Magnetismus einer Schicht erlangt werden können. Dieses Wissen regte die Untersuchung von Fe/Co/Cu(001) an. In diesem System wird eindeutig eine magnetische Fe Oberflächelage bei 8 ML Fe Schichtdicke nachgewiesen. Dieses Resultat demonstriert die Anwendbarkeit der Methode, die das Studium der Verteilung von magnetischen Eigenschaften innerhalb eines einzelnen Filmes des gleichen Elements ermöglicht, falls strukturelle Unterschiede vorliegen.

Die Messungen mit unpolarisiertem Licht wurden in einer Geometrie mit einem konstanten Winkel von 45° zwischen der Einfallsrichtung des Lichts **q** und der Emissionsrichtung der Photoelektronen **k** durchgeführt. Der magnetische Dichroismus ist der Unterschied in der Photoemissionsintensität bei Magnetisierungsumkehr. Die Magnetisierung **M** liegt dabei vertikal zur Fläche, die durch **q** und **k** definiert wird. Bei Drehung der Probe um **M** in dieser Geometrie wird jede Winkelabhängigkeit im magnetischen Dichroismus allein durch die Präsenz des Kristallgitters verursacht. In 5 ML fcc Co/Cu(001) bei 100 K wurde eine starke Variation des Dichroismus für Elektronenemissionsrichtungen um die Probennormale gefunden worden, die hauptsächlich durch Interferenz einer Vorwärtsstreuung entlang <001> hervorgerufen wird. Der Dichroismus in der Umgebung der Probennormale kann in zwei Beiträge aufgeteilt werden: einen atomaren und einen beugungsbezogenen Beitrag. Ersterer herrscht bei normaler Emission vor und wird gut durch ein einfaches Modell freier Atome beschrieben. Zweiterer verursacht eine Variation des Dichroismus um die Normalemissionsrichtung und hängt mit der Kristallstruktur zusammen. Eine schwächere Variation des Dichroismus als bei 100 K wurde in 5 ML Co/Cu(001) bei 300 K gefunden, aber der Dichroismus in Richtung der Oberflächennormalen (der atomare Beitrag) ist wegen einer gegenüber 200 K relativ hohen Curietemperatur dieses Films fast unverändert. Die Reduzierung der Beugungseffekte wird durch den Debye-Waller-Effekt erklärt, der die Kohärenz der Streuung im Kristallgitter beeinflußt und deswegen Beugungseffekte in MLDAD verringert.

Um die lineare Drift des Asymmetrienullpunkts zu kompensieren, wurde eine Musterasymmetriekurve benutzt, um damit jede Co-Asymmetriekurve anzupassen. Die Musterkurve wurde durch Mittelung von mehreren Asymmetriespektren von 10 ML Co unter verschiedenen Emissionswinkeln gewonnen und hat daher ein gutes Signal-Rausch-Verhältnis. Es erwies sich, daß mit dieser Musterkurve jede gemessene

Co-Asymmetriekurve gut angepaßt werden konnte. Dies wurde nicht nur für Co-Asymmetriespektren bei unterschiedlicher Co-Dicke, sondern auch für MCDAD- und MLDAD-Spektren, sogar mit verschiedenen Lichtquellen, demonstriert, was in Übereinstimmung mit der Einelektronentheorie ist.

Da die Vorwärtsstreuung sehr empfindlich auf eine Abnahme der Schichtdicke reagiert und der dominante Mechanismus für Beugungeffekte bei kinetischen Energien oberhalb von 400 eV ist, wurde die Dickenabhängigkeit dieser Effekte eingehender untersucht. Bei 100 K wurde gefunden, daß die Beugungseffekte bei Reduzierung der Schichtdicke von 5 ML auf 2 ML deutlich zurückgehen und bei 1.5 ML nahezu völlig verschwunden sind. Bei 300 K ergibt sich von 10 ML bis 3 ML eine ähnliche Tendenz. Bei kleiner Dicke und hoher Temperatur ist die Variation des Dichroismus um die Probennormale generell schwächer und breiter als bei größerer Dicke und niedrigerer Temperatur.

Weil es entlang anderer niedrig indizierter Kristallrichtungen auch Vorwärtsstreuung gibt, sollten ähnliche Beugungseffekte bei Variation der Emissionsrichtung um diese Richtungen herum gefunden werden. Messungen der Winkelabhängigkeit des Maximums im Co-Dichroismus ergaben, daß ähnliche Beugungseffekte auch um andere niedrig indizierte Kristallrichtungen existieren. Die Stärke der Variation des Dichroismus um bestimmte niedrig indizierte Kristallrichtungen hängt hauptsächlich von der Stärke der Vorwärtsstreuung entlang dieser Richtung ab. Es wurde gezeigt, daß die Winkelverteilung sowohl der Intensität als auch des Dichroismus strukturelle Information über ultradünne Filme liefern kann.

Wenn die kinetische Energie der Photoelektronen unterhalb von 200 eV liegt, ist bekannt, daß die Vorwärtsstreuung nicht mehr den vorherrschenden Beitrag zur Photoemission liefert. Mit zirkular polarisierter Röntgenstrahlung niedrigerer Photonenenergie $h\nu < 1000$ eV, aber in derselben experimentellen Geometrie durchgeführte MDAD Messungen an einer 5 ML Co Schicht belegen, daß kleinere Beugungseffekte um die Probennormale sogar ohne dominante Vorwärtsstreuung existieren. Es wurden zusätzlich MCDAD Messungen durchgeführt, bei denen die Magnetisierung in der Fläche liegt, die von $\mathbf{q}$ und $\mathbf{k}$ aufgespannt wird. Auch in diesen Messungen wurden Beugungseffekte um die Probennormale beobachtet.

Die Studie der Beugungseffekte in Co/Cu(001) zeigt, daß sie einen sehr wichtigen Beitrag zum magnetischen Dichroismus in der Rumpfniveau-Photoemission liefern, und es jetzt möglich ist, mit einer Technik gleichzeitig Magnetismus und Struktur eines ultradünnen Filmes zu untersuchen. Dieses Wissen motivierte die Studie von Fe/Co/Cu(001).

MDAD Messungen mit unpolarisierter Strahlung wurden an Fe/Co/Cu(001) Schichten bei Fe-Dicken von 1 ML, 2 ML und 8 ML durchgeführt. Dabei wurde jeweils eine

ferromagnetische Kopplung zwischen Fe und Co festgestellt. Im Gegensatz zu einer starken Variation Dichroismus um die Probennormale bei 3 ML wurde ein fast nicht vom Emissionswinkel abhängiger des Dichroismus bei 8 ML gefunden, obwohl die Vorwärtsstreuung entlang der Probennormale bei 8 ML sogar stärker ist als bei 3 ML. Auch ist der Dichroismus von 8 ML Fe kleiner als von 3 ML. Die unterschiedlichen Winkelabhängigkeiten von 3 ML und 8 ML zeigen deutlich, daß eine ferromagnetische Fe-Oberfläche mit darunterliegenden nichtmagnetischen Fe-Schichten vorliegt.

MCDAD-Experimente wurden auch an Fe/Co/Cu(001)-Schichten bei Fe-Dicken von 0.5 ML, 3.5 ML und 6 ML durchgeführt. Da die Photonenenergie des zirkular polarisierten Lichts in den Messungen nur 900 eV betrug, erhält man kinetische Energien der Fe-2p-Photoelektronen von weniger als 200 eV. Bei diesen Energien ist die Vorwärtssteurichtung nicht bevorzugt, so daß kein Maximum in der Intensitätsverteilung entlang der Probenormale auftritt. In der Winkelabhängigkeit des Dichroismus von 0.5 ML Fe wurde eine Winkelabhängigkeit festgestellt, die durch Beugungen mit größeren Winkeln als 45° stammen muß. Dieses belegt die Bedeutung von Beugungsprozessen mit großen Winkeln unter diesen Bedingungen. Bei 3 ML Fe wurde eine ähnliche Variation des Dichroismus gefunden, dessen Wert aber für jeden Emissionswinkel kleiner ist als bei 0.5 ML. Dies wird durch eine Erhöhung des magnetischen Momentes von 0.5 ML Fe im Vergleich zu dickeren Filmen durch den stärkeren Einfluß von Oberflächen- und Fe-Co Grenzflächenatomen erklärt. Bei 0.5 ML und 3.5 ML Fe lag die Magnetisierung von Fe parallel zu der der darunterliegenden Co-Schicht. Im Gegensatz dazu wurde bei 6 ML Fe eine umgekehrte Magnetisierungsrichtung von Fe im Vergleich zum Co gefunden. Die einzige mögliche Erklärung hierfür ist eine ferromagnetische Oberfläche der Fe-Schicht bei 6 ML mit darunterliegenden nichtmagnetischen Schichten wie bei 8 ML, aber einer antiferromagnetischen Kopplung zwischen der ferromagnetischen Fe Oberflächeschicht und dem Co-Film.

Generell wurde gefunden daß Fe/Co/Cu(001) Schichten in der fct Region (Fe-Dicke < 4 ML) völlig ferromagnetisch sind, wohingegen in der fcc Region (Fe Dicke 5 – 11 ML) eine magnetische Fe Oberfläche mit darunterliegenden nichtmagnetischen Schichten vorliegt. Die Abhängigkeit der Fe-Magnetisierungsrichtung von der Dicke des Fe Filmes (bzw. der Dicke des nichtmagnetischen Fe) wird als ein Übergang von antiferromagnetischer (bei 6 ML) zu ferromagnetischer (bei 8 ML) Kopplung zum Co Film interpretiert.

Das Ergebnis dieser Arbeit zu beiden Systemen (Co/Cu(001) und Fe/Co/Cu(001)) demonstiert, daß die Berücksichtigung von Beugungseffekten in MDAD sehr wichtig ist. Außerdem eröffnen diese Effekte die Möglichkeit, Magnetismus und Struktur gleichzeitig zu untersuchen. Die Untersuchung an Fe/Co/Cu(001) beweist, daß es

möglich ist, aus diesen Effekten Information über die Verteilung von magnetischen Eigenschaften innerhalb eines einzelnen Filmes des gleichen Elements zu erhalten, wenn Bereiche unterschiedlicher Struktur vorliegen.

References

[1] See for example U. Gradmann, J. Magn. Magn. Mater. **100**, 481 (1991); A. J. Freeman and R. Wu, *ibid.* **100**, 497 (1991).

[2] C. S. Fadley, M. A. Van Hove, Z. Hussain, and A. P. Kaduwela, J. Electr. Spectr. Rel. Phen. **75**, 273 (1995); C. S. Fadley, Surf. Sci. Rep. **19**, 231 (1993); C. S. Fadley, in: *Synchrotron Radiation Research: Advances in Surface Science*, edited by R. Z. Bachrach, (Plenum Press, New York, 1992).

[3] L. Baumgarten, C. M. Schneider, H. Petersen, F. Schäfers, and J. Kirschner, Phys. Rev. Lett. **65**, 492 (1990).

[4] H. Ebert,, L. Baumgarten, C. M. Schneider, and J. Kirschner, Phys. Rev. B **44**, 4406 (1991).

[5] C. M. Schneider, D. Venus, and J. Kirschner, Phys. Rev. B **45**, 5041 (1992).

[6] D. Venus, L. Baumgarten, C. M. Schneider, C. Boeglin and J. Kirschner, J. Phys.: Cond. Matt. **5**, 1239 (1993).

[7] C. M. Schneider, J. Kirschner, and D. Venus, in: *Vacuum Ultraviolet Radiation Physics*, edited by F. J. Wuilleumier, Y. Petroff, I. Nenner, (World Scientific, Singapore, 1993) p421.

[8] Ch. Roth, F. U. Hillebrecht, H. B. Rose, and E. Kisker, Phys. Rev. Lett. **70**, 3479 (1993); Ch. Roth, H. B. Rose, F. U. Hillebrecht, and E. Kisker, Solid State Commun. **86**, 647 (1993).

[9] F. U. Hillebrecht and W.-D. Herberg, Z. Phys. B **93**, 299 (1994).

[10] W. Kuch, M.-T. Lin, W. Steinhögl, C. M. Schneider, D. Venus, and J. Kirschner, Phys. Rev. B **51**, 609 (1995).

[11] F. Sirotti and G. Rossi, Phys. Rev. B **49**, 15 682 (1994).

[12] G. Rossi, F. Sirotti, N. A. Cherepkov, F. Combet Farnoux, and G. Panaccione, Solid State Comm. **90**, 557 (1994).

[13] G. Rossi, G. Panaccione, F. Sirotti, N. A. Cherepkov, Phys. Rev. B **55**, 11 483 (1997).

[14] G. Rossi, G. Panaccione, F. Sirotti, S. Lizzit, A. Baraldi, and G. Paolucci, Phys. Rev. B **55**, 11 488 (1997).

[15] C. M. Schneider, U. Pracht, W. Kuch, A. Chassé, and J. Kirschner, Phys. Rev. B **54**, R15618 (1996).

[16] H. B. Rose, F. U. Hillebrecht, E. Kisker, R. Denecke, and L. Ley, J. Magn. Magn. Mat. **148**, 62 (1995); F. U. Hillebrecht, H. B. Rose, T. Kinoshita, Y. U. Idzerda, G. van der Laan, R. Denecke, and L. Ley, Phys. Rev. Lett. **75**, 2883 (1995).

[17] A. Fanelsa, R. Schellenberg, F. U. Hillebrecht, and E. Kisker, Solid State Commun. **96**, 291 (1995); A. Fanelsa, R. Schellenberg, F. U. Hillebrecht, E. Kisker, J. G. Menchero, A. P. Kaduwela, C. S. Fadley, and M. A. van Hove, Phys. Rev. B **54**, 17 962 (1996).

[18] F. U. Hillebrecht, Ch. Roth, H. B. Rose, W. G. Park, E. Kisker and N. A. Cherepkov, Phys. Rev. B **53**, 12182 (1996).

[19] R. Schellenberg, E. Kisker, A. Fanelsa, F. U. Hillebrecht, J. G. Menchero, A. P. Kaduwela, C. S. Fadley, and M. A. van Hove, Phys. Rev. B **57**, 14310 (1998).

[20] R. Schellenberg, E. Kisker, M. Faust, A. Fanelsa, and F. U. Hillebrecht, Phys. Rev. B **58**, 81 (1998).

[21] N. A. Cherepkov, Phys. Rev. B **50**, 13813 (1994).

[22] C. M. Schneider, A. K. Schmid, P. Schuster, H. P. Oepen, and J. Kirschner, in: *Structure and Magnetism in Low-Dimensional Systems*, ed. by R. F. Farrow, M. Donath, B. Dieny, A. Fert, and B. Hermsmeier (Plenum, New York 1993).

[23] C. M. Schneider, J. J. de Miguel, P. Bressler, J. Garbe, S. Ferrer, R. Miranda, and J. Kirschner, J. de Physique **C8**, 1657 (1988).

[24] Hong Li and B. P. Tonner, Surf. Sci. **237**, 141 (1990).

[25] J. R. Cerdá, P. L. de Andres, A. Cebollada, R. Miranda, E. Navas, P. Schuster, C. M. Schneider, and J. Kirschner, J. Phys. : Condens. Matter **5**, 2055 (1993).

[26] A. Clarke, G. Jennings, R. F. Willis and J. B. Pendry, Surf. Sci. **187**, 327 (1987).

[27] C. M. Schneider, P. Bressler, P. Schuster, J. Kirschner, J. J. de Miguel and R. Miranda, Phys. Rev. Lett. **64**, 1059 (1990).

[28] P. Krams, F. Lauks, R. L. Stamps, B. Hillebrands, and G. Günterrodt, Phys. Rev. lett. **69**, 3647 (1992).

[29] C. M. Schneider, P. Bressler, P. Schuster, J. Kirschner, J. J. de Miguel, R. Miranda, and S. Ferrer, Vacuum **41**, 503 (1990).

[30] Dongqi Li, M. Freitag, J. Pearson, Z. Q. Qiu, and S. D. Bader, Phys. Rev. Lett. **72**, 3112 (1994); J. Appl. Phys. **76**, 6425 (1994); S. D. Bader, and Dongqi Li, J. Magn. Magn. Mater. **156**, 153 (1996). B. Gubanka, M. Donath, and F. Passek, *ibid.* **161**, L11 (1996).

[31] P. Bayer, S. Müller, P. Schmailzl, and K. Heinz, Phys. Rev. B **48**, 17 611 (1993); S. Müller, P. Bayer, A. Kinne, P. Schmailzl, and K. Heinz, Surf. Sci. **322**, 21 (1995).

[32] M. Straub, R. Vollmer, and J. Kirschner, Phys. Rev. Lett. **77**, 743 (1996).

[33] R. D. Ellerbrock, A. Fuest, A. Schatz, W. Keune, and R. A. Brand, Phys. Rev. Lett. **74**, 3053 (1995).

[34] D. P. Woodruff and T. A. Delchar, in: *Modern Techniques of Surface Science*, (Cambridge University, Cambridage, 1994), p140.

[35] J. G. Menchero, Phys. Rev. B **57**, 993 (1998).

[36] N. A. Cherepkov and V. V. Kuznetsov, J. Phys. B **22**, L405 (1989).

[37] N. A. Cherepkov, J. Phys. Condens. Matter **8**, 4971 (1996).

[38] B. T. Thole and G. van der Laan, Phys. Rev. B **49**, 9613 (1994).

[39] G. van der Laan, J. Magn. Magn. Mat. **148**, 53 (1995).

[40] G. van der Laan, J. Electr. Rel. Phen. **86**, 41 (1997).

[41] G. van der Laan, J. Phys.: Condens. Matt. **9**, L259 (1997).

[42] G. van der Laan, Phys. Rev. B **57**, 5250 (1998).

[43] J. G. Menchero, Phys. Rev. B **57**, 1001 (1998).

[44] J. G. Menchero, C. S. Fadley, G. Panaccione, F. Sirotti, and G. Rossi, Sol. State Commun. **103**, 197 (1997).

[45] J. G. Menchero, Phys. Rev. B **55**, 5505 (1997).

[46] E. Tamura, G. D. Waddill, J. G. Tobin, and P. A. Sterne, Phys. Rev. Lett. **73**, 1533 (1994).

[47] J. Henk, A. M. Niklasson,and B. Johansson, to be published.

[48] D. Venus, Phys. Rev. B **49**, 8821 (1994); G. van der Lann and B. T. Thole, Solid State Commun. **92**, 427 (1994).

[49] M. O. Krause and J. G. Ferreira, J. Phys. B **8**, 2007 (1975).

[50] M. Drescher, G. Snell, U. Kleineberg, H.J. Stock, N. Müller, U. Heinzmann and N. B. Brookes, Rev. Sci. Instrum. **68**, 1939 (1997).

[51] C. T. Chen, Nucl. Instrum. Methods A**256**, 595 (1987).

[52] S. Y. Tong, M. W. Puga, H. C. Poon, and M. L. Xu, in: *Chemistry and Physics of Solid Surfaces VI*, ed. by R. Vanselow, and R. Howe (Springer, Berlin, 1986), p. 509.

[53] W. F. Egelhoff, Jr, Phys. Rev. B **30**, 1052 (1984).

[54] W. F. Egelhoff, Jr: *in Structure of Surfaces*, ed by M. A. Van Hove and S. Y. Tong, (Springer, Berlin, 1985), p. 199.

[55] M. Fink and J. Ingram, Atomic Data **4**, 1 (1972); M. B. Webb and M. G. Lagally, Solid State Phys. **28**, 301 (1973).

[56] C. S. Fadley, Phys. Scr. T**17**, 39 (1987).

[57] R. A. Armstrong and W. F. Egelhoff, Jr, Surf. Sci. **154**, L225 (1985).

[58] W. F. Egelhoff, Jr, Phys. Rev. Lett. **59**, 559 (1997).

[59] J. F. Moulder, W. F. Stickle, P. E. Sobol, and K. D. Bomben, in: *Handbook of X-ray Photoelectron Spectroscopy*, ed. by J. Chastain (Perkin-Elmer Corporation, Physical Electronics Division, Eden Prairie, 1992).

[60] S. Doniach and M. Šunjić, J. Phys. C **3**, 285 (1970).

[61] P. Rennert and Yu Kucherenko, J. Electr. and Rel. Phen. **76**, 157 (1995).

[62] F. U. Hillebrecht, H. B. Rose, T. Kinoshita, Y. U. Idzerda, G. van der Lann, R. Denecke, and L. Ley, Phys. Rev. Lett. **75**, 2883 (1995).

[63] A. K. See and L. E. Klebanoff, Phys. Rev. Lett. **74**, 1454 (1995); Phys. Rev. B **51**, 11002 (1995).

[64] B. T. Thole and G. van der Laan, Phys. Rev. Lett. **67**, 3306 (1991); Phys. Rev. B **44**, 12424 (1991).

[65] S. D. Bader and J. L. Erskine, in: *Ultrathin Magnetic Structures II*, ed. by B. Heinrich and J. A. C. Bland, (Springer, berlin, 1994) p297

[66] B. M. McCoy and T. S. Wu, in: *The two-dimensional Ising model*, (Harvard, Cambridge, 1973).

[67] H. Ebel, C. Pöhn, R. Svagera, M. E. Wernle, M. F. Ebel, and A. Jablonski, J. Electr. Spectr. Rel. Phenom. **50**, 109 (1990).

[68] C. S. Wang, B. M. Klein, and H. Krakauer, Phys. Rev. Lett. **54**, 1852 (1985); F. J. Pinski, J. Staunton, B. L. Gyorffy, D. D. Johnson, and G. M. Stocks, *ibid.* **56**, 2096 (1986).

[69] V. L. Moruzzi, P. M. Marcus, K. Schwartz, and P. Mohn, Phys. Rev. B **34**, 1784 (1986); V. L. Moruzzi, P. M. Marcus, and J. Kübler, *ibid.* **39**, 6957 (1989).

[70] Y. Zhou, W. Zhang, L. Zhong, X. Nie, and D.-S. Wang, J. Magn. Magn. Mater. **167**, 136 (1997).

[71] R. Lorenz and J. Hafner, Phys. Rev. B **54**, 15 937 (1996); T. Asada and S. Blügel, Phys. Rev. Lett. **79**, 507 (1997).

[72] P. Montano, G. W. Fernando, B. R. Cooper, E. R. Moog, H. M. Naik, S. D. Bader, Y. C. Lee, Y. N. Darici, H. Min and J. Marcano, Phys. Rev. lett. **59**, 1041 (1987); D. Pescia, M. Stampanoni, G. L. Bona, A. Vaterlaus, R. F. Willis and F. Meier, Phys. Rev. Lett. **58**, 2126 (1987); C. Liu, E. R. Moog and S. D. Bader, Phys. Rev. Lett. **60**, 2422 (1988); W. A. A. Macedo and W. Keune, Phys. Rev. Lett. **61**, 475 (1988).

[73] S. Müller, P. Bayer, C. Reischl, K. Heinz, B. Feldmann, H. Zillgen, and M. Wuttig, Phys. Rev. Lett. **74**, 765 (1995); S. Müller, P. Bayer, A. Kinne, C. Reischl, R. Metzler, and K. Heinz, Surf. Sci. **331-333**, 723 (1995); K. Heinz, S. Müller, and P. Bayer, *ibid.* **337**, 215 (1995).

[74] M. Wuttig, B. Feldmann, J. Thomassen, F. May, H. Zillgen, A. Brodde, H. Hannemann, and H. Neddermayer, Surf. Sci. **291**, 14 (1993); T. Detzel, N. Memmel, and T. Fauster, *ibid.* **293**, 227 (1993); N. Memmel and T. Detzel, *ibid.* **307-309**, 490 (1994).

[75] W. L. O'Brien and B. P. Tonner, Surf. Sci. **334**, 10 (1995); Phys. Rev. B **52**, 15 332 (1995); J. Appl. Phys. **79**, 5629 (1996).

[76] E. J. Escorcia-Aparicio, R. K. Kawakami, and Z. Q. Qiu, J. Appl. Phys. **79**, 4964 (1996).

[77] E. J. Escorcia-Aparicio, R. K. Kawakami, and Z. Q. Qiu, Phys. Rev. B **54**, 4155 (1996).

[78] E. J. Escorcia-Aparicio, R. K. Kawakami, H. J. Choi, and Z. Q. Qiu, J. Appl. Phys. **81**, 4714 (1997).

[79] R. Kläsges, D. Schmitz, C. Carbone, W. Eberhardt, and T. Kachel, Solid State Comm. **107**, 13 (1998).

[80] S. Ohnishi, M. Weinert, and A. J. Freeman, Phys. Rev. B **28**, 6741 (1983).

[81] E. Tamura, R. Feder, G. Waller, and U. Gradmann, Phys. Status Solidi B **157**, 627 (627).

[82] B. Swinnen, J. Meersschaut, J. Dekoster, G. Langouche, S. Cottenier, S. Demuynck, and M. Rots, Phys. Rev. Lett. **78**, 362 (1997).

[83] C. F. Majkrzak, J. W. Cable, J. Kwo, M. Hong, D. B. McWhan, Y. Yafet, J. V. Waszczak, and C. Vettier, Phys. Rev. Lett. **56**, 2700 (1986).

[84] J. Kwo, M. Hong, F. J. DiSalvo, J. V. Waszczak, and C. F. Majkrz, Phys. Rev. B **35**, 7295 (1987).

[85] S. S. Parkin, N. More, and K. P. Roche, Phys. Rev. Lett. **64**, 2304 (1990).

Acknowledgements

I would like to thank my adviser, Prof. J. Kirschner for providing me with the opportunity and guidance to do this doctoral work in this institute with very nice circumtance. His suggestion and experience is always a big help to me.

I am very grateful to Prof. H. Neddermeyer and Prof. K. Baberschke for their kindness to be the referees of this thesis.

My special thanks to Dr. W. Kuch for his fruitfull collobration. He has not only helped me by his valueful experience and discussion, but also shown me how to organize and work effeiciently.

I am very grateful to Dr. M. Salvietti, who worked closely with me in the first two years of my work.

I am also indebted to Ms. B. Zada for her help in all repairment, technical problem and also order of the necessary parts for the experiment.

I would like to express my gratitude to other colleagues in Max-Planck-institut and especially these in AG Bessy in Berlin: R. Frmter, J. Gilles, Dr. D. Hartman, Dr. S. Kang, Dr. M.-T. Lin, F. Offi and M. Seider.

Finally, my sincere gratefulness to my wife M. Ruan, for he love and support in these years.

Erklärung an Eides Statt:

Ich erkläre, daß ich die vorliegende Dissertation **Photoelectron diffraction in magnetic dichroism in core-level photoemission** selbständig und ohne fremde Hilfe verfaßt, andere als die von mir angegebenen Quellen und Hilfsmittel nicht benutzt und den benutzten Werken wörtlich oder inhaltlich entnommene Stellen als solche kenntlich gemacht habe.

Halle, den 11. 03. 99

Xingyu Gao

Eidesstattliche Erklärung:

Ich erkläre, daß ich mich zu keinem früheren Zeitpunkt um den Doktorgrad beworben habe.

Halle, den 11. 03. 99

Xingyu Gao

Lebenslauf:

Persönliche Daten:

Name:	Xingyu Gao
Geburtstag:	08 October, 1969
Geburtsort:	Minshan im Provenz Sichaun, V. R. China
Familienstand:	verheiratet

Schulausbildung:

1981–1984	Grundschule Minshan, V. R. China
1984–1987	Gymanasium Minshan, V. R. China

Hochschulausbildung:

1987–1991	Universität Beijing, Fakultät für Physik, Diplom (B. Sc.) in Physik
1991–1994	Universität Beijing, Fakultät für Physik, Diplom (M. Sc.) in Physik
1996–1999	Promotionsarbeit in der Arbeitsgruppe von Prof. Dr. J. Kirschner am Max-Planck-Institut für Mikrostrukturphysik in Halle/Saale